Défauts induits par l'implantation d'hélium dans les matériaux à base silicium

Erwan Oliviero

▶ To cite this version:

Erwan Oliviero. Défauts induits par l'implantation d'hélium dans les matériaux à base silicium. Physique [physics]. Université de Poitiers, 2001. Français. NNT : . tel-00107085

HAL Id: tel-00107085
https://theses.hal.science/tel-00107085

Submitted on 17 Oct 2006

HAL is a multi-disciplinary open access archive for the deposit and dissemination of scientific research documents, whether they are published or not. The documents may come from teaching and research institutions in France or abroad, or from public or private research centers.

L'archive ouverte pluridisciplinaire **HAL**, est destinée au dépôt et à la diffusion de documents scientifiques de niveau recherche, publiés ou non, émanant des établissements d'enseignement et de recherche français ou étrangers, des laboratoires publics ou privés.

Label Européen

THESE

pour l'obtention du grade de

DOCTEUR DE L'UNIVERSITE DE POITIERS

Faculté des Sciences Fondamentales et Appliquées

Diplôme National - Arrêté du 30 mars 1992

ECOLE DOCTORALE SCIENCES POUR L'INGENIEUR
DOMAINE DE RECHERCHE : MILIEUX DENSES ET MATERIAUX

Présentée par

Erwan OLIVIERO

Défauts induits par l'implantation d'hélium dans les matériaux à base silicium

---

Directeurs de thèse :
J.F. BARBOT et M.F. BEAUFORT

Soutenue le 20 décembre 2001

JURY

C. TEMPLIER	Professeur à l'Université de Poitiers	*Président*
S.E. DONNELLY	Professeur à l'Université de Salford (Grande Bretagne)	*Rapporteur*
A. van VEEN	Professeur à l'Université de Delft (Pays-Bas)	*Rapporteur*
D. ALQUIER	Maître de Conférences à l'Université de Tours	*Examinateur*
J.F. BARBOT	Professeur à l'Université de Poitiers	*Examinateur*
M.F. BEAUFORT	Chargée de Recherches au CNRS, Université de Poitiers	*Examinatrice*

CONTENTS

1. Introduction **1**

2. Helium implantation induced defects in silicon **7**

2.1. Ion implantation ..7

2.2. The Helium-Silicon system 10

2.3. Low dose helium implantation 12

2.4. High dose helium implantation 15

2.5. Medium dose helium implantation 18

2.6. Methods of study 21

2.7. Conclusion 23

3. Helium bubbles and related defects in silicon **26**

3.1. High energy implantation 26

3.1.1. Medium doses helium implantation 41
3.1.2. Influence of dose and dose-rate on bubble formation 53
3.1.3. Influence of annealing time on bubble and defect formations 16

3.2. He desorption from He implanted silicon at high temperature 65

3.1.1. Experimental procedure 65
3.1.2.Conventional (isochronal) ramp annealing 66
3.1.3. Partial annealing measurements 72
3.1.4. Discussion 75
3.1.5. Conclusion 79

4. Helium implantation in silicon carbide **81**

4.1. High energy implantation 81

4.1.1. Experimental procedure 82
4.1.2. Results and discussion 82
4.1.3. Modelisation of the damaged structure 92
4.1.4. Summary 96

4.2. He desorption from SiC: a study of bubble precursors 99

4.2.1. Experimental procedure 99
4.2.2. 6H-SiC .100
4.2.3. 4H-SiC .103
4.2.4. CVD-SiC .108
4.2.5. Discussion .110
4.2.6. Conclusion .118

5. Discussion: He bubble formation in Si **120**

5.1. During implantation at room temperature 120

5.1.1. Bubble nucleation 120
5.1.2. Bubble growth 121
5.1.3. Critical dose for bubble formation 122

5.2. Bubble growth during annealing 123

6. Conclusion **127**

Appendix.1: Experimental techniques **130**

Appendix.2: Experimental data **138**

Acknowledgements **144**

1-Introduction

Materials requirements for semiconductors used in microelectronics become continuously more severe. Impurities and crystallographic defects can strongly modify the characteristics of electronic devices: increase of the leakage current in PN junction, decrease of the minority carriers lifetime, etc…Therefore, to improve device performance, it is essential to control the impurity concentration as well as the nucleation of defects. In silicon wafers the density of extended crystallographic defects must be extremely low even after high temperature processing steps. The density of metallic impurities (fast diffusers) in the active region of the devices must also be extremely low, at a level of 10^{10} at/cm^3. Such an impurity level can only be reached by a gettering treatment, i.e. by extracting the impurities far from the active region of electronic devices. In the last few years, helium induced cavities in silicon have received considerable attention due to their potential technological applications. Indeed, recent works [Follstaedt *et al.* 1996, Raineri *et al.* 1995] have shown that these cavities can be used as very efficient gettering sites. Cavities in silicon are usually formed by high dose He ion implantation. Due to its low solubility, He segregates in gas-vacancy complexes and, depending on implantation parameters such as energy and dose, form bubbles. Then, during annealing at temperatures above 700ºC, bubbles grow and He is released from the bubbles by gas-out diffusion, leading to void formation, i.e. cavities. Metallic impurities can thus be trapped on the cavities by a chemisorption process at their internal surfaces [Follstaedt *et al.* 1996]. Moreover, Deep Level Transient Spectroscopy (DLTS) measurements on diodes containing voids have shown the presence of deep levels localized near the middle of the band gap [Raineri *et al.* 1996]. Thus these voids could also be used for the generation of recombination centres to control charge carrier lifetime in the active region of silicon power devices. Helium bubble formation is a complex phenomenon involving different processes or mechanisms such as loop punching, migration and coalescence, Oswald ripening, trap-mutation…etc. In order to have better control over location, size, size distribution and associated defects of the cavities, numerous studies have been performed varying implantation parameters such as energy, dose or annealing parameters [Raineri *et al.* 2000]. However, the effects of varying the implantation temperature have not received much attention. Thus Si wafers have been implanted with He at different temperatures ranging from 200°C to 800°C. The interest of high temperature implantation would be not only to substitute the annealing step after implantation but also to obtain more information on the formation of

secondary defects formation. A combination of transmission electron microscopy (TEM) and thermal helium desorption spectrometry (THDS) is used to study the effect of implantation temperature on the microstructure of defects and bubbles as well as the helium content and activation energy for helium release. Results and discussion are presented in part 3.2.
Furthermore, most of the above mentioned studies have concentrated on low energy (i.e. in the keV range) implants producing a damaged layer in the vicinity of the implanted surface. High-energy (i.e. in the MeV range) implantation can produce cavities deep into silicon (>3 μm), in a well-defined region beyond the active region of electronic devices. The use of ion implantation with energies in the MeV range is steadily increasing in the fabrication of Si integrated circuits [Williams *et al.* 1993]. Lateral gettering, that has been recently found to be efficient in the case of iron (keV range) [Roqueta *et al.* 2000], could be also used in the periphery of active device. In this energy range, however, very few investigations have been performed to study bubbles formation and evolution upon annealing. It is obvious that a different behavior is expected. In particular, the helium desorption from bubbles should be more difficult with increasing energy, since the rate of desorption is shown to be depth dependent [Griffioen *et al.* 1987]. The release of He will be less influenced by the proximity of the surface. This has been recently confirmed by Non Rutherford elastic Backscattering (NRBS) experiments where 90 % of helium has been found to stay in bubbles after annealing at 800°C for 30 min in 1.6 MeV He implanted silicon [Godey *et al.* 2000]. Recent studies [Oliviero 1999, Godey 2000] have also shown that in this energy range, the induced damage is different. In some cases it has been reported that MeV implantation can lead to the formation of rows of dislocations from the cavity band [Godey 2000]. Dislocations that form upon annealing are known to be associated with both shallow and deep-lying electronic states in the band gap and thereby have strong direct or indirect effects on the electronic properties of semiconductors [Alexander *et al.* 1991]. They can also be used as gettering centers [Ourmazd *et al.* 1986]. They are however unstable, thus their nucleation must be controlled. These particular types of defects and thus MeV implantations are studied in details in part 3.1.

Silicon plays a major role in the development of modern semiconductor device technology and is the most used in the semiconductor technology. Almost all of today's computer chips are built on silicon wafer. Silicon is one of the most abundant materials on the earth. Si wafers are made of highly purified sand which is refined to produce 99.999999 % pure silicon. However, with the fast development of electronics, the limits of Si are reached and new semiconductor materials are required not to replace silicon but to extend the range of

semiconductor applications. The pronounced tendency of silicon carbide (SiC) to crystallize into many different configurations, the so-called polytypes (more than 250 different polytypes have been reported up to now [Wesch *et al.* 1996]), with a broad variation of the band gap, in combination with other outstanding properties (high temperature stability, high chemical resistivity, radiation hardness…) make SiC the most promising candidate. However all these properties complicate its synthesis and a lot of efforts have been made to develop and improve methods of bulk and epitaxial layer growth in order to produce SiC of high purity and good crystalline quality. Considerable efforts are still required before SiC devices are brought to market. After fusion work, the research on SiC almost died in the 70s because of the lack of progress in crystal growth, but nowadays it is making a huge comeback in semiconductor technology. Primary application fields of SiC are optoelectronics (blue light emitting diodes, UV photodiodes), high temperature electronics (ranging from pn-junction to field effect transistor), radiation hard electronics (nuclear reactor, space electronics) and high power/high frequency electronics. Ion implantation is a process used in many stages when building the semiconductors devices (basic doping stage,..etc.). Implantation usually induces structural damages in the crystal and thus can affect its electronic properties. In order to create functioning devices, this implantation-induced damage has to be removed. The use of ion implantation in semiconductor technology has recently acquired new interest. In particular, low dose proton irradiation for charge carrier lifetime control in silicon power devices has received considerable attention due to its ability to locally introduce deep levels in devices, predominantly in the nuclear stopping region. At high doses, implantation of light ions (protons, He) has been successful in the process of "Smart Cut®" (hydrogen) and in creating gettering sites, e.g. the bubble structures in the case of helium implantation in silicon [Follstaedt *et al.* 1996, Raineri *et al.* 1995]. High energy proton bombardment prior to packaging is also proposed to create semi-insulating regions in Si wafers [Lee *et al.* 2001] for RF integrated circuits. Ion implantation is also an important processing step of many SiC electronic devices. Specific problems are associated with ion implantation in SiC as for example the activation ratio of acceptor implantation (Al or B) to define the p-well in order to support a large blocking voltage when the device (DMOSFET) is off. MeV oxygen implantation into SiC is also studied for the development of SiC-on-insulator substrates for SiC-CMOS technology [Ishimaru *et al.* 1999]. This process, known as separation by implanted oxygen (SIMOX), is already well developed and commercialised in Si-based SOI wafers. The proton irradiation to create insulated regions in SiC wafers for device integration is also investigated. High dose hydrogen implantation is also used in SiC to process Smart

Cut® [Di Cioccio *et al.* 1997] and finally to elaborate SiCOI (SiC On Insulator). Even in the case of low doses (10^{10} cm^{-2}) helium implantation, a strong compensation occurs around the maximum of the elastic energy deposition. It is thus concluded that ions stopped in SiC produce at least five times more point defects than in Si [Hallen *et al.* 1999]. Nitrogen deactivation through reactions with migrating point defects is proposed to explain this implantation-induced compensation [Åberg *et al.* 2001]. For high doses, if stable cavities can also be formed in SiC, similar studies as those done in Si may be possible to improve the fundamental understanding of ion implants in SiC and thus to promote their use for new microelectronic devices. The formation of bubbles in high dose He implanted SiC is studied in part 4. A thermal helium desorption spectrometry (THDS) investigation of helium implantation induced defects (bubble precursors) in SiC is also presented. THDS studies were originally devoted to defects in metals, but have been also applied to silicon and ceramics providing interesting results [Van Veen *et al.* 1991]. It has been shown to be a powerful technique to investigate the defects created by ion implantation and their thermal stability. THDS can also provide quantitative information as the population of defects and the amount of helium remaining in the samples after annealing.

In the first part of this thesis, the effects of helium implantation in silicon are reviewed. The second part is devoted to helium bubbles and related defects in silicon. Firstly a detailed study on MeV implantations is described. Afterwards THDS results and discussion on the effect of implantation temperature on bubbles formation are presented. The third part is dedicated to helium implantation into SiC. Thereafter, the bubble formation is discussed and finally conclusions are drown.

References

[Åberg *et al.* 2001] D. Åberg, A. Hallén, P. Pellegrino, B.G. Svensson, *Appl. Phys. Lett.* **78**, 2908 (2001).

[Alexander *et al.* 1991] H. Alexander and H. Teichler, in *Materials Sciences and Technology*, vol. 4, *Electronic Structure and Properties of Semiconductors*, Ed. W. Schröter, VCH, Weinheim 1991 (pp. 249 to 320).

[Di Cioccio *et al.* 1997] L. Di Cioccio, F. Letertre, Y. Le Tiec, A.M. Papon, C. Jaussaud, M. Bruel, *Mat. Sci. Eng. B* **349-356**, 378 (1997).

[Follstaedt *et al.* 1996] D.M. Follstaedt, S.M. Myers, G.A. Petersen, and J.W. Medernach, *J. Electron. Mater.* **25**, 157 (1996).

[Godey 2000] S. Godey, Ph.D. thesis, Université d'Orléans, 2000.

[Godey *et al.* 2000] S. Godey, T. Sauvage, E. Ntsoenzok, M.F Beaufort, J.F. Barbot, B. Leroy, *J. Appl. Phys.* **87**, 2158 (2000).

[Griffioen *et al.* 1987] C.C. Griffioen, J.H. Evans, P.C. De Jong, A. Van Veen, *Nucl. Instr. Methods Phys. Res. B* **27**, 417 (1987).

[Hallen *et al.* 1999] A. Hallen, A. Henry, P. Pellegrino, B.G. Svensson, D. Åberg, *Mat. Sci. Eng. B* **61-62**, 378 (1999).

[Ishimaru *et al.* 1999] M. Ishimaru, R.M. Dickerson, K.E. Sickafus, *Appl. Phys. Lett.*, 352 (1999).

[Lee *et al.* 2001] L.S. Lee; C.P. Liao; C.L. Lee; T.H. Huang; D.D.L. Tang; T.S. Duh; T.T. Yang, *IEEE* **48**, 928 (2001).

[Oliviero 1999] E. Oliviero, DEA report, Université de Poitiers, 1999.

[Oliviero *et al.* 2001] E. Oliviero, M.L. David, J. Nomgaudyte, L. Pranevicius M.F. Beaufort, A. Declémy, J.F. Barbot , *J. Appl. Phys.* accepted (2001).

[Ourmazd *et al.* 1986] A. Ourmazd, *Mater. Res. Soc. Symp. Proc.* **59**, 331 (1986).

[Raineri *et al.* 1995] V. Raineri, P.G. Fallica, G. Percolla, A. Battaglia, M. Barbagallo, S.U. Campisano, *J. Appl. Phys.* **78**, 3727 (1995).

[Raineri *et al.* 1996] V. Raineri, P.G. Fallica, S. Libertino, *J. Appl. Phys.* **79**, 9012 (1996).

[Raineri *et al.* 2000] V. Raineri, M. Saggio, E. Rimini, *J. Mater. Res.* **15**, 1449 (2000).

[Roqueta *et al.* 2000] F. Roqueta, L. Ventura, J.J. Grob, R. Jérisian, *J. Appl. Phys.* **88**, 5000 (2000).

[Van Veen *et al.* 1991] A. van Veen, in: *Fundamental Aspects of Inert Gases in Solids*, S.E. Donnelly, J.H. Evans (Eds), NATO ASI series B, Physics 279, Plenum Publishing Corp., New York, 1991, pp 41-57.

[Wesch *et al.* 1996] W. Wesch, *Nucl. Instr. Methods Phys. Res. B* **116**, 305 (1996).

[Williams *et al.* 1993] J.S. Williams, R.G. Elliman, M.C. Ridway, C. Jagadish, S.L. Ellingboe, R. Golberg, M. Petravic, W.C. Wong, Z. Dezhang, E. Nygren, B.G. Svensson, *Nucl. Instr. Methods Phys. Res. B* **80/81**, 507 (1993).

2-Helium implantation induced defects in silicon

2.1 Ion Implantation

Implantation of energetic particles into materials induces micro-structural modifications that can strongly affect their mechanical and/or electronic properties. A fraction of the energy of the incident particle is deposited in the material in the form of point defects (see Fig.2.1) through a number of mechanisms such as electron excitations, ionization and atomic collisions. These fundamental point defects can combine to form more complex defect structures. Actually, damage is closely related to the energy transferred by the ion, and thus to its slowing down within the material. Two different processes of defect creation are associated with two types of interaction: the interaction between ions and target atoms (nuclear energy loss: $\left.\frac{dE}{dx}\right)_n$), and the interaction between ions and target electrons (electronic loss: $\left.\frac{dE}{dx}\right)_e$).

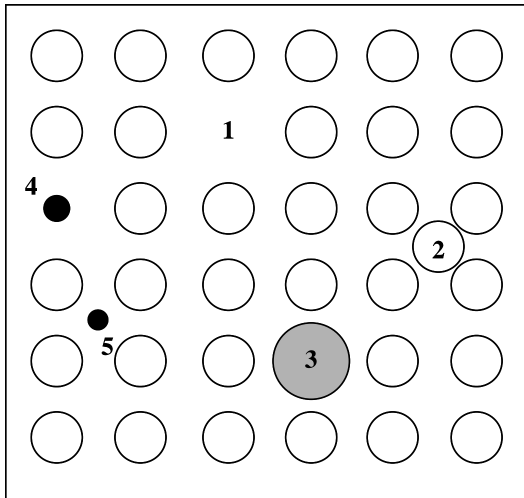

Figure 2.1: Point defects created in crystalline materials: (1) Vacancy, (2) Self-interstitial, (3) and (4) Foreign substitutional, (5) Foreign interstitial.

Nuclear stopping is the direct transfer of an amount of the kinetic energy from the incoming ions to the target atoms. This mechanism is known as atomic collision, elastic collision or nuclear collision. Depending on its energy, the incoming ion can displace one atom off its site and thus create a Frenkel pair (i.e. a vacancy and interstitial pair). The first ejected atom (primary atom) can then kick out other atoms and induce a collision cascade in the lattice (see Fig.2.2), provided its kinetic energy is large enough. To kick out one atom of its site, the incoming ion must have a kinetic energy higher than the threshold displacement energy E_{th} that is specific to the material.

Figure 2.2: Collision cascades created by implantation of an ion: Vacancy (o), Self-Interstitial (•)

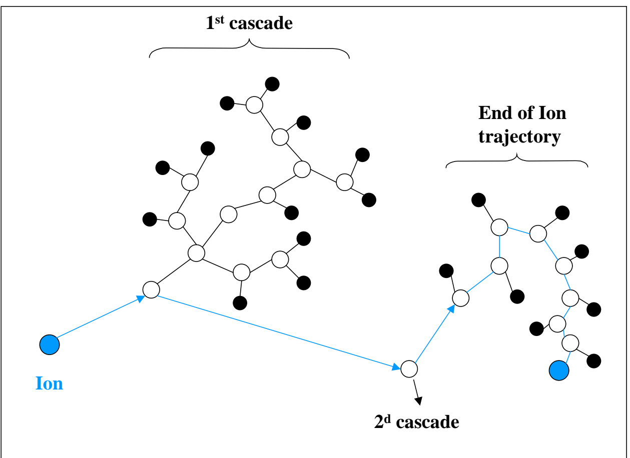

It can be calculated that the kinetic energy of the ion should be above the threshold for damage production as follows:

$$E_{th} = \frac{E_d}{G(m,M)} \tag{2.1}$$

where E_d is the displacement energy and $G(m,M) = \frac{4mM}{(m+M)^2}$ is the factor for maximum energy transfer in a single collision of ion (mass m) with the atoms (mass M) of the material. In crystalline semiconductors this energy is usually in the range 10 to 40 eV. If the energy of the incoming ion is less, it will just transfer some energy to the lattice in form of phonon excitation.

Electronic stopping is the transfer of kinetic energy from the ion to the target electrons by Coulomb force, resulting in excitation and ionization of target atoms. This process dominates for incident ion velocities higher than the one of the outer orbiting electrons. This mechanism is known as inelastic collision or electron excitation and ionization. In fact, for ion implantation, both types of energy transfers occur simultaneously in time and space and therefore are difficult to dissociate.

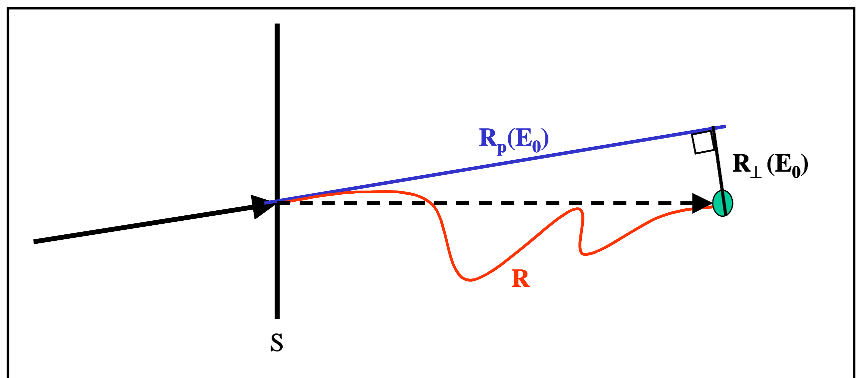

Figure 2.3: Difference between the path length (R) and the projected range (R_p).
The dashed arrow represents the penetration depth.

The implanted particle follows a complex trajectory, since its direction changes after each collision, and loses its kinetic energy progressively until it stops within the material. Of course it is important to know where the ions stop and thus the path length (R) of the particle can be calculated. However, the range projected on the initial direction of the particles is a much more relevant quantity for implantation (see Fig.2.3). This is the so-called projected range (R_p). The projection of R_p along the normal to the surface of the target is the penetration depth. Since each implanted ion experiences random collisions, the value of the path is statistically scattered. This is represented by the straggling ΔR_p. The ion trajectories and energy losses can be calculated with software such as SRIM 2000 [Ziegler *et al.*1985] (see Fig.2.4).

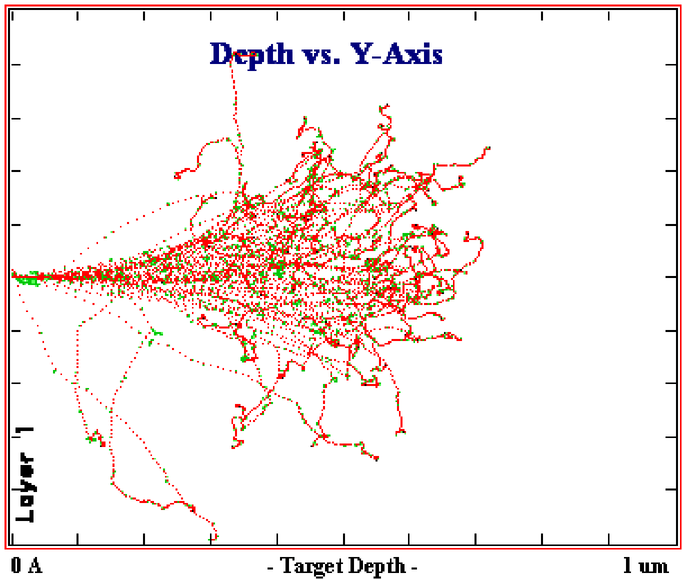

Figure 2.4: Ion trajectories calculated by SRIM 2000 [Ziegler *et al.*1985] for He implantation in silicon at 50 keV.

The as-created vacancies and interstitials are mobile at room temperature (in the case of silicon) and can either recombine, be trapped at higher order defects such as stacking faults or dislocations, or form other defect complexes. In the case of heavy ions or high dose implantation, defect clusters, regions of high defect density, or even amorphous regions will be created leading to strain and local Fermi level changes for example. These defect rich-regions will permit the formation of three layers device structure.

Ion implantation is a key process for the introduction of dopants in the semiconductor industry. Post implantation heat treatments are necessary to remove implantation damage and/or to activate dopants. This is one of the major drawbacks of this technique. Quantitative prediction of the as-induced defects is still lacking. It is however necessary to control them in order to optimize either their use in "Defect Engineering" or to suppress some undesirable

effects such as transient-enhanced diffusion (TED). TED of dopants in silicon has been shown to be connected to the supersaturation of self-interstitials contained in {311} defects [Stolk *et al.* 1997]. Even if some aspects of their generation are still quite unexplored, it seems established that some configurations of interstitials clusters are more stable than others and are able to grow via Oswald ripening process [Colombeau *et al.* 2001]. A non-negligible effect of ion implantation is also doping compensation, i.e. a decrease in the free-carrier density. Deep levels associated with defects acting as trapping centers can be introduced in the bandgap. This is particularly true in SiC where a very high compensation is observed even in the case of low dose irradiation. This compensation is found to increase strongly with nitrogen concentration [Åberg *et al.* 2001]. The future application of these IV-IV compound materials relies heavily on a proper control of the implantation parameters/conditions. A new application of ion damage could be the formation of nanocavities which appear to be promising as a gettering technique in Si. Some aspects of the formation of cavities in the case of helium implantation have been studied in this thesis.

2.2 The Helium-Silicon system

The properties of single He atoms or small clusters in the silicon lattice are the basis for any fundamental understanding of helium effects. The crucial parameters are the energies of He atoms at different sites in perfect and imperfect lattices since they determine the solubility, the paths of migration, the trapping at defects and the early stages of cluster formation. The most stable position of helium in silicon is the interstitial position. *Ab initio* molecular dynamics [Alatalo *et al.* 1992] and RBS (Rutherford Backscattering) measurements [Allen 1985] have shown that the helium sits preferentially in a tetrahedral interstitial site (T_d) which is the lowest energy configuration (Fig.2.5). The solution enthalpy and the migration energy of interstitial helium in silicon, calculated or measured by diverse techniques, are shown in Table.2.1.

H_S (eV)	**E_{mig} (eV)**	**Methods**	**Source**
0.77	0.84	*ab initio* MD	[Alatalo *et al.* 1992]
0.46	1.34	permeation	[Weringen *et al.* 1956]
0.90	0.80	desorption	[Jung *et al.* 1994]

Table 2.1: Solution enthalpy and migration energy of interstitial helium in silicon calculated or measured by diverse techniques.

Moreover, helium atoms have a tendency to occupy adjacent T_d sites to form complexes. On the other hand an He atom is not stable in a single vacancy [Allen 1985, Alatalo *et al.* 1992]. The helium diffusion, i.e. its motion from one interstitial site to another, occurs via a zigzag path through the interstitial sites (Fig.2.6).

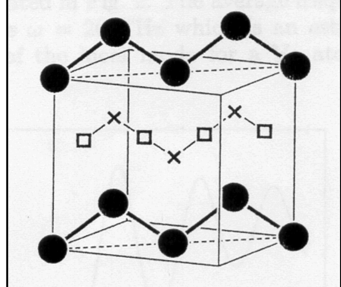

Figure 2.6: Schematic representation of the [110] plane of Si: Si atoms (•), tetrahedral interstitial site (×), hexagonal interstitial site (□). The He migration path is a zigzag line through the interstitial sites. (See [Alatalo *et al.* 1992])

The simple diffusion coefficient of interstitial helium in silicon can be written as follows:

$$D_{He} = D_0 \exp(-E_{mig}/kT) \quad (2.2)$$

where E_{mig} is the migration energy, k the boltzmann constant, and $D_0 = \nu d^2$ with ν the helium vibration frequency in an interstitial site ($\nu = 2 \times 10^{13}$ s^{-1}) and d the distance between two adjacent T_d sites (d = 1.62 Å). A typical value of D_{He} at 300 K is of 4×10^{-17} cm^2/s.

Estreicher *et al.* [1997] have confirmed that helium is dissolved in interstitial position and is repelled by the isolated vacancy, but they have also showed that helium can be exothermically dissolved in the divacancy.

- **Potential energy of the system He-Si:**

The formation energy of interstitial helium E_{form}^{He} and the formation and migration energies of a vacancy, a self-interstitial, can be predicted by atomistic calculations or obtained by permeation/desorption measurements. These data are shown in Table.2.2 and are schematically represented in the potential energy diagram (Fig.2.7).

Defect	E_{mig} (eV)	E_{form} (eV)	Source
He	1.34	0.46	[Weringen *et al.* 1956]
Vacancy	0.37	3.19	[Baskes *et al.* 1989]
Self-interstitial	-	4.81	[Baskes *et al.* 1989]

Table 2.2: Formation energy and migration energy of point defects in silicon given by the literature.

A direct consequence is that the dissociation energy of helium from any defect in silicon should not exceed 1.7 eV, assuming that the van der Waals binding of helium with silicon can be neglected. However, during high dose or high energy ion implantation, many point defects are created which change the state and mobility of helium. Thus the behaviour of helium in the implanted silicon is different than in the silicon free of defects.

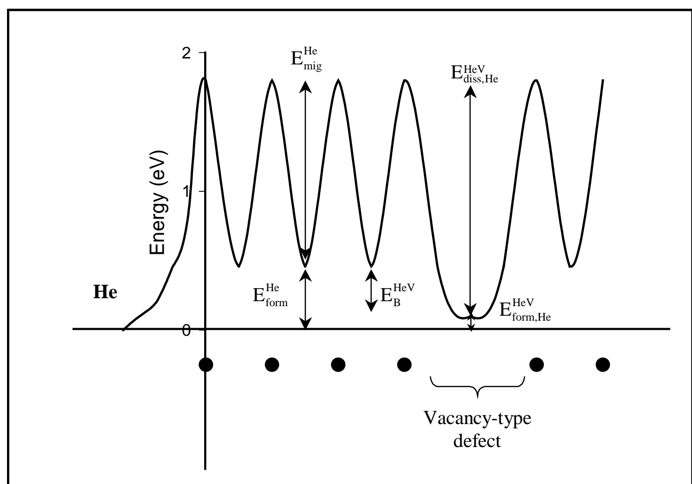

Figure 2.7: Potential energy diagram of helium in interaction with silicon. Helium at an interstitial position and helium at a vacancy are indicated. E^{He}_{form}, E^{He}_{mig} : formation and migration energies of interstitial He, $E^{HeV}_{form,He}$, $E^{HeV}_{diss,He}$: formation and migration energies of helium in interaction with a vacancy-type defect, E^{HeV}_{B} : bending energy of He with a vacancy-type defect.

2.3 Low dose He implantation

The interstitials and vacancies which survive mutual recombination or annihilation at microscopic sinks are stabilized by pairing themselves or by interacting with impurity atoms. The divacancy V_2 is one of the prominent defects appearing after particle irradiation. There are other two electrically active defects which are always found: the vacancy-oxygen complex (VO or A-center) and the interstitial carbon oxygen complex (C_iO_i). Carbon and oxygen are the unintentionally introduced impurities of highest concentrations. The group V elements (dopants) can also be paired with migrating vacancies giving rise to the so-called E-center (VP). Moreover, some of the implanted ions can form defects, during both the implantation and subsequent annealing treatment.

The implantation of light ions in silicon has received much attention over the last years because of the new interest involved in the control of minority carrier lifetime in the active

region of power devices. Deep levels can be thus locally introduced at a controlled depth. Reproducibility of dose and doping distributions are the great advantages of irradiation compared to conventional in-diffusion into the wafer. In the case of proton implantation, harmful effects such as the introduction of shallow donors can drastically affects the blocking voltage V_B [Barbot *et al.*1995]. In the case of helium irradiation, no shallow levels are formed but to reach the same depth the helium ion must have about 4 times higher energy than the proton. Helium irradiation also creates more damage per ion (10 times more), but the defect distribution is much narrower. The defect concentration in the tail is substantially lower than for the proton case.

The combination of implantation and diffusion has emerged as an alternative solution for minority carrier lifetime control in silicon devices. It was proposed to use low doses helium implantation in silicon to lower the diffusion temperature of platinum or gold. In fact, during implantation, point defects are created that will act as gettering centers for the further platinum diffusion. Implantation-induced defects due to low dose helium implantation have been studied by deep level transient spectroscopy (DLTS) [Schmidt *et al.* 1997]. In Fig.2.8, a DLTS spectrum of silicon diode implanted with 3.4 MeV He at a dose of $8x10^{11}$ cm^{-2} is presented. Six majority deep levels located at 0.17, 0.23, 0.35, 0.43, 0.56 and 0.64 eV from the conduction band are contributing to the DLTS spectrum. Their characteristics are presented in table.2.3.

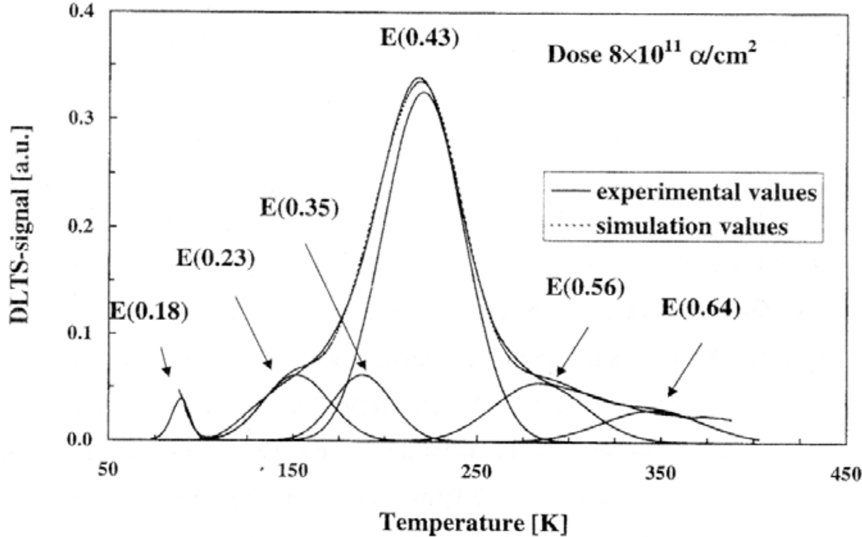

Figure 2.8: DLTS spectrum after helium implantation (3.4 MeV, $8x10^{11}$ cm^{-2}) in silicon. A reverse bias of -6V and a trap filling voltage of -0.2V were used. See ref. [Schmidt *et al.* 1997]

Energy level position (eV)	Defect identification	Capture cross-section (cm^2)
E_C-0.18	$(V\text{-}O)^{(0/-)}$ (A-center)	$1x10^{-14}$
E_C-0.23	$(V\text{-}V)^{(-/--)}$	$1x10^{-15}$
E_C-0.35	impurity-related	$1x10^{-15}$
E_C-0.43	$(V\text{-}V)^{(0/-)} + (V\text{-}P)^{(0/-)}$	$1x10^{-15}$
E_C-0.56	multivacancies ?	$8x10^{-16}$
E_C-0.64	multivacancies ?	$4x10^{-15}$

Table 2.3: Deep levels observed in n-type silicon after He implantation (3.4 MeV, $8x10^{11}$ cm^{-2}).

The concentration of these stable defects depends on implantation parameters (energy, dose, dose rate, temperature). Their thermal stability also differs. However, after annealing at 350°C for 15 min all defects seem to disappear or at least are at too low concentration to be detected using conventional techniques.

The different processes operative during implantation and giving rise to the generation of stable defects are schematically represented as follow:

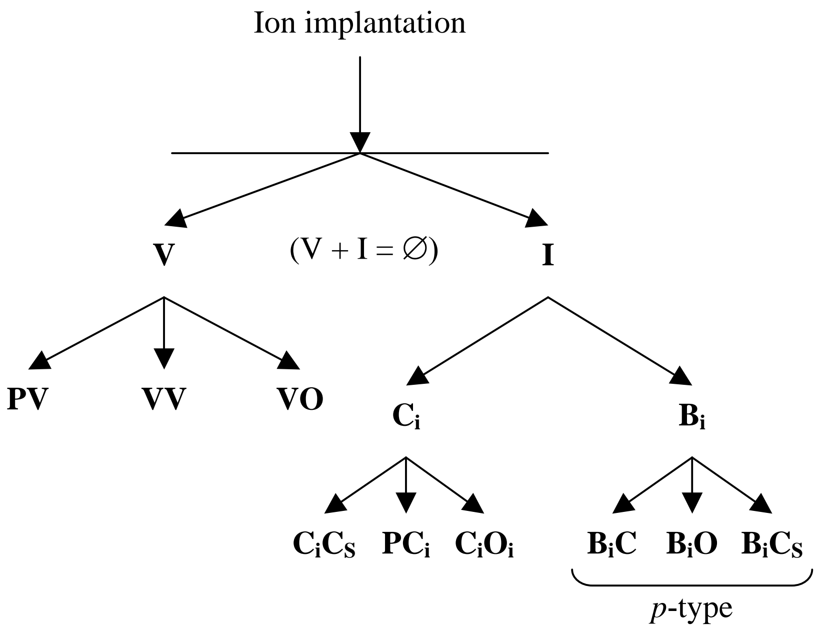

2.4 High dose He implantation

It is now well known that high dose helium implantation into silicon leads to the formation of bubbles. Due to its extremely low solubility, He segregates into small gas-vacancy complexes and forms bubbles. During the annealing at temperatures above 700ºC, bubbles grow while He is released from bubbles by gas out-diffusion, leading to void formation, i.e. cavities. This phenomenon was first observed in 1987 by Griffioen *et al.* in Si implanted at high He dose and low energy ($2x10^{17}$ cm^{-2} and 10 keV). More recently, Follstaedt *et al.* [1996] have demonstrated that He-induced cavities can trap metallic impurities by a chemisorption process at their internal surfaces. Since then, many studies have been carried out in this field with the aim of developing proximity gettering techniques for very large scale integration (VLSI) applications. Most of these studies have concentrated on high dose implants producing a high density of cavities. A recent overview of void formation and evolution in He implanted silicon has been published [Raineri *et al.* 2000]. All these implantations have been done using keV energies, leading to a damaged layer in the vicinity of the implanted surface (< 1 μm). A typical TEM image of the buried layer containing bubbles, obtained after keV implantation in silicon is shown in Fig.2.9. In fact, high dose He implantation results in a uniform and dense layer of small helium bubbles located at the Rp region.

Figure 2.9: TEM image of helium implanted silicon at 50 keV and $5x10^{16}$ cm^{-2}, no anneal. See ref. [David *et al.* 2001]

Bubble sizes are typically of few nanometers. The surrounding dark contrast is due to the lattice damage but no extended defects are observed as in most of the as-implanted samples.

Figure 2.10: TEM image of helium implanted silicon at 50 keV and $5x10^{16}$ cm^{-2} after annealing at 800°C for 30 min. See ref. [Oliviero 1999]

Annealing at 800°C for 30 min increases the cavity sizes as seen in Fig.2.10 and a well-defined cavity layer is observed. The cavities can be either spherical or faceted. The sizes, shapes and density of cavities strongly vary with annealing parameters. Many experiments have been carried out to study the annealing behavior of bubbles [Follstaedt *et al.* 1993, Raineri *et al.* 2000]. In this energy range (keV), voids are found to be effective sinks for point defects, resulting in the suppression of the secondary defects such as dislocations [Raineri *et al.* 1996]. Even if {113} defects and dislocations connected to cavities can be observed following implantation at keV energies, they are located close to the bubbles and dissolve during the first minutes of annealing to fill up the smallest cavities [Roqueta *et al.* 1999]. In any case no dislocations extending upward through the cavity-free region have been found.

It is obvious that the damage morphology and its evolution during annealing will depend on the range of implantation energies. Thus, in the case of MeV implantation, a different damage morphology is expected. In particular, helium desorption from bubbles should be more difficult with increasing energy, since the rate of desorption has been shown to be depth dependent [Griffioen *et al.* 1987]. The release of He should be less influenced by the proximity of the surface. This has been recently confirmed by Non Rutherford elastic Backscattering (NRBS) experiments where 90 % of helium has been found to stay in bubbles

after annealing at 800°C for 30 min in 1.6 MeV He implanted silicon [Godey *et al.* 2000]. A preliminary study was carried out in order to investigate this particular MeV implantation regime [Oliviero 1999]. As observed for the keV range, high dose implantation using MeV energies leads to the formation of a dense and uniform bubble layer located near R_p. The sizes of bubbles are also of order 1 nm but the bubble band is wider (Fig.2.11).

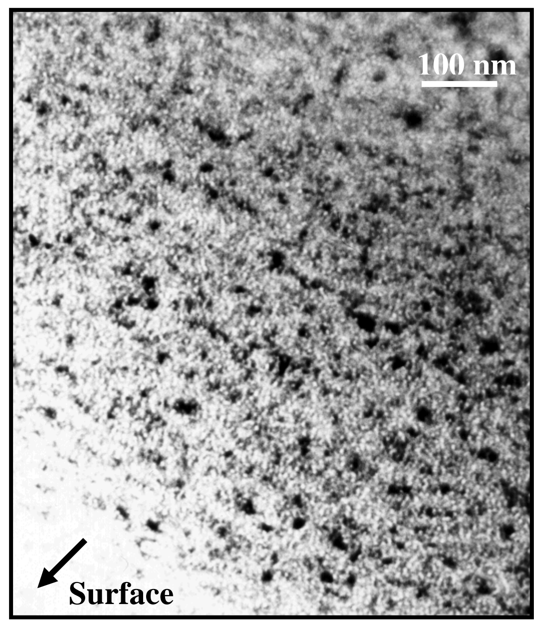

Figure 2.11: TEM image of helium implanted silicon at 1 MeV and $5x10^{16}$ cm^{-2}. See ref. [Oliviero 1999]

Annealing at 800°C for 30 min allows not only bubble growth but also extended defect nucleation [Oliviero 1999, Beaufort *et al.* 2000, Oliviero *et al.* 2001]. As seen in Fig.2.12, bubbles/voids of different sizes form a well-defined band. Behind this band a high concentration of elongated defects along <110> directions extend up to 500 nm toward the bulk. These elongated defects are the well-known {311} defects, or “rod-like” defects.

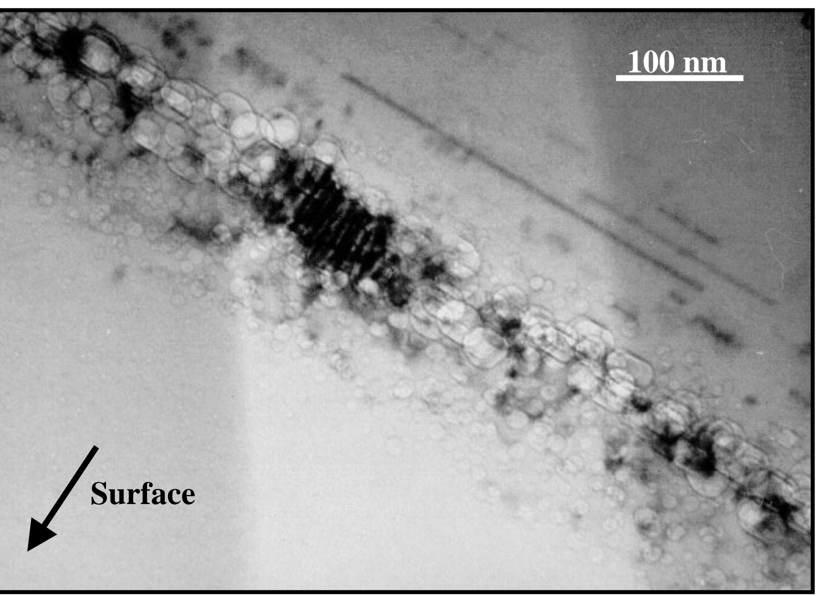

Figure 2.12: TEM image of helium implanted silicon at 1 MeV and $5x10^{16}$ cm^{-2} after annealing at 800°C for 30 min. See ref. [Oliviero 1999]

These defects consist of an agglomeration of excess Si self-interstitials and are known to form in response to the nonequilibrium injection of interstitials resulting from ion implantation. It is generally recognized that {311} interstitial clusters have an anisotropic, elongated shape. For a detailed discussion on the structural properties of {311} defects, the reader is referred to a recent review article by Takeda and co-workers [Takeda *et al.* 1994]. Frank loops are also present in the vicinity of the bubble band. Thus while creating bubbles or voids using MeV energies, numerous extended defects are also generated.

This preliminary work has shown that the effects of MeV implantation are totally different to those due to keV implantation and thus MeV implantations will be at the centre of a detailed study presented in the following chapters.

2.5 Medium dose implantation

Medium dose implantation (>$1x10^{15}$ and <$5x10^{16}$ cm^{-2}) have been mainly studied by Fichtner *et al.* [1997]. These implantations lead to "diluted systems" in order to distinguish them from the above mentioned condensed ones. In this regime, defects created are found to be not uniformly distributed. For example, a diluted system of spherical cavities in silicon (Fig.2.8a) has been reported in the case of a 40 keV helium implantation at a dose of $1x10^{16}$ cm^{-2}, followed by annealing at 800°C for 10 minutes [Fichtner *et al.* 1997]. The observed cavity arrangement consists of a large central cavity surrounded by ring of smaller cavities (Fig.2.8b). This "planetary-like" cavity configuration induces a strong strain field in the surrounding matrix and thus emits dislocations loops (Fig.2.8c). To explain this strain field, the authors state that the bubbles are in an overpressurized state, i.e. the gas pressure inside the bubble exceeds the thermodynamic equilibrium condition (the gas pressure inside the bubble is not balanced by the surface free energy of the surrounding matrix).

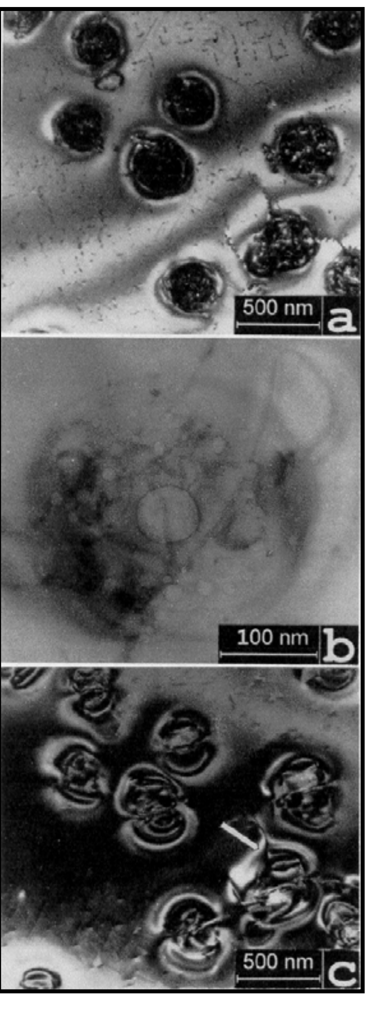

Figure 2.8: Plan view TEM micrograph showing a diluted cavity system resulting from a 40 keV, 1×10^{16} cm^{-2} He implantation after annealing at 800°C for 10 min. **(a)** General appearance of the cavities along with dislocation loops. Analysis conditions: dynamic bright field image with electron beam parallel to the <100> axis, multibeam, underfocus. **(b)** A typical large cavity surrounded by a ring of smaller ones. Analysis conditions: kinematic bright field image, underfocus. **(c)** Strain field contrast around the cavities and dislocation loops (pointed by an arrow) emerging from the cavities. Analysis conditions: dynamic bright field with electron beam close to the <100> direction, ***g*** = 400, underfocus. (See ref. [Fichtner *et al.* 1997]).

For the same implantation conditions but with an energy of 10 keV, a diluted system of large cavities located in a buried layer at of 100 nm (near the R_p) is also created The variation of implantation energy seems to only affect the cavity sizes and morphologies. In both case, a buried layer of dislocation loops is observed (Fig.2.8a).

The same authors [Fichtner *et al.* 1999] also report two-dimensional structures showing distinct morphological developments with respect to the annealing temperatures (Fig.2.9). For temperatures less than 400°C, plate-like cavities surrounded by a strain field are formed (Fig.2.9a) whereas for temperatures in the range 400°C-470°C cavities switch to the "planetary-like" configuration (Fig.2.9b). In the range 470°C-700°C the "planetary-like" configuration is kept but the central cavity become ellipsoid-like.

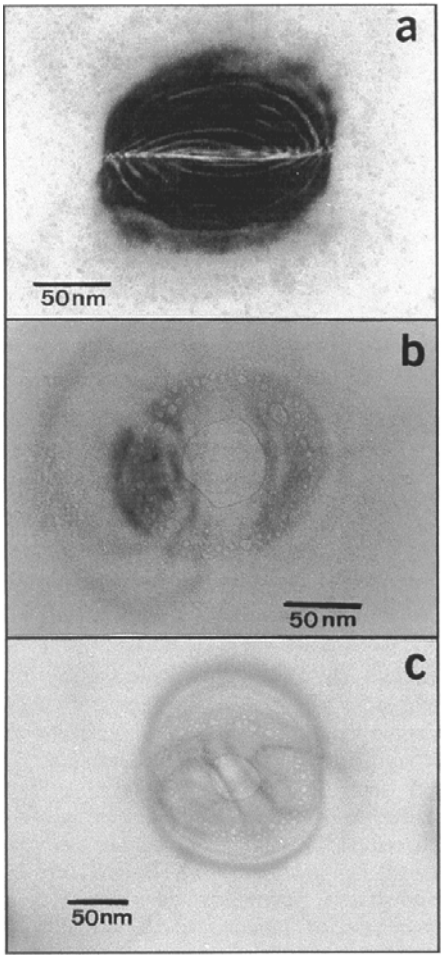

Figure 2.9: TEM micrograph showing typical cavity shapes resulting from a 30, 60 and 120 keV He multi-implantation, at a dose of $5x10^{15}$ cm^{-2} (for each energy) and annealing at various temperatures for 10 min. **(a)** Plate-like structure observed at 370°C. Note the strain induced contrast. Analysis conditions: dynamic BF image with e-beam parallel to the <116> direction. **(b)** Face-on view of a plate-like structure observed at 400°C. **(c)** Ellipsoid-like structure observed at 600°C. Analysis conditions: kinematic BF image with e-beam close to the <100> direction, underfocus. (See ref. [Fichtner *et al.* 1999])

For higher temperatures (T ≥ 800°C), they obtain spherical-like cavities arranged within planar clusters oriented along {100} planes (Fig.2.10).

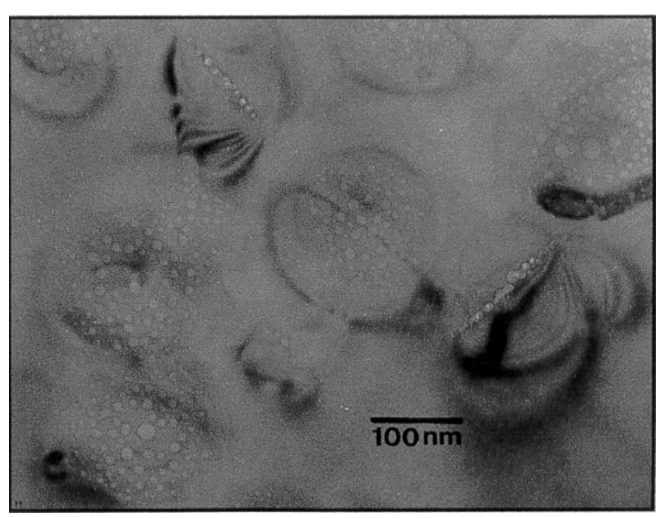

Figure 2.10: TEM micrograph showing a diluted cavity system resulting from a 40 keV, $1x10^{16}$ cm^{-2} He implantation after annealing at 800°C for 30 s. Spherical-like cavities are arranged within planar clusters oriented along {100} lattice planes. Note also the edge-on clusters. Analysis conditions: kinematic BF image with e-beam close to the <100> direction, underfocus. (See ref. [Fichtner *et al.* 1999]).

The plate-like structures as in Fig.2.9a may be formed either at low temperatures (e.g. T ≈ 300°C) or within very short annealing times at higher temperatures. Their nucleation occurs preferentially at the {100} or {110} planes of the Si lattice.

Moreover, Raineri *et al.* [1995] have also investigated bubble formation for 40 keV He implantation at a dose of $1x10^{16}$. After annealing at 800°C for 1 hour, they observe voids with a mean diameter of 13 nm but no diluted system are reported.

2.6 Methods of study

The recent progress in semiconductor technology implies an quantitative control of defects, both intrinsic (vacancies, interstitials, anti-site defects) and extrinsic (dopants, impurity atoms) . This requires techniques that are able to detect defects at constantly decreasing concentrations. The ability of identifying very low defect concentrations is the strength of spectroscopic techniques.

Numerous techniques are available to characterise implantation-induced defects in semiconductors (Table.2.4). Their efficiency will depend on the type of defect studied, its concentration and its size, as well as the implantation dose regime selected. For low doses (< $1x10^{13}$) the most powerful technique is deep level transient spectroscopy (DLTS) [Barbot *et al.* 1995]. However, this technique is only sensitive to electrically active defects. With a sensitivity of about 10^{-5} times the background doping, DLTS allow the determination of the energy positions in the band gap, the charge carrier capture cross-section and the concentrations of defects. Nevertheless, the identification of the "unknown" defects is not straightforward, and for that a combination with other techniques is needed. Other powerful techniques in the low dose regime are photo-luminescence (PL), positron beam analysis (PBA), Rutherford backscattering (RBS) and thermal helium desorption spectrometry (THDS). PL is also sensitive to electrically active defects but needs a higher defect concentration than DLTS. PBA is very powerful for the study of vacancy-type defects, since positrons are sensitive to open volumes. They can detect from monovacancies to cavities [Brusa *et al.* 1999]. As seen before, RBS can be used to localize single He atom [Allen 1985]. This technique is more sensitive to interstitial-like defects. THDS has the most extended range since it can be used in the case of low doses to study defect precursors but also for high doses to characterise the defects [Van Veen 1991]. The dissociation energy of small defects as

well as the helium content can be determined. The most widely used experimental method for the investigation of medium and high doses is of course transmission electron microscopy (TEM) that allows the direct imaging of the induced defects. With deeper analysis qualitative and quantitative information can be derived from TEM studies such as defect nature, density, depth profile… Other techniques such as EELS (Electron energy loss spectroscopy) [Hojou *et al.* 1996] or XRD (X-ray diffraction) have been successfully used and yield valuable complementary information such as local concentration and strain respectively [Declemy *et al.* 2002]. Non-Rutherford elastic backscattering (NREBS), neutron depth profiling (NDP) and nuclear reaction analysis (NRA) were used also to detect the amount of helium retained in the sample [Godey *et al.* 2000]. ERD (elastic recoil detection) can be used to obtain the helium depth profile as well as the helium content [Kaschny *et al.* 1998]. C-RBS (channeling Rutherford backscattering) has been used to analyse and depth-profile the cavities [Moons *et al.* 1997] and to determine the amount of impurities present in the gettering sites [Raineri *et al.* 1995]. Spectroscopic ellipsometry (SE) can provide information on the volume fraction and depth distribution of cavities [Fukarek *et al.* 1999]. Atomic force microscopy (AFM) can give information on the modification of the surface and the change in volume, i.e. the swelling induced by the formation of cavities.

<table>
<tr><th></th><th colspan="2">Single He atom and small He_nV_m clusters</th><th colspan="3">Properties of He-bubbles and related defects</th><th colspan="2">Macroscopic defects</th></tr>
<tr><td>He-atoms, n</td><td>1</td><td>~5-10</td><td>~50-100</td><td>~2.10^4</td><td>~10^6</td><td colspan="2">Blisters, cracks,</td></tr>
<tr><td>Vacancies, m</td><td>0/1</td><td>~5</td><td>~50</td><td>~5.10^4</td><td>~5.10^7</td><td colspan="2">Steps</td></tr>
<tr><td>Typical dimensions</td><td>0.2 nm</td><td>0.5 nm</td><td>1 nm</td><td>10 nm</td><td>100 nm</td><td>1 µm</td><td>1 mm</td></tr>
<tr><td>Theory</td><td colspan="2">Computer simulation</td><td colspan="3">Statistical mechanics</td><td colspan="2">Fracture mechanics</td></tr>
<tr><td>Experiment</td><td colspan="5">THDS</td><td colspan="2"></td></tr>
<tr><td></td><td colspan="2"></td><td colspan="3">TEM</td><td colspan="2">SEM</td></tr>
<tr><td></td><td colspan="5"></td><td colspan="2">AFM</td></tr>
<tr><td></td><td colspan="2"></td><td colspan="3">EELS</td><td colspan="2"></td></tr>
<tr><td></td><td colspan="5">PBA</td><td colspan="2"></td></tr>
<tr><td></td><td colspan="2"></td><td colspan="3">XRD</td><td colspan="2"></td></tr>
<tr><td></td><td colspan="5">DLTS</td><td colspan="2"></td></tr>
<tr><td></td><td colspan="3">RBS</td><td colspan="4"></td></tr>
</table>

Table 2.4: Different techniques used to study helium implantation induced defects.

2.7 Conclusion

Ion implantation is already a major technique in semiconductor processing technology. Its potential is again highlighted by new applications such as the control of minority carrier lifetime and the gettering of impurities for further technological innovations. The effects of implantation in crystalline materials have been described. He implantation being the main theme of this study, the He-silicon system has been described in details. For a better understanding of the process, the implantation has to be divided into three different dose regimes: the low, high and medium doses. For low doses, He implantation produces mainly divacancies and/or small vacancy-clusters. For high doses, He implantation yields the formation of a buried layer containing bubbles which can grow during subsequent annealing. Extended defects such as dislocations and “rod-like” defects can be observed depending on the implantation and annealing parameters. Moreover it was underlined that the implantation energy range should be taken into account. A preliminary study has shown that keV and MeV implantations lead to different defect structures. For the medium doses, He implantation leads to diluted systems. The formation and morphology of defects seems to dramatically depend on the implantation and annealing parameters. Various techniques are available to study the implantation effects. Of course the best approach is to combine them since their efficiency depends on the type of defect, its concentration and size as well as the implantation dose regime.

References

[Åberg *et al.* 2001] D. Åberg, A. Hallén, P. Pellegrino, B.G. Svensson, *Appl. Phys. Lett.* **78**, 2908 (2001).

[Alatalo *et al.* 1992] M. Alatalo, M.J. Puska, R.M. Nieminen, *Phys. Rev. B* **46**, 12806 (1992).

[Allen 1985] W.R. Allen, *Mat. Res. Soc. Symp. Proc.* **279**, 433 (1993).

[Barbot *et al.*1995] J.F. Barbot, E. Ntsoenzok, C. Blanchard, J. Vernois, D.B. Isabelle, *Nucl. Instr. Methods Phys. Res. B* **95**, 213-218 (1995).

[Brusa *et al.* 1999] R.S. Brusa, G.P. Karwasz, N. Tiengo, A. Zecca, F. Corni, G. Calzolari, C. Nobili, *J. Appl. Phys.* **85**, 2390 (1999).

[Baskes *et al.* 1989] M.I. Baskes, J.S. Nelson, A.F. Wright, *Phys. Rev. B* **40**, 6085 (1989).

[Beaufort *et al.* 2000] M.F. Beaufort, E. Oliviero, H. Garem, S. Godey, E. Ntsoenzok, C. Blanchard, and J.F. Barbot, *Phil. Mag. B* **80**, 1975 (2000).

[Colombeau *et al.* 2001] B. Colombeau, F. Cristiano, A. Altibelli, C. Bonafos, G. Ben Assayag, A. Claverie, *Appl. Phys. Lett.* **78**, 940 (2001).

[David *et al.* 2001] M.L. David, M.F. Beaufort, J.F. Barbot, to be published (2001).

[Declemy *et al.* 2002] A. Declemy, E. Oliviero, M.F. Beaufort, J.F. Barbot, M.L. David, C. Blanchard, Y. Tessier, E. Ntsoenzok, accepted in *Nucl. Instr. Methods Phys. Res. B* (2002).

[Estreicher *et al.* 1997] S.K. Estreicher, J. Weber, A. Derecskei-Kovacs, D.S. Marynick, *Phys. Rev. B* **55**, 5037 (1997).

[Fichtner *et al.* 1997] P.F.P. Fichtner, J.R. Kaschny, R.A. Yankov, A. Mücklich, U. Kreiβig, W. Skorupa, *Appl. Phys. Lett.* **70**, 732 (1997).

[Fichtner *et al.* 1999] P.F.P. Fichtner, J.R. Kaschny, M. Behar, R.A. Yankov, A. Mücklich, W. Skorupa, *Nucl. Instr. Methods Phys. Res. B* **148**, 329-333 (1999).

[Follstaedt *et al.* 1993] D.M. Follstaedt, S.M. Myers, H.J. Stein, *Mat. Res. Soc. Symp. Proc.* **279**, 105 (1993).

[Follstaedt *et al.* 1996] D.M. Follstaedt, S.M. Myers, G.A. Petersen, J.W. Medernach, *J. Electron Mater* **25**, 157 (1996).

[Fukarek *et al.* 1999] W. Fukarek, J.R. Kaschny, *J. Appl. Phys.* **86**, 4160 (1999).

[Godey *et al.* 2000] S. Godey, T. Sauvage, E. Ntsoenzok, M.F Beaufort, J.F. Barbot, B. Leroy, *J. Appl. Phys.* **87**, 2158 (2000).

[Godey *et al.* 2000] S. Godey, E. Ntsoenzok, T. Sauvage, A. Van Veen, F. Labohm, M.F Beaufort, J.F. Barbot, *Mat. Scie. Eng. B* **73**, 54 (2000).

[Griffioen *et al.* 1987] C.C. Griffioen, J.H. Evans, P.C. De Jong, A. Van Veen, *Nucl. Instr. Methods Phys. Res. B* **27**, 417 (1987).

[Hojou *et al.* 1996] K. Hojou, S. Furuno, K.N. Kushita, H. Otsu, Y. Furuya, K. Izui, *Nucl. Instrum. Methods Phys. Res. B* **116,** 382 (1996).

[Jung 1994] P. Jung, *Nucl. Instrum. Methods Phys. Res. B* **91**, 362 (1994).

[Kaschny *et al.* 1998] J.R. Kaschny, P.F.P. Fichtner, A. Muecklich, U. Kreissig, R.A. Yankov, W. Skorupa, *Nucl. Instrum. Methods Phys. Res. B* **136-138**, 583 (1998).

[Moons *et al.* 1997] R. Moons, W. Deweerd, H. Pattyn, A. Vantomme, G. Langouche, *Nucl. Instr. Methods Phys. Res. B* **127/128**, 379 (1997).

[Oliviero 1999] E. Oliviero, report for DEA in materials sciences, university of Poitiers (1999).

[Oliviero *et al.* 2001] E. Oliviero, M.F. Beaufort, J.F. Barbot, *J. Appl. Phys.* **89**, 5332 (2001).

[Raineri *et al.* 1995] V. Raineri, A. Battaglia, E. Rimini, *Nucl. Instr. Methods Phys. Res. B* **96**, 249 (1995).

[Raineri *et al.* 1996] V. Raineri, S.U. Campisano, *Appl. Phys. Lett.* **69**, 1783 (1996).

[Raineri *et al.* 2000] V. Raineri, M. Saggio, and E. Rimini, *J. Mater. Res.* **15**, 1449 (2000).

[Roqueta *et al.* 1999] F. Roqueta, A. Grob, J.J. Grob, R. Jérisian, J.P. Stoquert, and L. Ventura, *Nucl. Instrum. Methods Phys. Res. B* **147**, 298 (1999).

[Schmidt *et al.* 1997] D.C. Schmidt, J.F. Barbot, C. Blanchard, P. Desgardin, E. Ntsoenzok, G. Blondiaux, *Appl. Phys. A* **65**, 403-406 (1997).

[Stolk *et al.* 1997] P.A. Stolk, H.J. Grossmann, D.J. Eaglesham, D.C. Jacobson, C.S. Rafferty, G.H. Gilmer, M. Jaraiz, J.M. Poate, H.S. Luftman, T.E. Haynes, *J. Appl. Phys.*, **81**, 6031 (1997).

[Takeda *et al.* 1994] S. Takeda, M. Kohyama, K. Ibe, *Phil. Mag. A* **70**, 287 (1994).

[Van Veen 1991] A.van Veen, in: *Fundamental Aspects of Inert Gases in Solids*, NATO ASI series B, Physics 279, S.E. Donnelly, J.H. Evans (Eds), Plenum Publishing Corp., New York, pp 41-57, (1991).

[Weringen *et al.* 1956] A. van Weringen, N. Warmoltz, *Physica* **22**, 849 (1956).

[Ziegler *et al.*1985] J.F. Ziegler, J.P. Biersack, U. Littmark, *The Stopping and Range of Ions in Solids* (New York: Pergamon), (1985).

3-Helium bubbles and related defects in silicon

3.1 High energy implantation

The use of ion implantation with energies in the MeV range is steadily increasing in the fabrication of Si integrated circuits [Williams *et al.* 1993]. MeV implantation gives the opportunity to produce cavities in a well-defined region of the electronic devices. However, very few investigations have been performed to study their formation and their evolution upon annealing in this energy range. It is obvious that the damage morphology and its evolution are different depending on the range of energies. In particular, the helium desorption from bubbles should be more difficult with increasing energy since the rate of desorption is shown to be depth dependent [Griffioen *et al.* 1987]. This has been recently experimentally confirmed by Non Rutherford elastic Backscattering (NRBS) experiments where 90 % of helium has been found to remain in bubbles after an annealing at 800°C for 30 min in 1.6 MeV He implanted silicon [Godey *et al.* 2000]. While creating bubbles or voids, numerous extended defects are also generated. Extended defects are known to be associated with deep-lying electronic states in the band gap and thereby can affect the electronic properties of diodes. They can also be used as gettering centres [Ourmazd 1986]. So, in any case, their nucleation must be controlled.

3.1.1 Medium dose helium implantation

In this section, we study the formation of bubbles and of all the associated extended defects in the case of medium dose MeV implantation of helium in *n*-type silicon. We report on TEM observations showing new features of the micro-structural evolution of such cavity systems. A detailed study of the evolution of bubbles and their associated extended defects (dislocations) upon annealing is described. These results may provide a better comprehension of the He bubble nucleation and growth phenomena as well as of the formation of extended defects induced by the bubble growth process.

3.1.1.1 Experimental procedure

All experiments were carried out on commercial n-n^+ silicon wafers. The n-type layer, 75 μm thick, was epitaxially grown on a (111) oriented n^+ substrate of Czochralski silicon. The doping concentration of the n-region is $N_D = 2\text{x}10^{14}$ cm^{-3} (doped with phosphorus). These samples were implanted at room temperature with 1.6 MeV helium provided by a 3.5 MV van de Graff accelerator (CERI, Orléans), to a dose of 2x10^{16} cm^{-2}. The flux was 8.3x10^{12} cm^{-2}.s^{-1}. SRIM calculations [Ziegler *et al.* 1985] gives R_p = 5.5 µm and ΔR_p = 0.2 μm (Fig.3.1). Anneals were performed under nitrogen gas flow at 800°C for 30 min in a quartz tube within a tubular furnace. Cross-sectional Transmission Electron Microscopy was used to study the implantation-damaged region before and after annealing. The samples were cut, glued and then thinned using mechanical polishing and ion milling, for examination in the $[01\bar{1}]$ orientation. TEM images were obtained from a JEOL 200 CX operating at 200 kV. In the following, S in the TEM images denotes the implanted surface of the sample.

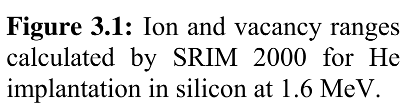

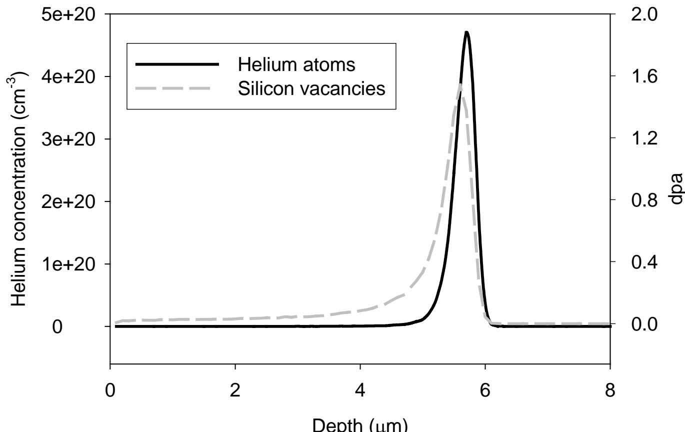

Figure 3.1: Ion and vacancy ranges calculated by SRIM 2000 for He implantation in silicon at 1.6 MeV.

3.1.1.2 Results and discussion

As-implanted

The Transmission Electron Microscopy (TEM) observations show that a uniform and dense layer of small helium bubbles is present in as-implanted samples (Fig.3.2). It is already known that for doses higher than 1x10^{16} cm^{-2}, bubble nucleation takes place during He implantation [Fichtner *et al.* 1999, Follstaedt *et al.* 1993]. This layer is approximately 1 μm in width. The center of the layer lies at 5.5 μm below the surface as expected using SRIM calculation. It was difficult to obtain a good contrast on the bubbles because of the surrounding dark contrast due to the lattice damage. However, helium bubbles can be seen as white spots with a dark edge for under focus condition and as dark centers with a white edge

for over focus condition. The average diameter of the bubbles is estimated to be close to 3 nm and the density to be about $2x10^{17}$ cm^{-3}. No extended defects are observed outside this buried layer.

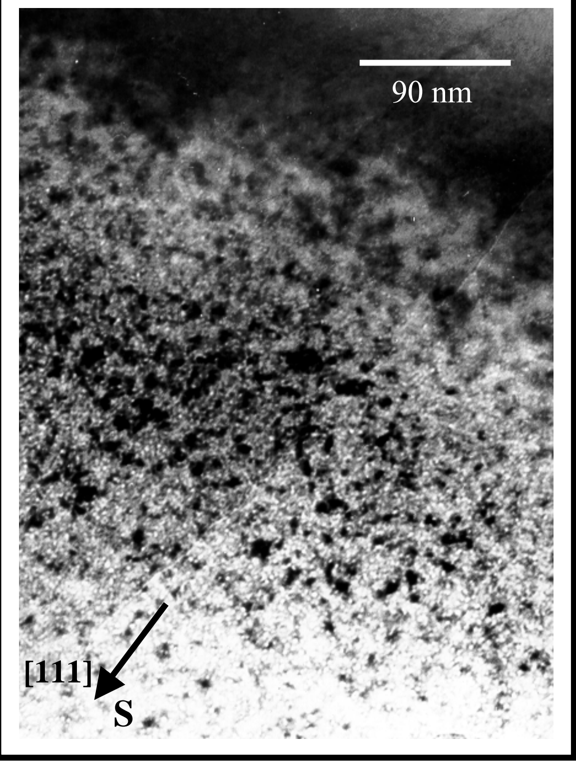

Figure 3.2: [01 $\bar{1}$] cross-section TEM micrograph of bubbles in the as-implanted silicon sample with helium at $2x10^{16}$ cm^{-2} and 1.6 MeV. Kinematical diffraction condition: underfocus.

After-annealing

Upon annealing the bubbles present in the as-implanted sample grow and cluster in a more well-defined layer, as expected from previous work [Fichtner *et al.* 1998]. However, the width of the buried layer is found to be reduced when comparing before annealing, but not in a symmetrical way around the R_p value (Fig.3.3). Indeed, before annealing the layer was centred on the R_p value whereas after annealing it is located below R_p. The part closest to the implanted surface has disappeared upon annealing. This phenomenon is attributed to the influence of the surface which acts as a sink for the defects.

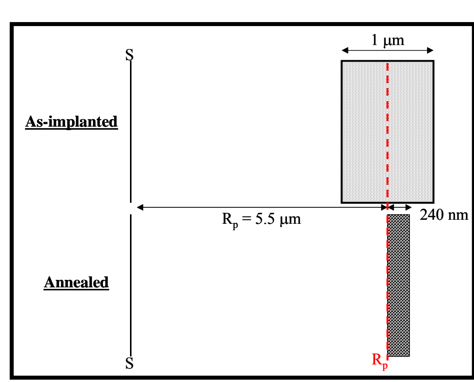

Figure 3.3: schematic view of the changes in width and location of the buried layer induced by the annealing at 800°C for 30 min.

General view

The general view of the damaged region (Fig.3.4), obtained at a low magnification in a cross-sectional image, shows that the 2x10^{16} cm^{-2} helium implantation followed by annealing

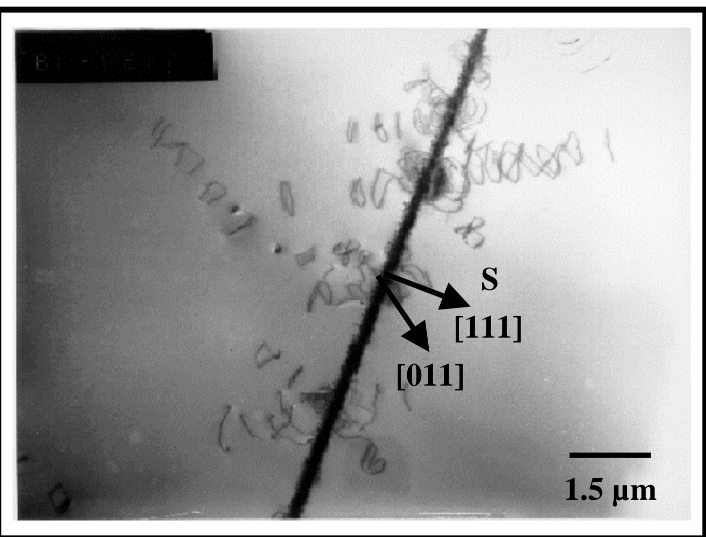

Figure 3.4: $[01\bar{1}]$ cross-section TEM image showing the damage region formed in Si after helium implantation with 2x10^{16} cm^{-2} at 1.6 MeV and annealing at 800°C for 30 minutes. Note the presence of rows of dislocations emerging from the band.

at 800°C for 30 min, gives rise to a continuous buried layer of about 300 nm width. We also observe stacking of dislocation loops appearing in rows in an orderly manner. The loops seem to be emitted from specific points randomly distributed within this layer. They can extend to the surface and 6 μm into the bulk. From Fig.3.4, it is obvious that they are generated along specific directions. In any one row, the loops appeared to be equally spaced and to have the same size. A comprehensive study of theses loops will be described below. Looking closer at the buried layer, a continuous band of small helium bubbles as well as small dislocation loops are observed. Clusters of bigger bubbles intersect this band (Fig.3.5).

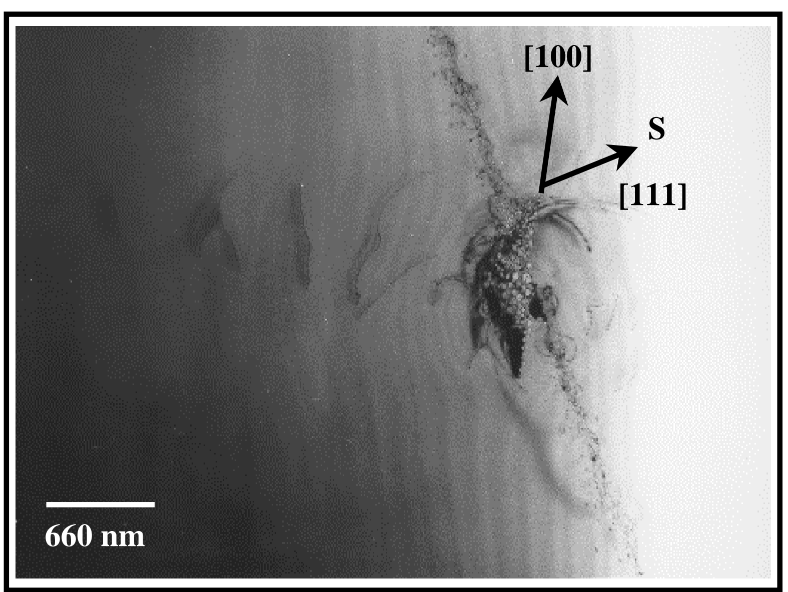

Figure 3.5: $[01\bar{1}]$ cross-section TEM picture obtained in Si after helium implantation at 1.6 MeV with 2x10^{16} cm^{-2} and heat treatment for 30 min at 800°C showing a cluster of bubbles that intersect the bubble layer. Kinematical diffraction condition: underfocus. Note that the cluster is oriented along a specific direction (100) and the presence of dislocations emerging from the cluster.

The clusters are randomly distributed along the bubble band and the rows of dislocation loops mentioned above are emerging from them. Moreover**,** the loops have the same size and shape as the related cluster. Thus, we can reasonably admit that these clusters act as loop sources. In the following, these different features will be described more in detail.

Buried layer

a) Bubble band

The bubble band has an average width of 240 nm (Fig.3.6) and lies about 5.6 μm deep from the surface (R_p = 5.5 μm using SRIM simulation). The bubbles within are spherical in shape and homogeneously distributed. The density is estimated to be of about $2x10^{16}$ cm^{-3}. The bubble diameters range from 7 nm to 22 nm, with a mean diameter of 12 nm. The pressure inside one of these bubbles is estimated to be in the range of 5 GPa using Mills, Liebenberg and Bronson (MLB) equation of state (EOS) of helium [Mills *et al.* 1980].

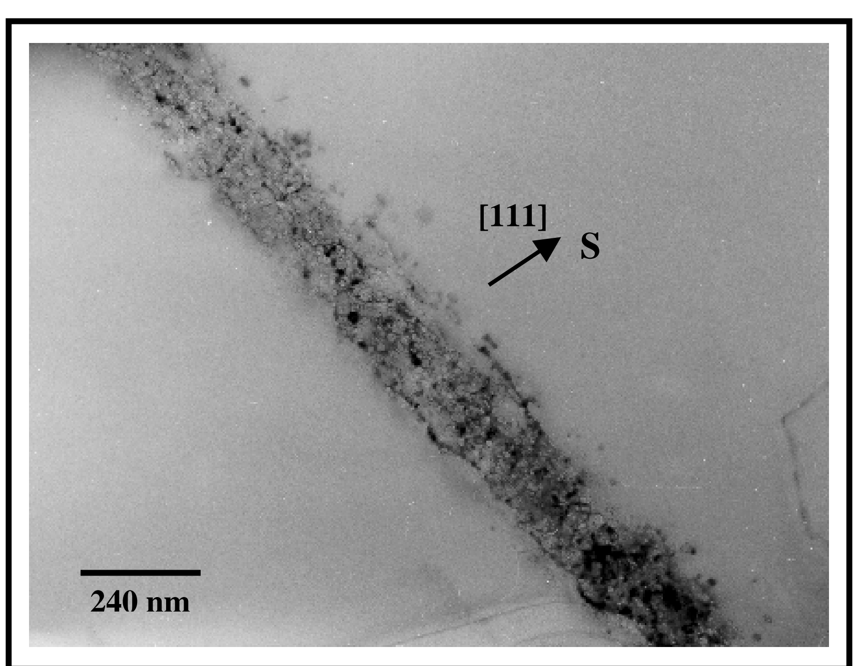

Figure 3.6: Bright field [$01\bar{1}$] cross-section TEM image showing the bubble band formed by a $2x10^{16}$ He/cm^2 implant in Si at 1.6 MeV after 30 min annealing at 800°C. Kinematical diffraction condition: underfocus.

b) Frank dislocation loops

As seen in Fig.3.6, small dislocation loops are also observed. They are present inside the band but most of them are lying below and along the bubble band. This explains why in the

low magnification image the buried band appears with a 300 nm width. Some of the loops lying next to the band were studied because they were easy to distinguish. They exhibit black/white contrast lobes in both bright and dark field images, particularly visible when imaged edge-on under dynamical two-beam conditions with the diffraction vector perpendicular to their habit plane. This behaviour is characteristic of Frank loops. Moreover, they show a fringe contrast for certain diffraction conditions. In the weak beam image of fig.3.7a, recorded with **g** = $\bar{1}11$ (**g**,**7g**), the fault fringes are visible inside the loops (indicated by arrows). An analysis with different diffraction vectors **g** has confirmed that they are Frank dislocation loops. Their mean radius is about $\bar{r}$ = 44 nm with a standard deviation σ = 14 nm. The +**g** and –**g** method, which will be described later, shows that they are interstitial in nature. They lie on {111} planes and all of them are also attached to bubbles (see Fig.3.7b).

Figure 3.7: (a) Dark field [01$\bar{1}$] cross-section TEM micrograph obtained in Si after helium implantation at 1.6 MeV with 2x10^{16} cm^{-2} and heat treatment for 30 min at 800°C, showing Frank loops (indicated by arrows) located behind the bubble band. **(b)** Frank loop bound to a bubble

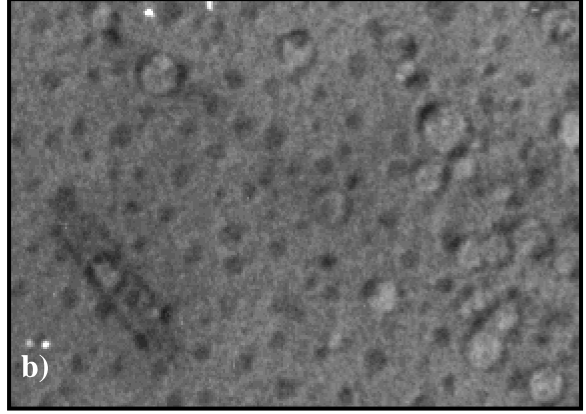

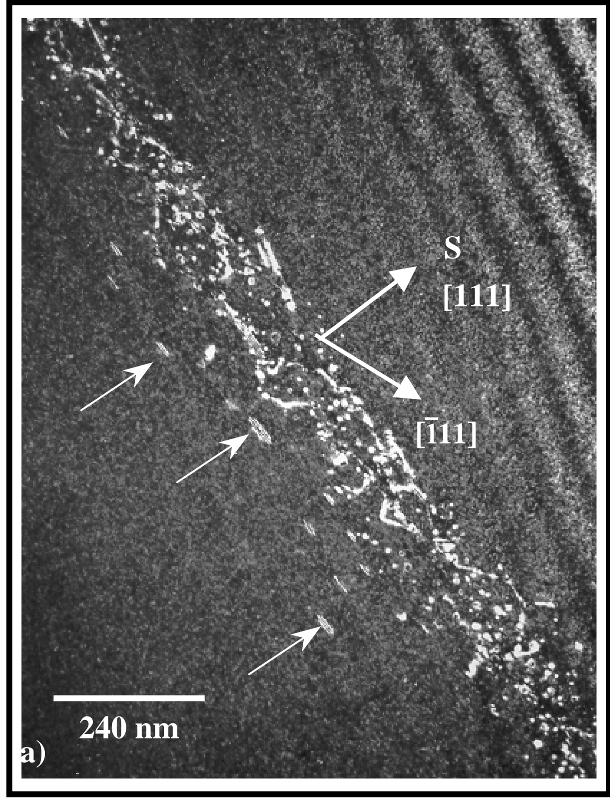

A detailed study of such faulted loops has been already described in a recent work [Beaufort *et al.* 2000] and is presented in §3.1.3. In this article, it is shown that bubbles and dislocation loops growth are closely linked. The formation of interstitial Frank loops may thus not result from the clustering of excess self-interstitial atoms created by the implantation as in the case of so-called End of Range (EOR) defects but from the growth of individual bubbles. This behaviour could be explained by a loop punching process. This process gives the bubble an extra plane of vacancies in exchange for an interstitial loop in the lattice. The initial stage may

be viewed as a small number of surface atoms being squeezed into interstitial positions between the two atomic planes closest to the equator of the bubble. More surface atoms being pushed between these two planes then complete this interstitial ledge. The resulting interstitial ring is then the first stage of the dislocation loop punching process [Adams *et al.* 1991]. It is known that in a fcc structure, Frank loops, i.e. dislocation loops with Burgers vector *a*/3<111>, are sessile [Hirth *et al.* 1968]. Thus, the Frank loop remains bound to the bubble, as seen in Fig.3.7b. Supposing that the process involved in the growth of these bubbles during annealing is loop punching, the pressure criterion for this process is given by:

$$p-2\gamma/r > \mu b/r \tag{3.1}$$

where p is the internal cavity pressure, γ is the surface tension or surface free energy of the material in which the bubble is formed (γ_{Si} = 1 $N.m^{-1}$), μ is the shear modulus of the material, b is the loop Burgers vector, and r is the cavity radius. Subtracting $2\gamma/r$ from the pressure corrects for the equilibrium pressure needed to match surface tension; the excess pressure must then exceed that required to punch loops, $\mu b/r$. The determination of the cavity volume allows for the estimation of the pressure after the process, when bubbles have been relaxed. The He density in bubbles has been estimated by assuming that all the He is still in bubbles; that leads to 1.32×10^{23} He/cm^3 . The internal cavity pressure is then 5 GPa using Mills, Liebenberg and Bronson (MLB) equation of state (EOS) of helium [Mills *et al.* 1980]. The required pressure for loop punching, calculated using r = 3 nm and μ = 68 GPa in Eq.(3.1), is 8 GPa. However, this value is the lowest limit since before loop punching the volume would have been less, perhaps one half this amount, and the density correspondingly higher. Thus, the internal cavity pressure before the process would be about 20 GPa which exceeds the required pressure for loop punching. Thus the hypothesis of loop punching appears reasonable.

c) Dislocation loops

The dislocation loops generated in rows from the buried layer and labelled A, B, C and D on Fig.3.8, have been studied by classical TEM methods [Edington *et al.* 1975]. The loop planes, their Burgers vectors and their nature (interstitial or vacancy) have been determined by studying the extinction, the changes in size, and the inside-outside contrast for different values of the diffraction vector **g**, respectively.

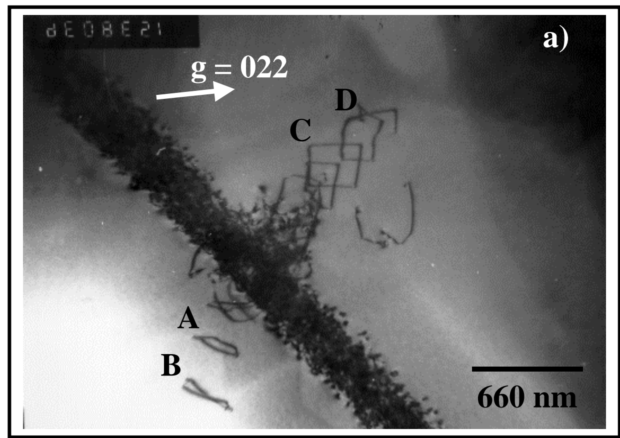

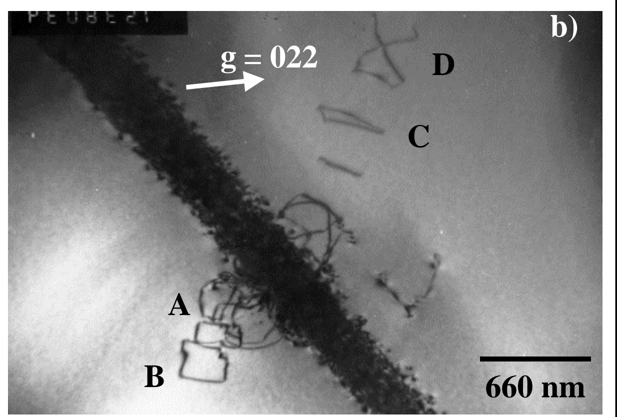

Figure 3.8: $[01\bar{1}]$ cross-section TEM pictures obtained in Si after helium implantation at 1.6 MeV with $2\mathrm{x}10^{16}$ cm^{-2} and anneal for 30 min at 800°C; **(a)** Edge on view of dislocation loops labelled A and B under **g** = 022 by tilting clockwise towards ($\bar{1}1\bar{1}$) plane. **(b)** Edge on view of the dislocation loops labelled C and D under **g** = 022 by tilting counter clockwise towards $(11\bar{1})$.

The plane of the foil, $(01\bar{1})$, was determined with regard to the general view and to the orientation of the surface. The direction of the Burgers vector of a loop can be determined using the **g**.**b** = 0 criterion for contrast extinction. Under **g** = $1\bar{1}\bar{1}$, loops A, B, C and D are invisible. Supposing that they are perfect dislocations (thus with Burgers vectors **b** = *a*/2<110>), and by analysis of the extinction under different **g**, leads to a Burgers vector **b** = *a*/2[101] for the loops C and D and **b** = *a*/2 [110] for A and B (see Fig.3.9.a,b). The habit plane of a loop is determined by looking at its changes in size. Under **g** = 022 and by tilting clockwise, towards the $(11\bar{1})$ plane, about the $[0\bar{1}\bar{1}]$ direction, A and B appear bigger whereas C and D appear smaller (Fig.3.8b). Under the same diffraction condition, but now by tilting counter clockwise, towards the $(\bar{1}1\bar{1})$ plane, about the same direction, C and D appear

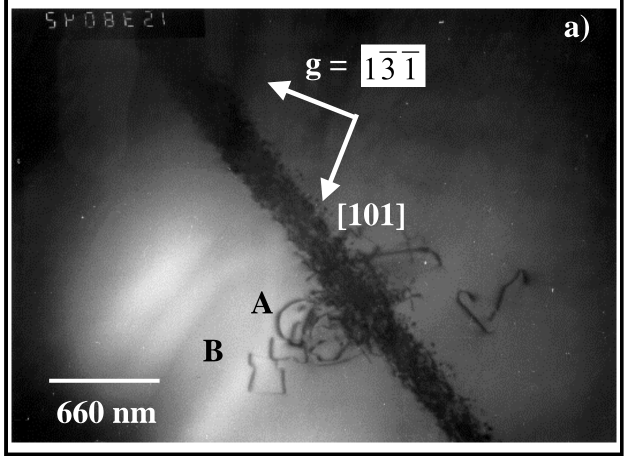

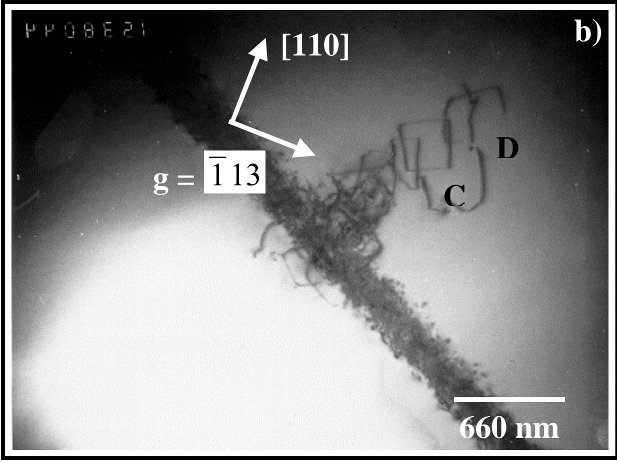

Figure 3.9: $[01\bar{1}]$ cross-section TEM pictures obtained in Si after helium implantation at 1.6 MeV with $2\mathrm{x}10^{16}$ cm^{-2} and anneal for 30 min at 800°C; **(a)** Extinction of the dislocation loops C and D under **g** = $1\bar{3}\bar{1}$. **(b)** Extinction of the loops A and B under **g** = $\bar{1}31$.

bigger while A and B can be seen edge on (Fig.3.8a). Thus, loops A and B lie in $(11\bar{1})$ plane whereas loops C and D lie in $(\bar{1}1\bar{1})$ plane. Afterwards, the method of inside/outside contrast [Edington *et al.* 1975] was used to determine the extrinsic/intrinsic nature of the loops. Because perfect edge loops may be either interstitial (extra plane) or vacancy (one plane missing) while there are two possible senses of inclination of the loops within the TEM foil, an edge dislocation may have four possible configurations (Fig.3.10).

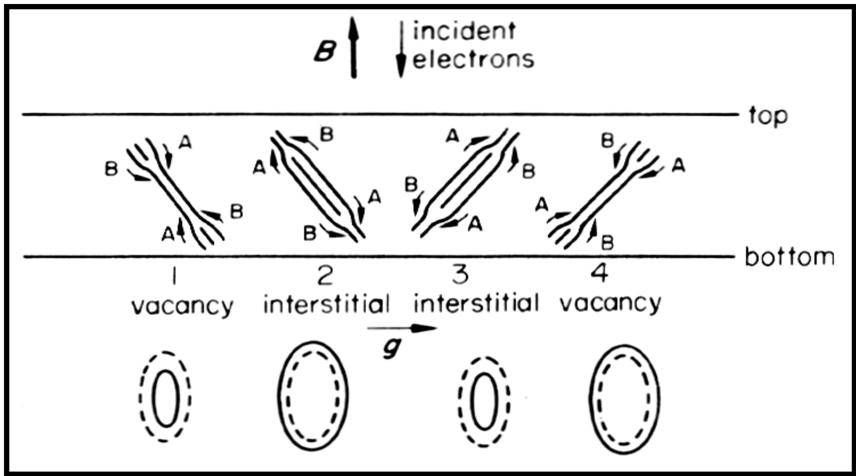

Figure 3.10: The four possible configurations of inclined vacancy or interstitial loops and the position of the image (heavy line) relative to the core (dashed line) [J.W. Edington, Practical Electron Microscopy].

The method depends upon whether or not the image of the loop is inside or outside the dislocation core. This is determined by the sense of rotation of the reflecting planes around the dislocation. If the reflecting plane is rotated towards $s = 0$ (s being the deviation from the Bragg reflection position), the image occurs at this position relative to the core.

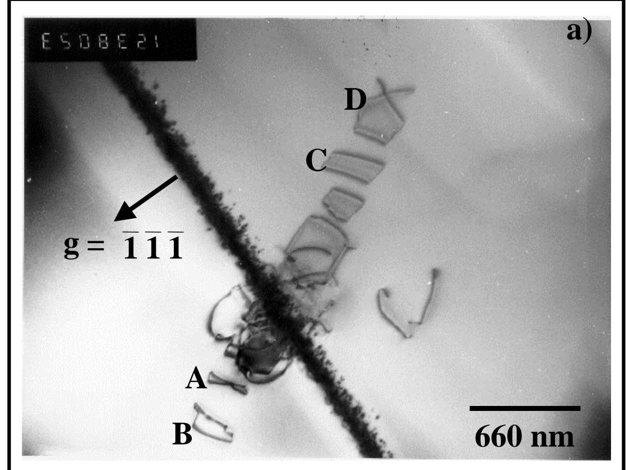

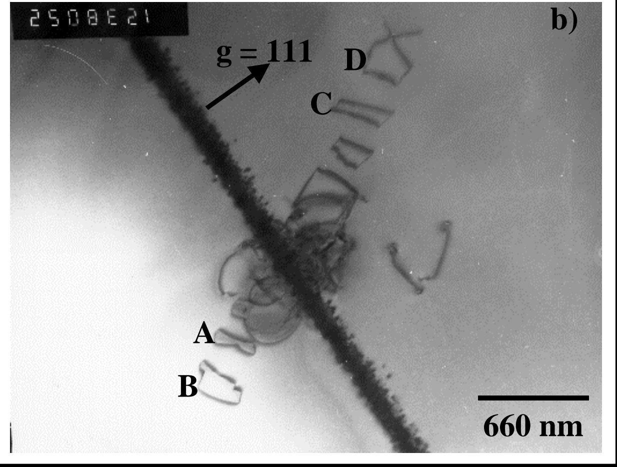

Figure 3.11: $[01\bar{1}]$ cross-section TEM micrographs obtained in Si after helium implantation at 1.6 MeV with $2x10^{16}$ cm^{-2} and anneal for 30 min at 800°C; **(a)** Inside contrast for the loops A and B, outside contrast for the loops C and D under **g** = $\bar{1}1\bar{1}$ **(b)** Outside contrast for the loops A and B, inside contrast for the loops C and D under **g** = 111.

Fig.3.11a shows that the loops A and B exhibit outside contrast while C and D exhibit inside contrast under **g** = $\bar{4}00$. This behaviour inverts on reversing the diffraction vector **g** (Fig.3.11b).

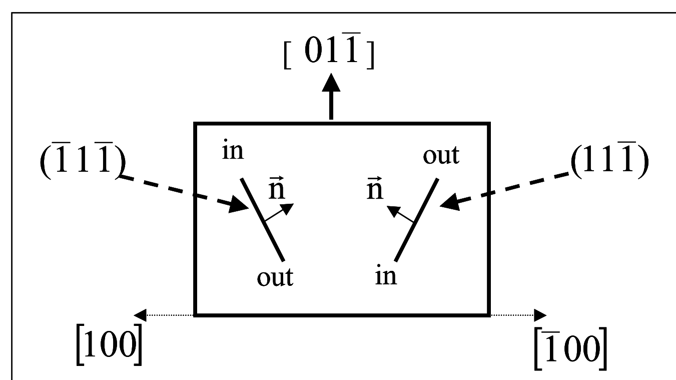

Figure 3.12: Orientations and inclinations of the loops inside the sample for **g** = 400 or $\bar{4}00$.

As described previously, loops A and B lie in the plane (11$\bar{1}$), while C and D lie in the plane ($\bar{1}1\bar{1}$) (see Fig.3.12). This shows that all the loops are interstitial in nature. The results are summarised in Table.3.1. Prismatic punching of dislocations loops has already been observed after oxygen precipitation in silicon [Tan *et al.* 1976]. In this case, the precipitates were also two dimensionally shaped on {100} planes, but the dislocation loops were lying in the {110} planes in contrast to our observations.

Loops	Habit plane	Burger vector **b**	Loop inclination and **g** vector	Inside/outside contrast	Loop nature
A	(11$\bar{1}$)	$\frac{1}{2}[110]$	**g** = $\bar{4}00$	Inside	Interstitial
B	(11$\bar{1}$)	$\frac{1}{2}[110]$	**g** = $\bar{4}00$	Inside	Interstitial
C	($\bar{1}1\bar{1}$)	$\frac{1}{2}[101]$	**g** = $\bar{4}00$	Outside	Interstitial
D	($\bar{1}1\bar{1}$)	$\frac{1}{2}[101]$	**g** = $\bar{4}00$	Outside	Interstitial

Table 3.1: Summary of the study of the dislocation loops.

These loops can be emitted by the bubble clusters or come from the coalescence of small dislocation loops resulting from the loop punching of bubbles inside the cluster. A graphic study of the loops states the answer. By determining the line of these loops under different diffraction vectors, the loops are found to be gliding in the {111} planes. It is well known that glissile dislocations involved in plastic deformation have Burgers vectors **b** of the *a*/2 <110> type and glide in {111} planes [George *et al.* 1997]. Thus, the plastic deformation of the matrix, due to the stress induced by the bubble clusters, generate these loops.

d) Bubble clusters

Fig.3.5 has shown that the clusters that intersected the band are oriented along [100] directions. By tilting experiments around the [100] direction towards the (001) plane, the cluster appears edge on (Fig.3.13). The clusters are thus two dimensionally shaped.

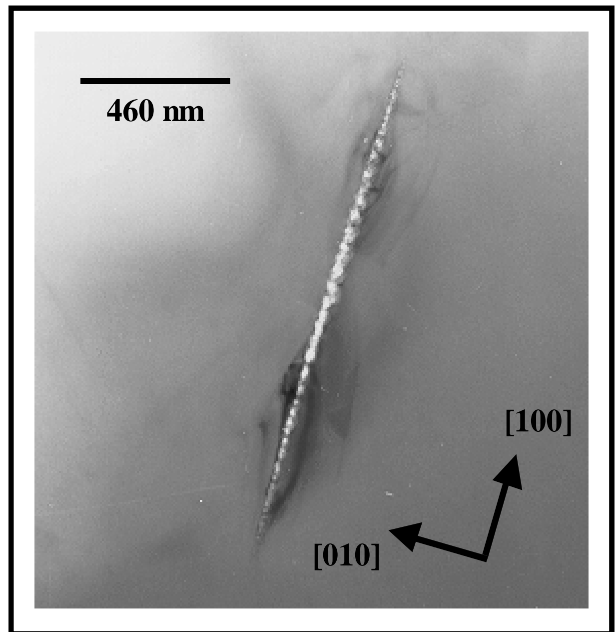

Figure 3.13: $[01\bar{1}]$ cross-section TEM image obtained in Si after helium implantation at 1.6 MeV with 2x10^{16} cm^{-2} and anneal for 30 min at 800°C, showing a cluster of bubbles edge on.

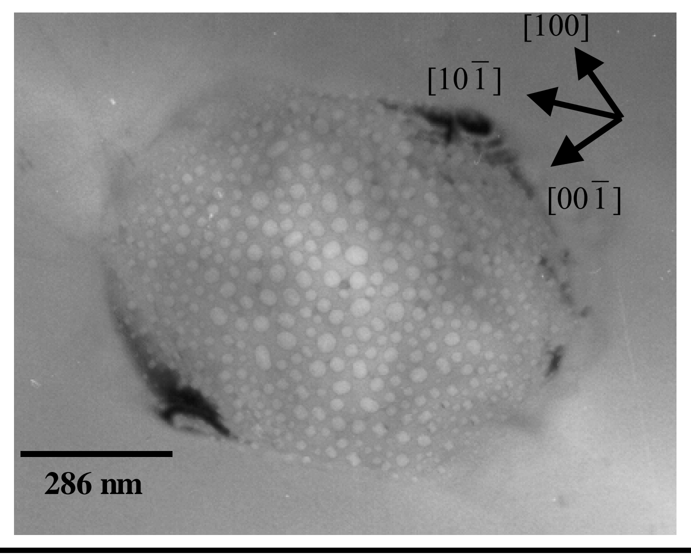

Figure 3.14: $[01\bar{1}]$ cross-section TEM picture obtained in Si after helium implantation at 1.6 MeV with 2x10^{16} cm^{-2} and anneal for 30 min at 800°C, showing a cluster in its habit plane. Note that the cluster is faceted.

By tilting experiments still around the [100] direction, but now towards the $(0\bar{1}0)$ plane, the cluster appears as a planar arrangement of spherical bubbles distributed within a faceted domain (Fig.3.14). Facets are oriented along <001> and <110> directions. The density of bubbles within the cluster is 2x10^{15} cm^{-3}. The mean bubble diameter is 30 nm, with the bubble diameters ranging from 10 nm to 50 nm : the bigger ones are located in the middle whereas the small ones are located in the periphery of the cluster. Actually, the bubble size distribution

follows a Gaussian distribution. The mean size of the cluster is 800 nm. Such planar clusters of spherical cavities in silicon have been already reported by Fichtner *et al.* [1999] in the case of a diluted system (dose of $1x10^{16}$ cm^{-2}), for a 40 keV helium implantation followed by annealing at 800°C for 30 s. They also report that for low doses, the two-dimensional structures show distinct morphological developments depending on the annealing temperatures. Indeed, for temperatures less than 800°C, they observe plate-like cavities, lying on {110} and {100} planes, with the shape being temperature dependent. For higher temperatures (T ≥ 800°C), they obtain spherical-like cavities arranged within planar clusters oriented along {100} planes, as in our case but for a smaller dose ($1x10^{16}$) and a smaller energy (40 keV).

Helium platelets and planar groups of small helium bubbles were first observed in molybdenum [Evans *et al.* 1981]. These platelets were lying on {110} planes. For annealing temperatures between 600 and 800 °C, they transformed into planar groups of helium bubbles still lying on {110} planes. Caspers *et al.* [1981] have performed atomistic calculations on molybdenum which suggested that the platelet-like growth of helium aggregates could be explained by a trap-mutation of a helium-vacancy defects (He-V) in which a helium atom is trapped and a self-interstitial atom is pushed out. Self-interstitials are known to cluster two-dimensionally, thus pushed out self-interstitials would do so and thereby favour the growth of helium aggregates in {110} planes.

For the fcc metal nickel, platelets or planar groups of small helium bubbles, lying on (111) planes, were also reported [D'Olieslaeger *et al.* 1986, Van Veen *et al.* 1984]. So, in metals, the planar clusters lie on the dense planes. The clusters in silicon could be expected to lie on the dense planes {111}, however, the present data and the literature show that in silicon they nucleate preferentially in {100} planes.

The first step of platelet formation is the generation of He_nV_m precipitates. When these precipitates have reached a critical size, they transform into complexes that offer more space for the helium, by pushing away the matrix atoms. This is the so-called trap-mutation process:

$$He_nV_m \rightarrow He_nV_{m+1} + I \qquad (3.2)$$

The self-interstitial that has been pushed away stays bound to the complex. These interstitials cluster together in the vicinity of the platelet, and form a dislocation loop. This loop is unable to glide through the crystal [Hirth *et al.* 1968]. When the pressure in the platelet decreases, the dislocation loop dissolves back into the helium cluster. This confirms

our assumption that the loops emerging from the clusters are generated by the induced stress in the matrix. The formation of platelets can be seen as a common initial structure from which arise the other arrangements of bubbles which are observed at higher temperatures [Fichtner *et al.* 1999]. In fact, during annealing (T≥800°C), the platelets change into planar arrangement of spherical bubbles. Finnis *et al*. [1982, 1983] found that the spherical bubble is always the preferred configuration and that under conditions of high internal pressure, a cluster of several bubbles has a lower total energy than one single large bubble.

3.1.1.3 Summary

The nucleation and growth of He induced cavities in silicon as well as the related defects were studied in the case of a $2x10^{16}$ He/cm^2 implantation at 1.6 MeV. After annealing, a buried layer was observed, in which planar clusters were randomly distributed. In this latter case, prismatic punching occurs and dislocations loops emerged. Within the bubble band, some of the bubbles are bound to Frank dislocation loops. We showed that these Frank loops were generated by loop punching. Planar clusters of helium bubbles lying on the {001} planes were also studied. It was determined that such He bubble structures nucleate and grow by the formation of He-filled platelet structures, almost certainly by the trap-mutation process, which transform into planar clusters of spherical bubbles upon thermal annealing. The rows of loops dislocations, which extended over a few micrometers away from the buried layer, were related to theses clusters. In fact, we showed that the clusters act as dislocation loop sources, due to the induced stress in the matrix.

References

[Adams *et al.* 1991] J.B. Adams, W.G. Wolfer, S.M. Foiles, C.M. Rohlfing, C.D. Van Siclen, in *Fundamental Aspects of Inert Gases in Solids*, edited by S.E. Donnelly and J.H. Evans (Plenum, New York), **279**, 3 (1991).

[Beaufort *et al.* 2000] M.F. Beaufort, E. Oliviero, H. Garem, S. Godey, E. Ntsoenzok, C. Blanchard, J.F. Barbot, *Phil. Mag. B* 80, 1975 (2000).

[Caspers *et al.* 1981] L.M. Caspers, M. Ypma, A. van Veen, G.J. Van des Kolk, *Phys. Status Solidi A* **63**, K183 (1981).

[D’Olieslaeger *et al.* 1986] M. D’Olieslaeger, L. De Schepper, G. Knuyt, L.M. Stals, *J. Nucl. Mater.* **138**, 27-30 (1986).

[Edington *et al.* 1975] J.W. Edington, *Practical Electron Microscopy in Materials Science*, Monograph three, Interpretation of Transmission Electron Micrographs (Macmillan, London, 1975).

[Evans *et al.* 1981] J.H. Evans, A. van Veen, L.M. Caspers, *Nature* **291**, 310 (1981).

[Fichtner *et al.* 1998] P.F.P. Fichtner, A. Mücklich, U. Kreissig, R.A. Yankov, W. Skorupa, *Nucl. Instr. Methods Phys. Res. B* **136-138**, 583-586 (1998).

[Fichtner *et al.* 1999] P.F.P. Fichtner, J.R. Kaschny, M. Behar, R.A. Yankov, A. Mücklich, W. Skorupa, *Nucl. Instr. Methods Phys. Res. B* **148**, 329-333 (1999).

[Finnis *et al.* 1982] M.W.Finnis, A. Van Veen and L.M. Caspers, *AERE Harwell TP Report 927* (1982).

[Finnis *et al.* 1983] M.W.Finnis, A. Van Veen and L.M. Caspers, *Rad. Effects* **78**, 121 (1983).

[Follstaedt *et al.* 1993] D.M. Follstaedt, S.M. Myers, H.J.Stein, *Mater. Res. Soc. Symp. Proc.* **279**, 105 (1993).

[George *et al.* 1997] A. George, Core structure and energies of dislocation in Si, in *Properties of Crystalline Silicon*, edited by Robert Hull (INSPEC, London), **20**, 108 (1997).

[Godey *et al.* 2000] S. Godey, T. Sauvage, E. Ntsoenzok, M.F Beaufort, J.F. Barbot, B. Leroy, *J. Appl. Phys.* **87**, 2158 (2000).

[Griffioen *et al.* 1987] C.C. Griffioen, J.H. Evans, P.C. De Jong, A. van Veen, *Nucl. Instr. Methods Phys. Res. B* **27**, 417 (1987).

[Hirth *et al.* 1968] J.P. Hirth, J. Lothe, in *Theory of Dislocations*, (John Wiley&Sons, New York, 1968).

[Mills *et al.* 1980] R.L. Mills, D.H. Liebenberg, J.H. Bronson, *Phys. Rev. B*, **21**, 5137 (1980).

[Tan *et al.* 1976] Y. Tan, W.K. Tice, *Phil. Mag.* **34**, 615 (1976).

[Ourmazd 1986] A. Ourmazd, *Mater. Res. Soc. Symp. Proc.* **59**, 331 (1986).

[Van Veen *et al.* 1984] A. van Veen, J.H. Evans, L.M. Caspers, J.Th. De Hosson, *J. Nucl. Mater.* **122-123**, 560 (1984).

[Williams *et al.* 1993] J.S. Williams, R.G. Elliman, M.C. Ridway, C. Jagadish, S.L. Ellingboe, R. Golberg, M. Petravic, W.C. Wong, Z. Dezhang, E. Nygren, B.G. Svensson, *Nucl. Instr. Methods Phys. Res. B* **80/81**, 507 (1993).

[Ziegler *et al.* 1985] J.F. Ziegler, J.P. Biersack, U. Littmark, *The Stopping and Range of Ions in Solids* (Pergamon Press, New York, 1985).

3.1.2 Influence of dose and dose-rate on bubble formation

Since radiation damage is one of the main components involved in bubble formation, it is important to understand not only the mechanisms of damage production, but also the factors that influence the accumulation of damage during irradiation. One aspect of damage production that has not received much attention is the influence of dose-rate. Nevertheless, high dose-rate implantation in silicon is becoming more prevalent in VLSI fabrication. New techniques, such as plasma immersion, involve very high dose-rate. This technique has been demonstrated to be economic for cavity formation [Chu *et al.* 1998]. Therefore a better understanding of the dose-rate effects during helium implantation in silicon is necessary.

In this section, we study the influence of the dose-rate on the formation of bubbles and on the associated extended defects in the case of medium dose MeV implantation of helium in n-type silicon. We report the TEM observations, showing new features of the micro-structural evolution of such cavity systems. A detailed study of the evolution of bubbles and their associated extended defects (dislocations) upon annealing is described. These results may provide a better comprehension of He bubble nucleation and growth phenomena as well as the formation of extended defects induced by the bubble growth process.

3.1.2.1 Experimental procedure:

All experiments were carried out on commercial n-n^+ silicon wafers. The n-type layer, 75 μm thick, was epitaxialy grown on a (111) oriented n^+ substrate of Czochralski silicon. The doping concentration of the n-region is N_D = 2x10^{14} cm^{-3} (doped with phosphorus). These samples were implanted at room temperature with 1.6 MeV helium provided by a 3.5 MV van de Graaff accelerator (CERI, Orléans) at three different fluxes: 2.5x10^{12}, 8.3x10^{12} and 1.3x10^{13} cm^{-2}.s^{-1}. The dose was kept constant at 2x10^{16} He.cm^{-2}. SRIM calculations [Ziegler *et al.* 1985] give R_p = 5.5 μm and ΔR_p = 0.2 μm, leading to a maximal local He concentration of 4x10^{20} cm^{-3} near to the minimum concentration required for the bubble formation in the case of keV energies after annealing [Follstaedt *et al.* 1996]. Anneals were performed under nitrogen gas flow at 800°C for 30 min in a quartz tube within a tubular furnace. Cross-sectional Transmission Electron Microscopy was used to study the implantation-damaged

region before and after annealing. The samples were cut, glued and then thinned using mechanical polishing and ion milling, for examination in the $[01\bar{1}]$ orientation. In the TEM images that were obtained from a JEOL 200 CX operating at 200 kV, *S* denotes the implanted surface of the sample.

3.1.2.2 Results

<u>As-implanted</u>

MeV helium implants in silicon, at $2x10^{16}$ cm^{-2}, lead also to bubble formation. TEM observations show a uniform and dense layer of small helium bubbles present in all the as-implanted samples. No visible differences in TEM micrographs were noticed between the as-implanted samples using different fluxes. As an example, the cross section image of the sample implanted at medium flux $8.3x10^{12}$ $cm^{-2}.s^{-1}$ is shown in Fig.3.15. The buried layer located at 5.5 μm below the surface is approximately 1 μm in width. It was difficult to obtain good bubble contrast because of the surrounding dark contrast due to the lattice damage. However, helium bubbles can be clearly seen as white spots with a dark edge in underfocus condition and as dark centers with a white edge in overfocus condition. The average diameter of the bubbles is estimated to be 2-3 nm - the same as that observed in case of keV implants. No extended defects are observed outside this buried layer.

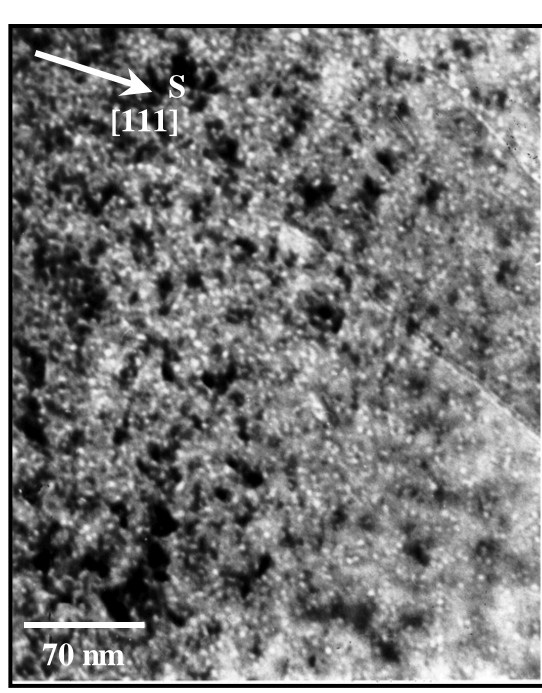

Figure 3.15: $[01\bar{1}]$ cross-section TEM micrograph of bubbles in silicon implanted with helium using a flux of $8.3x10^{12}$ $cm^{-2}.s^{-1}$ ($2x10^{16}$ cm^{-2}, 1.6 MeV, no anneal). Kinematical diffraction condition: underfocus.

After annealing

Upon annealing the small helium bubbles present in the as-implanted samples grow and agglomerate in a better-defined layer, as expected from previous work in the keV range [Raineri *et al.* 1995, 1996, 2000, Myers *et al.* 1999]. However, in contrast to keV implants, MeV implants result in the formation of secondary defects upon annealing. Depending on the flux different morphologies of the damage layer are observed.

a) 2.5x10^{12} cm^{-2}.s^{-1} flux

The general view of the damaged region (Fig.3.16), obtained at a low magnification in a cross-section image, shows that the 2.5x10^{12} cm^{-2}.s^{-1} flux Helium implantation followed by an anneal at 800°C for 30 min, gives rise to a continuous buried layer of about 0.7 μm wide and located at R_p= 5.5 μm. On closer inspection (Fig.3.17), bubbles are observed in the central region, 150 nm thick, of the buried layer. The vast majority of bubbles or cavities are faceted with facets parallel to the surface, i.e. (111) plane. As shown, the bubbles do not form a continuous band but are distributed within planar clusters of few tens of bubbles. These clusters are rather homogeneously distributed along the R_p. They are not located in planes perpendicular to the surface; their intersection with the plane of the foil is oriented along <100> direction. They are approximately 200 nm in size and the bubbles within have a mean diameter of 20 nm. Big platelets, consisting of a single plate-like bubble, are also observed with a size of about 100 nm (indicated by the black arrow on Fig.3.17). A tangle of many dislocations confined to the vicinity of the bubble band is also observed. A detailed study of these dislocations has shown that they are perfect dislocations: they lie in {111} planes with a Burger vector **b** = *a*/2<011>.

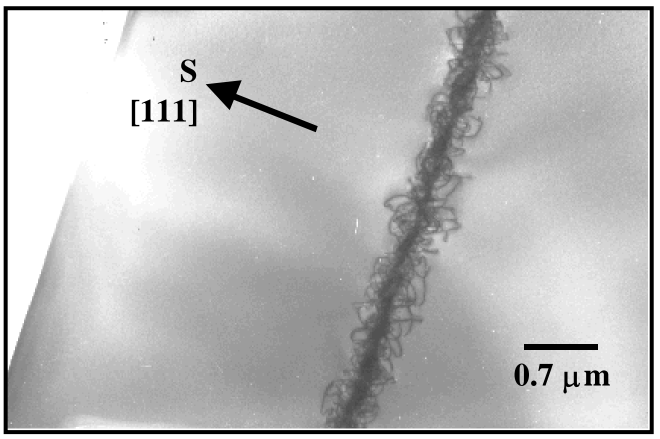

Figure 3.16: Cross-section TEM image showing the damaged region formed in Si after helium implantation with 2x10^{16} cm^{-2} at 1.6 MeV and annealing at 800°C for 30 minutes for the flux of 2.5x10^{12} cm^{-2}.s^{-1}.

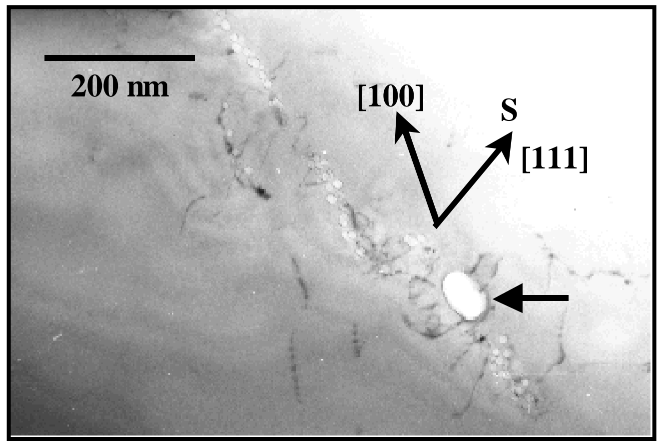

Figure 3.17: Cavity microstructure from cross-section TEM obtained in Si after helium implantation for the flux of $2.5x10^{12}$ $cm^{-2}.s^{-1}$ ($2x10^{16}$ cm^{-2}, 1.6 MeV and heat treatment for 30 min at 800°C). Kinematical diffraction condition: underfocus. Note that the intersection of the bubble clusters with the plane of the TEM foil is oriented along a specific direction [100], the absence of a continuous bubble layer and the presence of a single platelet indicated by an arrow.

b) $8.3x10^{12}$ $cm^{-2}.s^{-1}$ flux

The general view of the damaged region using the $8.3x10^{12}$ $cm^{-2}.s^{-1}$ flux (Fig.3.18) shows a continuous buried layer as well, but now surrounded by stacking of dislocation loops appearing in rows in an orderly manner. The loops seem to be emitted from specific points rather than homogeneously distributed within the layer. They can extend up to the implanted surface and to 6 μm into the bulk. From Fig.3.18, it is obvious that they are generated along specific directions. In any one row, the loops appeared to be equally spaced and of the same size. A detailed characterization of these loops is described in §3.1.1.

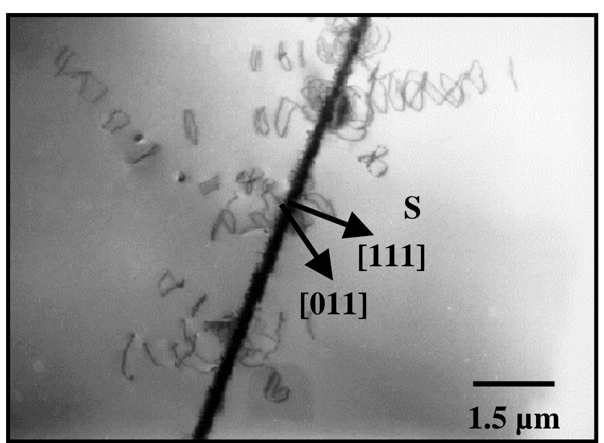

Figure 3.18: $[01\bar{1}]$ cross-section TEM image of the damage region formed in Si after helium implantation for the flux of $8.3x10^{12}$ $cm^{-2}.s^{-1}$ ($2x10^{16}$ cm^{-2}, 1.6 MeV and annealing at 800°C for 30 minutes).

Close inspection of the buried layer reveals a continuous band of small helium bubbles as well as small Frank dislocation loops. Clusters of bigger bubbles intersect this band

(Fig.3.19). The rows of dislocation loops, previously observed, emerge from them. Moreover**,** the loops have the same size and shape as the related cluster. Thus, we can reasonably assume that these clusters act as loop sources. The bubble band has an average width of 240 nm and is located about 5.6 μm deep from the surface (R_p = 5.5 μm using SRIM simulation). The bubbles within are spherical in shape and homogeneously distributed. The density is estimated to be about $2x10^{16}$ cm^{-3}. The bubble diameters range from 7 nm to 22 nm, with a mean diameter of 12 nm. The intersection between the clusters that crossed the bubble band and the plane of the foil is oriented along <100> direction.

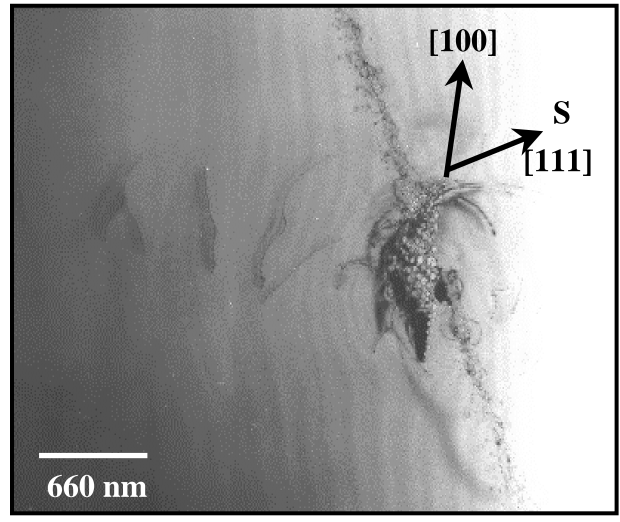

Figure 3.19: Close view of a cluster within the bubble band observed for the flux of $8.3x10^{12}$ $cm^{-2}.s^{-1}$ ($2x10^{16}$ cm^{-2}, 1.6 MeV, 30 min. at 800°C).

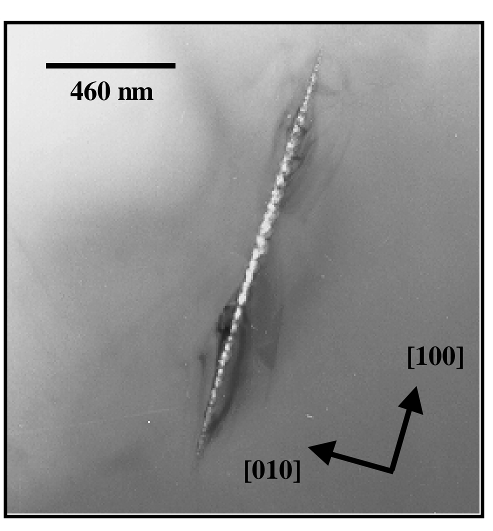

Figure 3.20: Cluster of bubbles edge on ($8.3x10^{12}$ $cm^{-2}.s^{-1}$)

By tilting around the [100] direction towards the (001) plane, the cluster appears edge on (Fig.3.20). They are thus two dimensionally shaped. By tilting again around the [100] direction, but now towards the $(0\bar{1}0)$ plane, they appear as a planar arrangement of spherical bubbles distributed within a faceted domain (Fig.3.21). The facets are oriented along <001> and <110> directions. The density of bubbles within the cluster is $2x10^{15}$ cm^{-3}. The mean bubble diameter is 30 nm, with the bubble diameters ranging from 10 nm to 50 nm: the bigger bubbles are located in the middle whereas the small ones are located in the periphery of the cluster. The bubble size distribution follows a Gaussian distribution. The mean size of the clusters is 800 nm.

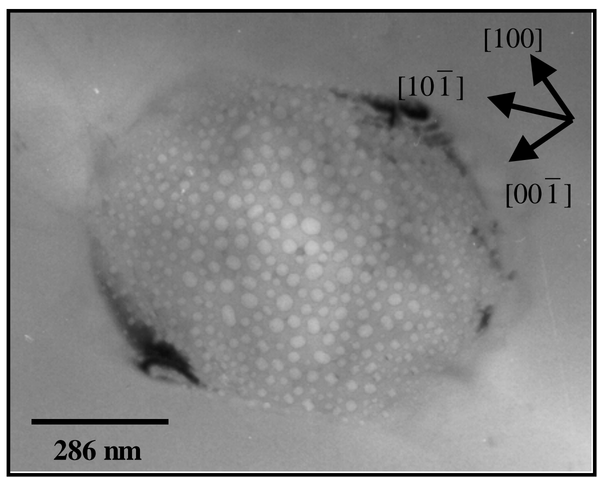

Figure 3.21: Cluster in its habit plane ($8.3x10^{12}$ $cm^{-2}.s^{-1}$).
Note that the cluster is faceted.

c) $1.3x10^{13}$ $cm^{-2}.s^{-1}$ flux

At higher flux, Fig.3.22, a continuous buried layer located near R_p as well as many rows of dislocations are observed. Stacked dislocation loops at a density larger than that observed at lower flux, are found also to extend towards the surface or towards the bulk in specific directions.

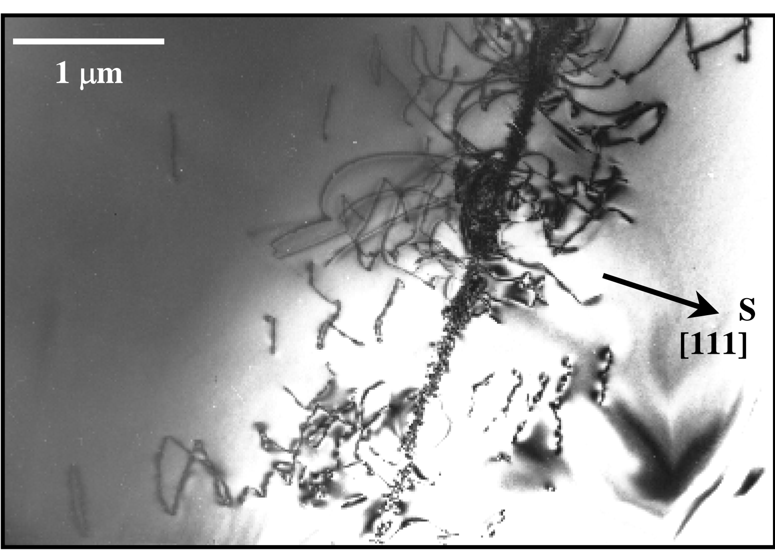

Figure 3.22: [01 $\bar{1}$] cross-section TEM image showing the damage region formed in Si after helium implantation for the flux of $1.3x10^{13}$ $cm^{-2}.s^{-1}$ ($2x10^{16}$ cm^{-2}, 1.6 MeV, 30 min. at 800°C).

Closer inspection of this layer (Fig.3.23) reveals that it is made up of a continuous bubble band with the clustering of bigger bubbles, partially or totally, included inside this band. As mentioned above, the clusters act as dislocation sources. Frank loops bound to bubbles are also observed inside and alongside the band. The bubble band is about 300 nm wide and the mean bubble diameter is 12 nm. The density of bubbles outside the clusters is estimated to be

about 2x10^{16} cm^{-3}. The clusters are about 450 nm long and the bubbles within have a mean diameter of 30 nm. The major difference with the other fluxes without taking into account the cluster density is the orientation of the clusters. Indeed, the intersection of clusters with the plane of the TEM foil is oriented along [100] or [$\bar{1}$11] directions (Fig.3.22). Thus the cluster habit planes are now the {100} or the {110} planes.

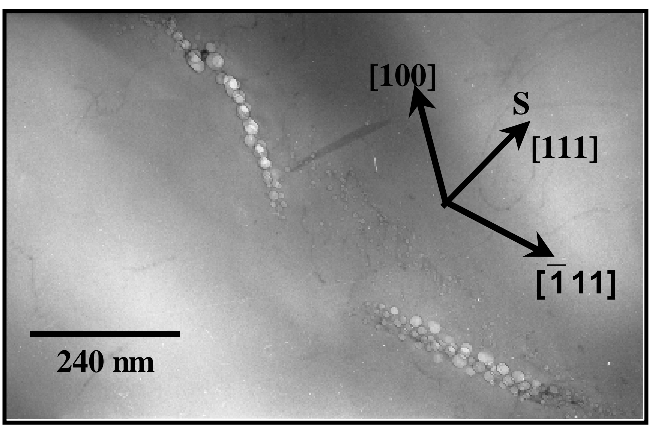

Figure 3.23: Close view of bubble clusters nearly include into the continuous bubble layer (1.3x10^{13} cm^{-2}.s^{-1}). Kinematical diffraction condition : underfocus. Note that the intersections of the clusters with the plane of the TEM foil are oriented along the two specific directions [100] and [$\bar{1}$11].

3.1.2.4 Discussion

Planar clusters of spherical cavities in silicon have been already reported for dilute systems; i.e. at medium doses (1x10^{16} and 5x10^{15} cm^{-2}) in the keV range [Fichtner *et al.* 1997, 1998, 1999]. In the MeV range, when decreasing the dose to 1x10^{16} cm^{-2} (see Fig.3.24) we observed a damaged layer which is made up of small defects, probably dislocation loops. Only in some of them are one or more bubbles clearly observed (inset of Fig.3.24). Thus, as previously observed for medium dose in the keV range, an alternative route for the development of bubble microstructure seems also to operate in the MeV range, and bubbles tend to cluster.

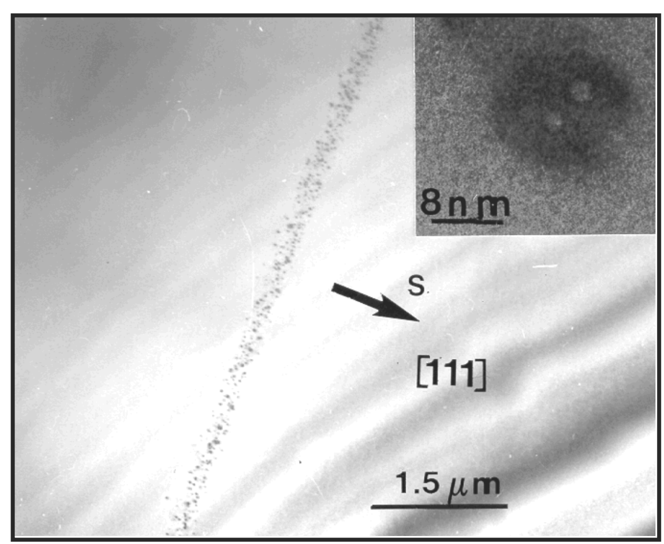

Figure 3.24: [01$\bar{1}$] cross-section TEM image of the damage region formed in Si after helium implantation at a dose of 1x10^{16} cm^{-2} (1.3x10^{13} cm^{-2}.s^{-1}, 1.6 MeV, 30min. at 800°C).

At high doses, $5x10^{16}$ and $1x10^{17}$ cm^{-2}, a homogenous dense array of bubbles or cavities is observed Fig.3.25-26, as expected from conventional coarsening mechanism. Below the bubble band, defects that consist of an agglomeration of excess Si interstitials stored in a (meta) stable configuration are observed. They will be studied in detail in the next section (§.3.1.3).

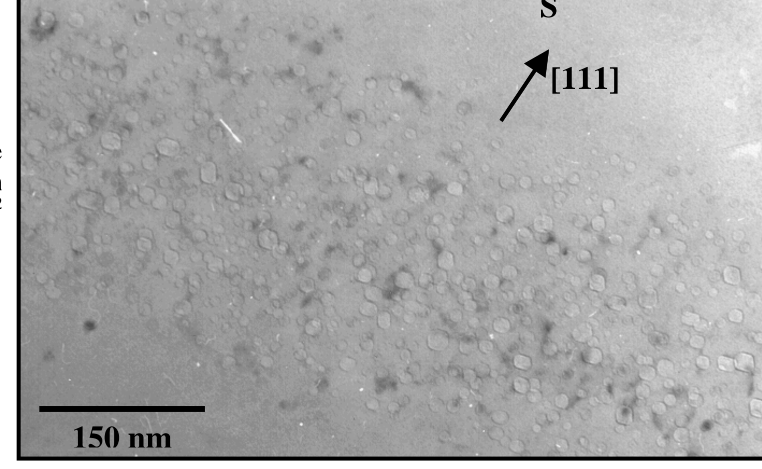

Figure 3.25: $[01\bar{1}]$ cross-section TEM image of the damage region formed in Si after helium implantation at a dose of $5x10^{16}$ cm^{-2} ($1.3x10^{13}$ $cm^{-2}.s^{-1}$, 1.6 MeV, 30min. at 800°C).

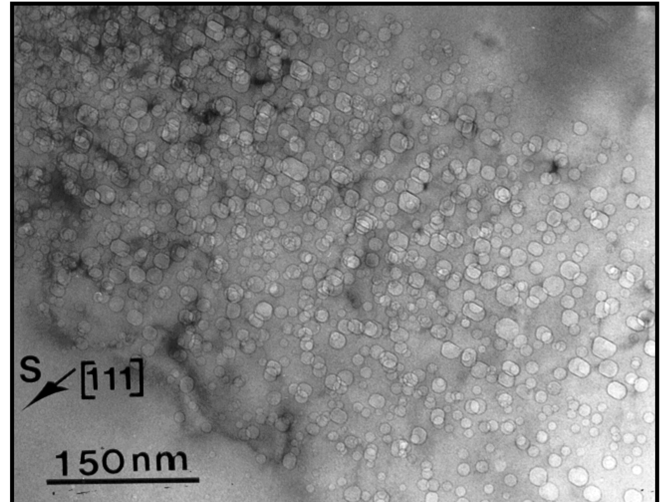

Figure 3.26: $[01\bar{1}]$ cross-section TEM image of the damage region formed in Si after helium implantation at a dose of $1x10^{17}$ cm^{-2} ($1.3x10^{13}$ $cm^{-2}.s^{-1}$, 1.6 MeV, 30min. at 800°C).

As discussed in the previous section (§3.1.1), helium platelets and planar groups of small helium bubbles were first observed in metals [Evans *et al.* 1981, D'Olieslaeger *et al.* 1986, Van Veen *et al.* 1984] and lay in the dense planes. In case of Si, the present observations and the data from literature [Fichtner *et al.* 1999] show, however, that they nucleate preferentially in {100} or {110} planes. As explained earlier, the platelet-like growth of helium aggregates could be explained by a trap-mutation [Van Veen *et al.* 1984] of a helium-vacancy defect (He-V). In the case of medium doses, the formation of platelets can be seen as a common initial structure from which issue the other arrangements of bubbles observed at higher temperatures [Fichtner *et al.* 1997]. Upon annealing (T≥800°C), the platelets change into

planar arrangement of spherical bubbles as shown by Finnis *et al.* [1982, 1983]. Thus, upon annealing platelets are first created and are then transformed into planar clusters of bubbles. However, the platelet still observed after complete annealing in the lowest flux sample (indicated by the black arrow on Fig.3.17) must be more stable.

Helium bubble formation is a complex phenomenon that occurs following different independent steps and that involves a few different processes or mechanisms such as loop punching, migration and coalescence, Ostwald ripening, trap-mutation…etc. It is well known that the main components involved in bubble formation are the radiation damage and the diffusion of the implanted helium atoms. During implantation, multi-vacancies are created trapping helium atoms to evolve in bigger He_nV_m clusters up to visible gas bubbles. The limit for bubble formation is not only due to the helium concentration but also to the vacancy concentration. This has been proved by second implantation experiments [Raineri *et al.* 2000]. Thus a higher concentration of bubbles can be obtained for an implanted dose ($\geq 1x10^{16}$) if more vacancies are generated. This means that the dose-rate is a crucial parameter for the bubble formation, as observed in this work. Even if some controversies exist about diffusion coefficients of vacancies and self-interstitials in silicon, these defects are known to be highly mobile at room temperature, leading to strong annihilation within a single collision cascade. Only a few percent of the Frenkel pairs survive. The dose rate has been shown to strongly influence the defect build-up in semiconductors. For high doses and dose rates the collision cascades overlap before the dynamical annealing of defects in single cascades and a higher concentration of stable defects will result. At low doses ($<10^{12}$ cm^{-2}) and dose rates a reverse effect has been found, due to the enhanced diffusion time of vacancies [Svensson *et al.* 1993, 1997]. It is thus reasonable to assume that more He_nV_m clusters will be created with increasing dose rate for a fixed dose of $2x10^{16}$ cm^{-2}. More bubbles will thus be formed during an appropriate anneal, leading also to a wider bubble layer. However, the generation of vacancies resulting from the nuclear collisions should reach a saturation value with the increasing flux since even using high doses of He implantation silicon can not be amorphized at room temperature. In the case of high dose implantation, the stress induced by the large concentration of He in interstitial positions could also create vacancies that will participate in the creation of a homogeneous bubble band observed after annealing.

In the as-implanted samples, no differences were noticed in TEM micrographs. However, the concentration of small He_nV_m clusters, consisting of only few atoms and thus not detectable by TEM, must be different. It was even not possible to obtain a rough estimation of the

bubble density in the buried layer, but it can be assumed that the density is different within each sample. For the lowest flux, He and vacancies cluster together to form He_nV_m complexes large enough to be detected by TEM in the as-implanted sample. However, since the concentration of vacancies C_V is small, one can assume that these clusters are in an over-pressurized state, that means with n >> m. Thus the He_nV_m complexes are involved in trap-mutation leading to the formation of platelets and then to planar arrangements of spherical bubbles. Increasing the flux, more vacancies are available. More He_nV_m clusters are thus created but not in an over-pressurized state. They can easily evolve into bubbles by trapping the surrounding vacancies and He atoms leading to a continuous bubble band. This bubble band enlarges when increasing again the flux. By providing more vacancies, the concentration of bubbles increases. In the middle dose-rate sample, there is, however, still a lack of vacancies and some over-pressurized He_nV_m clusters still co-exist. This could explain the observed planar arrangements of spherical bubbles, Fig.3.19. At the highest flux, the clusters are now lying in two different families of planes and are located within the bubble band. We can assume that increasing again the flux will lead to the formation of a continuous and homogenous bubble band without clusters as observed for higher doses, Fig.3.25-26.
The appearance of rows of dislocations seems to be related to the size of the clusters of spherical bubbles since only tangle of dislocations located inside the damage band are observed at low flux. However, more experiments as well as calculations are needed to determine the limiting size of these clusters for the generation of stacking dislocations. The Frank loops observed within the bubble band and bound to bubbles would appear to result from loop punching.

3.1.2.5 Summary

The influence of the dose-rate on the nucleation and the growth of He induced cavities in silicon, as well as of the related defects, has been studied in the case of a $2x10^{16}$ He/cm^2 implantation at 1.6 MeV. In all the as-implanted samples, a layer of small helium bubbles is observed. On the TEM micrographs no visible differences are noticed for the different fluxes. After annealing, completely different features of the micro-structural evolution of the cavity systems are observed for each flux. For the lowest flux, platelets and planar clusters of helium bubbles are distributed along the projected range R_p and are surrounded by a tangle of dislocations. No continuous bubble band is observed. For the medium and the highest flux, a continuous bubble band is observed, intersected by rather homogeneously distributed planar

clusters of helium bubbles. From these clusters prismatic punching occurs and gliding dislocation loops emerge. They are found to extend over few micrometers away from the buried layer. Within the bubble band, some of the bubbles bound to Frank dislocation loops show that loop punching is involved in the bubble growth. The width of the bubble band, the cluster size, habit planes as well as their concentration are shown to be dose-rate dependent. These behaviors are discussed in terms of vacancy concentration, over-pressured He_nV_m clusters and the trap-mutation process.

Flux ($cm^{-2}.s^{-1}$)	**Clusters**		**Continuous bubble band**		**Clusters included in the bubble band ?**	**Stacking of dislocation loops ?**	**Frank loops ?**
	Size (nm)	Habit plane	?	Width (nm)			
2.5×10^{12}	200	<100>	✗	-	✗	✗	✗
8.3×10^{12}	800	<100>	✓	240	✗	✗	✓
1.3×10^{13}	450	<100> and <110>	✓	300	✓	✓	✓

Table.3.2 : Summary of the dose-rate influence on bubble formation in silicon for helium implantation (2×10^{16} cm^{-2}, 1.6 MeV, 30 min. at 800°C)

References

[Chu *et al.* 1998] P.K. Chu, N.W. Cheung, *Mat. Chemistry and Physics* **57**, 1 (1998).

[D'Olieslaeger *et al.* 1986] M. D'Olieslaeger, L. De Schepper, G. Knuyt, L.M. Stals, *J. Nucl. Mater.* **138**, 27-30 (1986).

[Evans *et al.* 1981] J.H. Evans, A. van Veen, L.M. Caspers, *Nature* **291**, 310 (1981).

[Fichtner *et al.* 1997] P.F.P. Fichtner, J.R. Kaschny, R.A. Yankov, A. Mücklich, U. Kreiβig, W. Skorupa, *Appl. Phys. Lett.* **70**, 732 (1997).

[Fichtner *et al.* 1998] P.F.P. Fichtner, A. Mücklich, U. Kreissig, R.A. Yankov, W. Skorupa, *Nucl. Instr. Methods Phys. Res. B* **136-138**, 583-586 (1998).

[Fichtner *et al.* 1999] P.F.P. Fichtner, J.R. Kaschny, M. Behar, R.A. Yankov, A. Mücklich, W. Skorupa, *Nucl. Instr. Methods Phys. Res. B* **148**, 329-333 (1999).

[Finnis *et al.* 1982] M.W.Finnis, A. Van Veen and L.M. Caspers, *AERE Harwell TP Report 927* (1982).

[Finnis *et al.* 1983] M.W.Finnis, A. Van Veen and L.M. Caspers, *Rad. Effects* **78**, 121 (1983).

[Follstaedt *et al.* 1996] D.M. Follstaedt, S.M. Myers, G.A. Petersen, J.W. Medernach, *J. Electron. Mater.* **25**, 157 (1996).

[Myers *et al.* 1999] S.M. Myers, D.M. Follstaedt, *J. Appl. Phys.* **86**, 3048 (1999).

[Raineri *et al.* 1995] V. Raineri, P.G. Fallica, G. Percolla, A. Battaglia, M. Barbagallo, S.U. Campisano, *J. Appl. Phys.* **78**, 3727 (1995).

[Raineri *et al.* 1996] V. Raineri, S.U. Campisano, *Appl. Phys. Lett.* **69**, 1784 (1996).

[Raineri *et al.* 1996] V. Raineri, P.G. Fallica, S. Libertino, *J. Appl. Phys.* **79**, 9012 (1996).

[Raineri *et al.* 2000] V. Raineri, M. Saggio, E. Rimini, *J. Mater. Res.* **15**, 1449 (2000).

[Raineri *et al.* 2000] V. Raineri, S. Coffa, E. Szilagyi, J. Gyulai, E. Rimini, *Phys. Rev. B* **61**, 937 (2000).

[Svensson *et al.* 1993] B.G. Svensson, C. Jagadish, J.S. Williams, *Phys. Rev. B* **71**, 1860 (1993).

[Svensson *et al.* 1997] B.G. Svensson, C. Jagadish, A. Hallen, J. Lalita, *Phys. Rev. B* **55**, 10498 (1997).

[Van Veen *et al.* 1984] A. van Veen, J.H. Evans, L.M. Caspers, J.Th. De Hosson, *J. Nucl. Mater.* **122-123**, 560 (1984).

[Ziegler *et al.* 1985] J.F. Ziegler, J.P. Biersack, U. Littmark, *The Stopping and Range of Ions in Solids* (Pergamon Press, New York, 1985).

3.1.3 Influence of annealing time on bubble and defect formations

In this section we explore the possibility of creating cavities by high dose MeV helium ion implantation in n-type silicon. The evolution of the buried layer (bubbles, dislocations, …) created by the helium implantation has been studied as a function of annealing time while implantation energy, dose, dose rate, and annealing temperature were kept constant.

3.1.3.1 Experimental procedure:

All the experiments were performed on commercial n-n^+ silicon wafers. The n-type layer, 7.5 μm thick, was epitaxially grown on a <111> oriented n^+-substrate of Czochralski silicon. The doping concentration N_D of the 100 μm thick n-region, was about $1\text{x}10^{14}$ cm^{-3} (doped with phosphorus). These samples were implanted at room temperature at a dose of $1\text{x}10^{17}$ $ions.cm^{-2}$ with 1.6 MeV helium ions ($R_p \approx 5.5$ μm and $\Delta R_p \approx 0.2$ μm : TRIM calculations [Ziegler *et al.* 1985]) using a 3.5 MV van de Graaff accelerator (CERI, Orléans). The helium implantation rate, kept constant for all the irradiations, was $1.2\text{x}10^{13}$ cm^{-2} s^{-1}. Anneals were performed under nitrogen gas flow at 800 °C for 15 min, 30 min, 500 min and 17 h.

The structure and evolution of the implantation damage during the anneals were studied with cross-sectional transmission electron microscopy (TEM). The samples were thinned using ion milling and TEM images were obtained with a JEOL 200 CX operating at 200 kV. For studying cavities or bubbles with minimal contrast from the unavoidable accompanying lattice damage, specimens were tilted from their <110> orientation by few degrees in order to reduce diffraction effects. They were also imaged in under-focus and over-focus conditions to highlight the cavity edges with Fresnel contrast. In all the TEM pictures the as-implanted surface is indicated by an arrow and the letter *S*.

3.1.3.2 Results and discussion

<u>As-implanted sample</u>

A low magnification cross-section TEM image shows that the He^+ implantation at $1\text{x}10^{17}$ cm^{-2} produces a continuous damage layer. The average width of the damage band is estimated

to be 700 nm. A closer view, as seen in Fig.3.27, shows that the damage layer contains a very high density of small helium bubbles. It is difficult to observe them because of the lattice damage that prohibits good bubble contrast. Their average diameter is estimated to be about 3 nm. Using weak beam conditions, we observe in this layer a granular contrast that is probably induced by small clusters of point defects or by linear defects generated by the helium implantation. Similar results have been previously reported after low energy helium implantation [Griffioen *et al.* 1987], [Siegele *et al.* 1995]. In a previous work, no bubbles have been observed in hydrogen-implanted silicon [Beaufort *et al.* 1994].

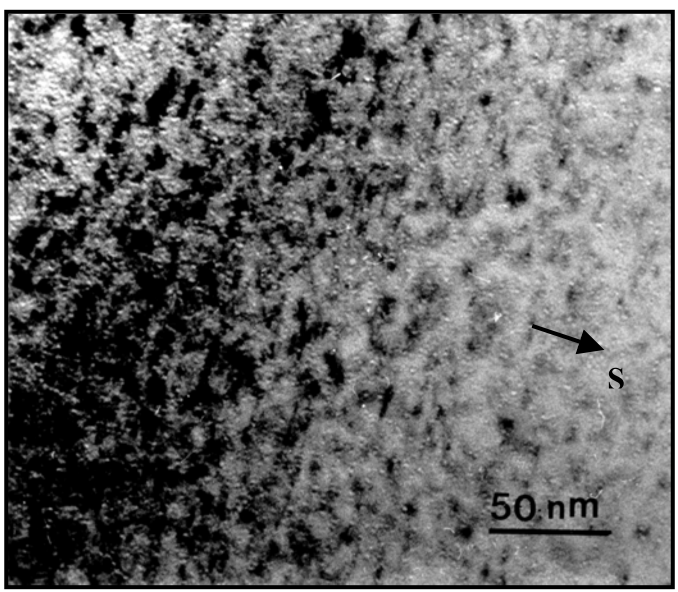

Figure 3.27: Cross-section TEM micrograph of bubbles in silicon implanted with helium at $1x10^{17}$ cm^{-2}, 1.6 MeV, no anneal. Kinematical diffraction condition: underfocus.

After annealing at 800°C

a) 15 minutes annealing.

After a 15 min. anneal at 800 °C, the TEM micrograph, Fig.3.28a, reveals two different layers: a continuous bubble layer of about 700 nm width followed by a layer of low defect density (~ 600 nm). The majority of bubbles have a circular shape with size ranging from 5 to 25 nm. Some of the bubbles of large diameter are faceted with facet planes of {111} type. A few elongated cavities are also observed. The bubble density in the middle of the band is estimated to be $2.5x10^{16}$ cm^{-3}. Lattice defects (dislocations) from the implantation are also

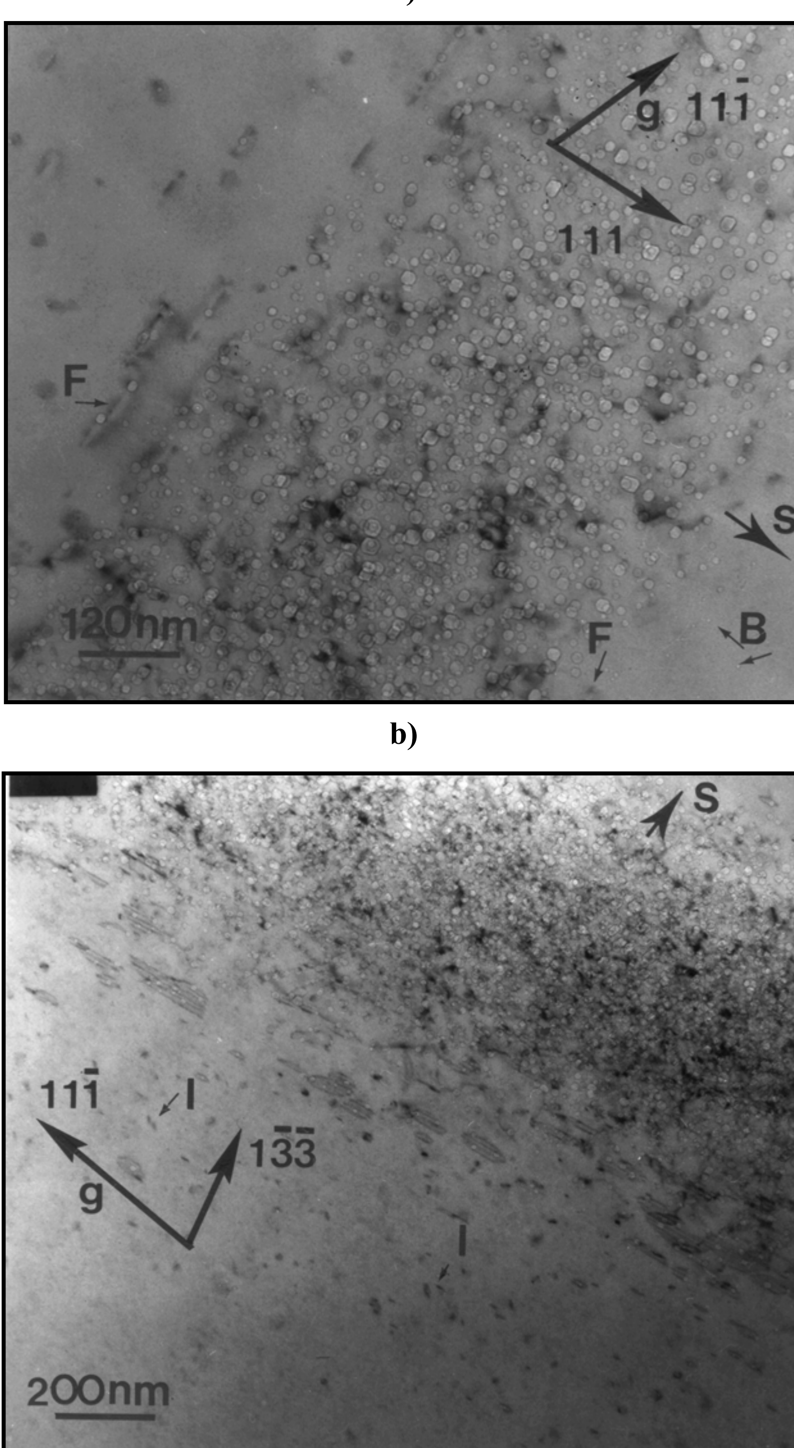

Figure 3.28: Cross-section TEM pictures obtained in Si after helium implantation with 1×10^{17} cm^{-2} at 1.6 MeV and heat treatment for 15 min at 800 °C. **(a)** Damage visualization: F : Frank loop, I :{113} defects ?, B : small bubbles. **(b)** Observation of the faulted loops by tilting the sample toward the $(\bar{3}\,1\,\bar{2})$ plane; as seen all the Frank loops are associated with bubbles, even in front of the bubble band.

present inside this layer but their characterization was not possible in bright field even in weak beam conditions. Up to 600 nm below this band, a very low density of bubbles is observed, all of them being actually bound with lattice damage. A more detailed study has

shown that these defects are dislocation loops since they exhibit a two lobes contrast particularly visible in dynamical conditions when they are edge-on imaged. The usual +g and -g method has shown that they are interstitial type (extrinsic) dislocation loops in nature. Using weak beam conditions with **g** =$11\bar{1}$, one family whose habit plane is parallel to the surface, (111), can be set edge on, Fig.3.28a. By means of tilting experiments toward the defect plane, ($\bar{3}1\bar{2}$) in Fig.3.28b, the faulted contrast is observed. According to the **g.R**=0 criterion, the displacement vector is found to be 1/3[111] as characteristic of Frank loops. This has been also confirmed by studying the border dislocations which are out of contrast with **g** = $\bar{1}\bar{1}1$ and in contrast with **g** = 022. When possible, an estimation of the number of interstitials stored in one loop has been made. We found that the number of interstitials roughly corresponds to the number of atoms released from the formation of the bound bubble. So, it appears obvious that the interstitial dislocation loops have grown when bubbles have coarsened during annealing, as already discussed in ion-implanted metals [Donnelly *et al.* 1991]. The formation of interstitial Frank loops may thus not result from the clustering of excess self- interstitial atoms created by the implantation as in the case of the so-called End Of Range (EOR) defects but from the growth of individual bubbles [Bonafos *et al*. 1997]. This is confirmed by the observation of some Frank dislocations bound with bubbles in the upper border of the buried layer (labelled F in Fig.3.28a) where no excess of Si interstitials is expected. Larger faulted loops bound to many bubbles are observed near the bubble band at a depth corresponding to the helium depth distribution. Unfortunately, no loop size distribution can be done preventing any calculations of interstitials stored in all the loops. It seems, however, that this mechanism may not operate for the high bubble concentrations since no faulted loops have been observed in the high buried layer. Frank loops surrounding a {111} planar array of bubbles and cavities have already been reported in high energy H implanted silicon after a 600 °C anneal [Beaufort *et al.* 1994]. The cross-section image, Fig.3.28b, also reveals the presence of some very small defects elongated in shape that could be the well-known "rodlike" or {113} defects, labelled I. The morphology of the {113} defects will be discussed in the next section, i.e. after the 30 min anneal, where they are large enough to be studied. Moreover, having a closer look in front of the large band of bubbles, we can observe numerous very small bubbles, of about 2-3 nm in diameter (labelled B in Fig.3.28a). These small bubbles do not seem to have coarsened during the annealing. At low implantation energy, it has been also reported that the bubble distribution extends toward the front surface, before and after annealing [Follstaedt *et al.* 1996, Raineri *et al.* 1995].

b) 30 minutes annealing

Fig.3.29a and b show the 1x10^{17} He.cm^{-2} sample after annealing at 800 °C for 30 min. Besides the reduction of the bubble layer which is about 500 nm wide, the most obvious changes compared to the 15 min anneal are related to the defects observed below it. Indeed, two types of defects are now clearly observed below the band of bubbles. The Frank dislocation loops are now among elongated extended defects whose sizes are up to 500 nm and that extend up to 700 nm on this side, see Fig.3.29a. A more detailed study of these long defects showed that they appeared narrow and faulted in the (110) and $(1\bar{2}\bar{1})$ planes.

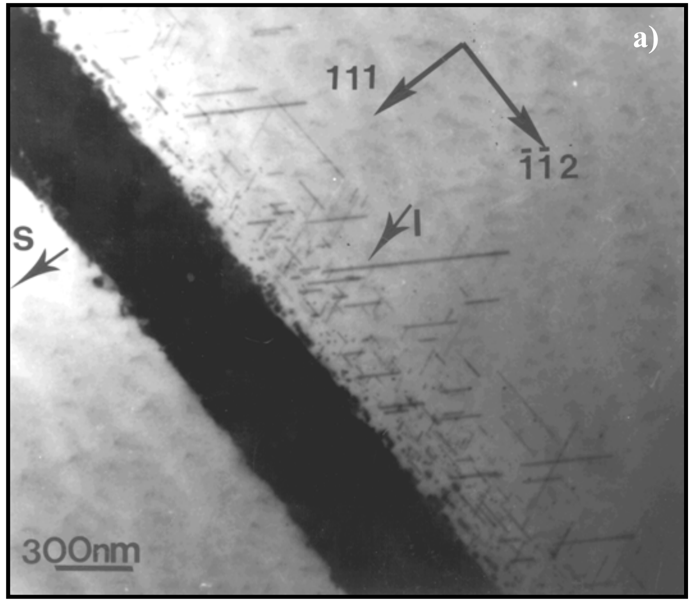

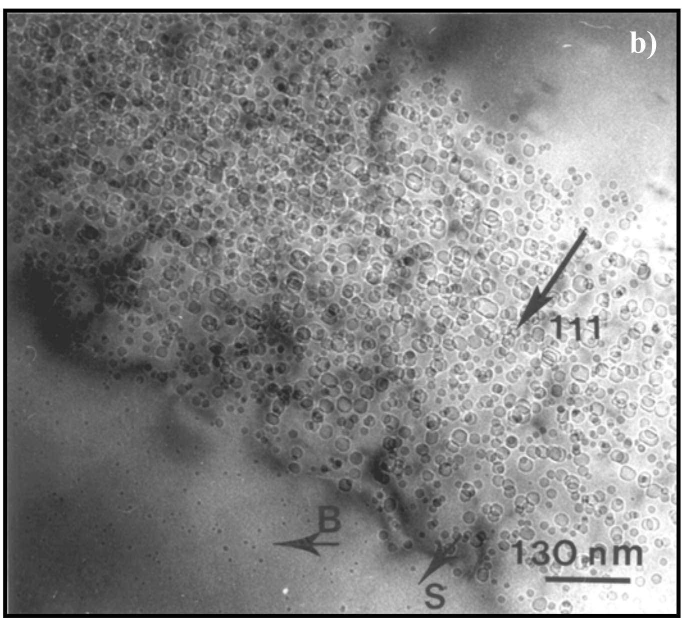

Figure 3.29: Cross-section TEM pictures obtained in Si after a 30 min anneal time (1x10^{17} He.cm^{-2}, 1.6 MeV, 800°C); **(a)** Visualization of the defects located behind the buried layer. **(b)** Bubble observation by kinematical diffraction condition : overfocused. Note the presence of small bubbles in front of the bubble layer indicated by an arrow.

They are elongated along $[\bar{1}\bar{1}2]$ directions in the $(1\bar{1}0)$ plane, corresponding to the $[0\bar{1}\bar{1}]$ directions in the (311) plane. All of these observations show that they are the "rodlike" defects lying on {113} planes. Dislocation loops located near R_p, accompanied by {113} defects extending to the bulk have been already reported after 2.3 MeV Si implantation and annealing at 800°C during 30 min [Brown *et al.* 1998]. These defects are known to consist of an agglomeration of excess Si interstitials stored in a (meta) stable configuration [Claverie *et al.* 1999]. So, it is obvious that they have grown in size during the anneal involving interstitial diffusion. The structure of the {113} defects and their evolution upon annealing have been extensively studied after Si keV implantation [Stolk *et al.* 1997]. In this case, it has been shown that upon annealing they grow in size and decrease in density only during the first stages of annealing; they are no longer detectable beyond 5 min. According to this it seems obvious that interstitial clusters created by the implantation and considered to be sinks for Si atoms were already present after the 15 min anneal, but were too small to be detected by TEM. The mean lifetime of these defects increases with increasing implant energy as already observed using keV energies [Eaglesham *et al.* 1995]. The formation of {113} defects may result from the clustering of excess self-interstitial atoms created by the implantation. However, we are not able to make any calculation of interstitial atoms due to the high density and to the size differences of these {113}s. The Frank loops which are located nearer to the buried layer than the {113}s, are not associated with bubbles the contrary of what was observed after the 15 min anneal. In this case, they may result from the precipitation of Si interstitials as in EOR defects.

The upper border of the bubble band is found to be at a depth of 5.8 μm, which is deeper than the location TRIM calculations predict. However, a layer of small bubbles, ≈ 200 nm wide, is observed in the region shallower than the band, see Fig.3.29b. The density of these small bubbles, near 3 nm in diameter, is estimated to be about 1×10^{16} bubbles.cm^{-3}. Thus, it seems that the first 200 nm of the bubble band have been annealed and only the small bubbles remain, i.e. the ones that have not coarsened. Few bubbles are present toward the surface as observed after the 15 min anneal. The diameter of the bubbles in the high damage region is in the range 5 - 25 nm.

In contrast to what is observed after keV implantation under similar conditions of annealing, where the smaller bubbles are localized close to the surface and the larger ones near the projected range region, the bubbles of different diameter are roughly homogeneously distributed in the buried band. Moreover, as expected the width of the bubble layer is greater

with increasing incident energy. No defects located behind the damaged zone have been reported after high dose helium keV implants and annealing in the same conditions [Follstaedt *et al.* 1993]. This puts more importance on the deposited energy, on the surface which is an attractive sink for the supersaturated layer of interstitials and on the role of the bubbles that may release self-interstitials during their formation and coarsening.

c) 500 minutes annealing

As is clear from Fig.3.30, all the {113} defects have disappeared after the 500 min anneal; only Frank loops are observed. They are known to be more stable than the {113}s and to persist to much longer times in annealing, as observed. They are now roughly homogeneously distributed up to 500 nm behind the buried layer with a mean radius $\bar{r}$ of about 15 nm. From the estimation of the Frank loop density n_d (cm^{-2}), the density of atoms per loop N_L has been calculated to be about $1x10^{14}$ cm^{-2} according to the following equation:

$$N_L = \frac{d_{111}}{e} \pi n_d \bar{r}^2 \quad (3.3)$$

where d_{111} is the atomic density of the (111) plane and e the measured depth over which the defects are seen on the cross-section image with **g** = 111. TEM investigations show that no bubbles are bound to them.

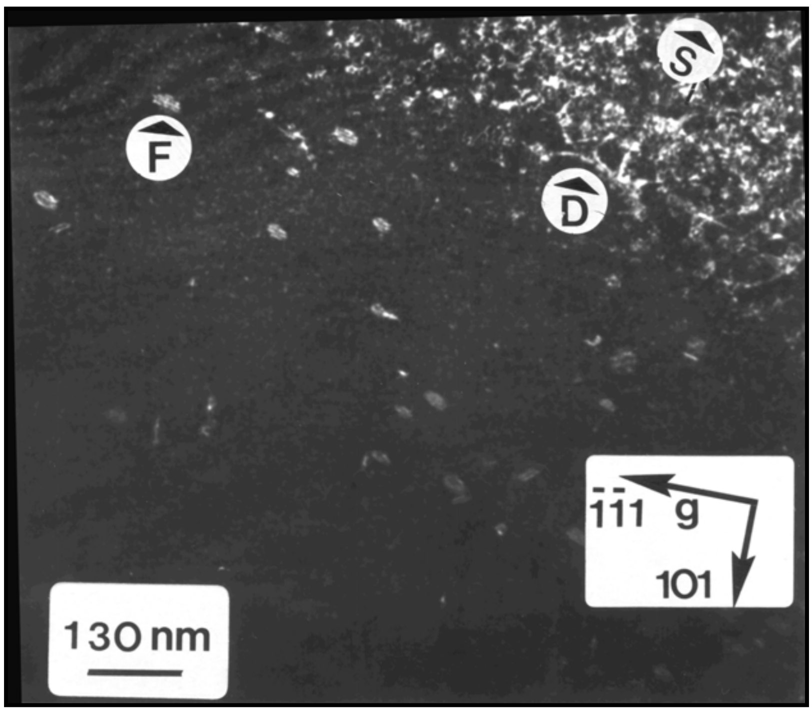

Figure 3.30: After a 500 min anneal time ($1x10^{17}$ $He.cm^{-2}$, 1.6 MeV, 800°C). Dark field cross-section image showing the Frank loops located behind the buried layer. Observation of dislocations (labeled D) in the bubble band.

Further studies are necessary to determine if the dislocation loops are affected by the dissolution or by the transformation of {113}s into loops. There are previous publications that already looked at the effects of {113} on dislocation loops, but in the latter case of keV Si implants, the length of the {113}s was in the 10 nm range [Eaglesham et al. 1995]. The same transformation does not seem to take place in the MeV implant case because of the large difference in size between both types of extended defect. The weak beam image clearly shows the presence of dislocation lines in the buried layer. No more change of its width has been observed. However, the size of bubbles becomes a bit larger on average when increasing annealing times, from 5 to 35 nm.

d) 17 h annealing

After 17 h annealing, no more defects are observed by TEM below the bubble layer, as shown in Fig3.31. The bubble diameter is in the range of 7 to 45 nm for a bubble band width near 500 nm. Note also that the 200 nm band of small bubbles in front of the buried layer is still observed. In Fig.3.32 the size distribution of the bubbles is shown for the shorter and longer annealing times. As shown, although some large bubbles were still present after the 15 min anneal, the size distribution of these was rather Gaussian whereas after 17 h anneal the distribution becomes strongly skewed toward the larger size. A similar behavior had also been observed for a 30 keV implantation after long time annealing [Follstaedt *et al.* 1996]. With increasing annealing time it seems that the population of small bubbles (<10 nm) does not change a lot and that the large ones still coarsen.

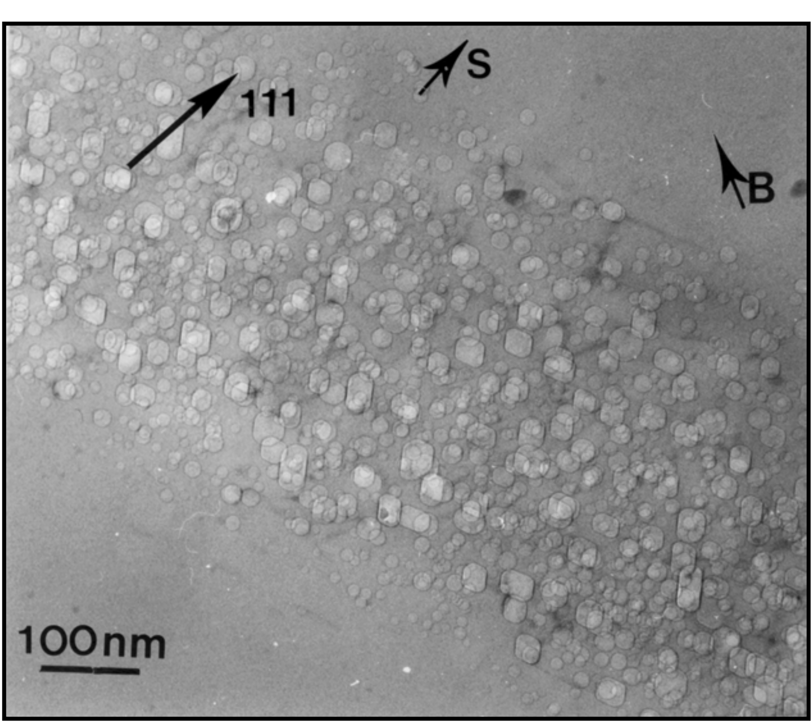

Figure 3.31: Cross-section TEM after a 1020 min anneal time ($1x10^{17}$ $He.cm^{-2}$, 1.6 MeV, 800°C) showing the bubble layer formed by a $1x10^{17}$ $He.cm^{-2}$ implant at 1.6 MeV after 17 h annealing at 800°C. No more defects are observed behind this layer.

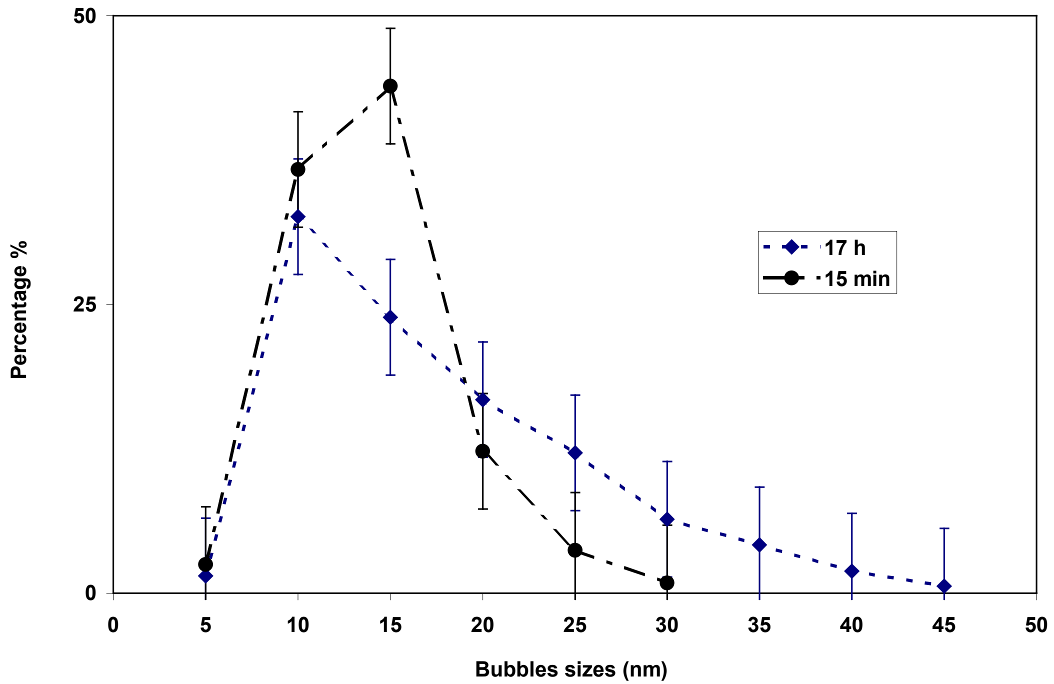

Figure 3.32: Size distribution of bubbles obtained in silicon implanted with helium at $1x10^{17}$ cm^{-2}, 1.6 MeV after annealing at 800°C for two annealing times : 15 min and 17 h.).

3.1.3.3 General remarks

By increasing annealing time the bubble diameter increases relatively little. As already observed after keV implantation and annealing it is clear that both bubble morphology and bubble density are affected more by the temperature of annealing than by the time of annealing although some coarsening of the bubbles does take place leading to slightly larger bubbles. This result is surprising since only 30% of helium has been shown to remain in cavities after the 17 h anneal whereas 90 % was still in cavities after the 15 min anneal [Godey *et al.* 2000]. On the contrary, the defects located behind the buried layer strongly depend upon the annealing time. The density of dislocations inside the band also decreases with annealing time. Two different mechanisms of coarsening of helium bubbles, depending on the experimental parameters (annealing times and helium concentrations), are known to operate in metals and metal alloys: the Ostwald ripening (OR) and migration and coalescence (MC) [Schroeder *et al.* 1991]. The elongated cavities observed after the short anneal (15 min) may have been formed by coalescence. They also tend to develop {110} facets. However, the vast majority of bubbles do not change their shape upon annealing indicating that the

migration and coalescence is difficult at this temperature. The bubble size even increases a little through the studied period. Moreover, complementary TEM observations on silicon implanted with helium at $5x10^{16}$ cm^{-2} and $1x10^{17}$ cm^{-2} following by an annealing at 800°C for 30 min do not show any significant changes in the mean radius of the bubbles – mean radius seems to be constant with increasing helium concentration c_{He}. This behavior, diameter independent of c_{He}, is expected in metals when the coarsening is controlled by the OR mechanism. In the same way, at 800°C no increase in the diameter has been reported in keV implanted silicon for doses between $1x10^{16}$ and $1x10^{17}$ $He.cm^{-2}$ [Raineri *et al.* 1995]. From our observations, it is difficult to precisely explain the mechanism responsible for bubble coarsening at this temperature. Further works is required to explain the observations under other experimental conditions.

3.1.2.4 Summary

Defects in silicon induced by high dose helium implantation are shown to be strongly dependent on the incident energy range. In the case of MeV helium implants in silicon at a dose of 10^{17} $ions.cm^{-2}$ followed by an 800°C anneal, two different layers of damage are observed. The first one is made up of a large density of bubbles with embedded dislocations whereas the second, located behind the first, contains two types of extended defects: the {113}s and the Frank loops. Whereas the bubble morphology does not really change during the annealing time, the extended defects are greatly affected. For a 15 min anneal, only Frank dislocation loops bound to bubbles are observed. For longer annealing time {113} defects are formed, which implies that Si interstitials are captured by the small interstitial clusters already formed by the implantation. With increasing annealing time, {113} defects dissociate and only Frank loops are observed. These are homogeneously distributed with a roughly constant size. They are more stable than {113}s and longer annealing times are needed to dissolve them, as we observe after a 17 h anneal. Further studies are necessary to determine the decay rates of both defects, the dominant loss mechanism of interstitials and the role of the bubble band in the injection of interstitial atoms which have escaped from the damage region. All these results show that the processes involved must be different from what has previously been observed for keV implantation where only one layer of bubbles is observed whatever the annealing time may be.

Anneal time (min)	Bubbles		Bubble band		{113} ?	Dislocation ?	Frank loops ?
	Size (nm)	Density (cm^{-3})	Distance to surface (µm)	Width (nm)			
As-implanted	3	-	5.5	700	✗	✗	✗
15	3-25	$2.5x10^{16}$	5.5	700	✓ ?	✗	✓
30	3-25	$1x10^{16}$ (3 nm)	5.4	500	✓	✗	✓
500	5-35	-	5.4	500	✗	✓	✓
1020	7-45	-	5.4	500	✗	✗	✗

Table.3.3 : Summary of the annealing time influence on bubble and defects formation in silicon for helium implantation ($1x10^{17}$ cm^{-2}, 1.6 MeV, anneal at 800°C).

References

[Beaufort *et al.* 1994] M. F. Beaufort, H. Garem, J. Lepinoux, *Phil. Mag. A* **69**, 881 (1994).

[Bonafos *et al.* 1997] C. Bonafos, M. Omri, B. de Maudit, G. BenAssayag, A. Claverie, D. Alquier, A. Martinez, D. Mathiot, *J. Appl. Phys.* **82**, 2855 (1997).

[Brown *et al.* 1998] R.A. Brown, O. Kononchuk, G.A. Rozgoni, S. Koveshnikov, A.P. Knights, P.J. Simpson, F. Gonzàlez, *J. Appl. Phys.* **84**, 2459 (1998).

[Claverie *et al.* 1999] A. Claverie, L.F. Giles, M. Omri, B. de Mauduit, G. BenAssayag, D. Mathiot, *Nucl. Instr. Methods Phys. Res. B* **147**, 1 (1999).

[Donnelly *et al.* 1991] S.E. Donnelly, D.R.G. Mitchell, A. van Veen, in *Fundamental aspects of inert gases in solids* edited by Donnelly and Evans, Plenum Press, New York, 357 (1991).

[Eaglesham *et al.* 1995] D.J. Eaglesham, P.A. Stolk, H.J. Gossmann, T.E. Haynes, J.M Poate, *Nucl. Instr. and Methods Phys. Res. B* **106**, 191 (1995).

[Follstaedt *et al.* 1993] D.M. Follstaedt, S.M. Myers, H.J. Stein, *Mat. Res. Soc. Symp. Proc* **279**, 105 (1993).

[Follstaedt *et al.* 1996] D.M. Follstaedt, S.M. Mayer, C.A. Petersen, J.W. Medernach, *J. Electr. Mat.* **25**, 157 (1996).

[Godey *et al.* 2000] S. Godey, T. Sauvage, E. Ntsoenzok, M.F. Beaufort, J.F. Barbot, B. Leroy, *J. Appl. Phys* **87**, 2158 (2000).

[Griffioen *et al.* 1987] C.C. Griffioen, J.H. Evans, P.C. De Jong, A. van Veen, *Nucl. Instr. Methods Phys. Res. B* **27**, 417 (1987).

[Raineri *et al.* 1995] V. Raineri, P.G. Fallica, G. Percolla, A. Battaglia, M. Barbagallo, S.U. Campisano, *J. Appl. Phys.* **78**, 3727 (1995).

[Raineri *et al.* 1996] V. Raineri, G. Fallica, S. Libertino, *J. Appl. Phys.* **79**, 9012 (1996).

[Schroeder *et al.* 1991] H. Schroeder, P.F.P. Fichtner, H. Trinkaus, in *Fundamental Aspects of Inert Gases in Solids* edited by S.E. Donnelly and J. H. Evans, Plenum Press, New York, 290 (1991).

[Siegele *et al.* 1995] R. Siegele, G.C. Weatherly, H.K. Haugen, D.J. Lockwood, L.M. Howe, *Appl. Phys. Lett.* **66**, 1319 (1995).

[Stolk *et al.* 1997] P.A. Stolk, H.J. Grossmann, D.J. Eaglesham, D.C. Jacobson, C.S. Rafferty, G.H. Gilmer, M. Jaraiz, J.M. Poate, H.S. Luftman, T.E. Haynes, *J. Appl. Phys.* **81**, 6031 (1997).

[Williams *et al.* 1993] J.S. Williams, R.G. Elliman, M.C. Ridway, C. Jagadish, S.L. Ellingboe, R. Goldberg, M. Petravic, W.C. Wong, Z. Dezhang, E. Nygren, B.G. Svensson, *Nucl. Instr. Methods Phys. Res. B* **80/81**, 507 (1993).

[Ziegler *et al.* 1985] J.F. Ziegler, J.P. Biersack, U. Littmark, *The Stopping and Range of Ions in Solids*, (Pergamon Press, New York, 1985).

3.2 He desorption from He implanted silicon at high temperature

In order to have better control over location, size, size distribution and defects associated with the cavities, numerous studies have been performed varying parameters such as implantation energy, dose or annealing parameters [Raineri *et al.* 2000]. However, the effects of varying the implantation temperature have not received much attention. Thus Si wafers have been implanted with He at different temperatures ranging from 200°C to 800°C. The interest in high temperature implantation is not only the possibility of substituting the annealing step after implantation but also of obtaining more information on secondary defect formation. A combination of TEM and THDS is used to study the effect of implantation temperature on the microstructure of defects and bubbles as well as the helium content and activation energy for helium release.

3.2.1 Experimental Procedure

All the experiments on silicon were performed on commercial n-n^+ silicon wafers. The n-type layer was epitaxially grown on a <111> orientated n^+ substrate of Czochralski silicon. The doping concentration of the 100 μm thick n-region was $1x10^{14}$ cm^{-3} (doped with phosphorus). These samples were implanted at a constant dose of $5x10^{16}$ $ions.cm^{-2}$ with 50 keV helium ions (Rp = 500 nm and ΔRp = 140 nm according to SRIM calculations [Ziegler *et al.* 1985]). The beam current was always kept at 40 μA. The implantations were carried out at different temperatures, up to 800°C, see Table.3.4. During the implantation the temperature was checked by a thermocouple in contact with the sample surface.

Sample name	Implantation temperature (°C)
Si 200	200
Si 400	400
Si 500	500
Si 600	600
Si 800	800

Table 3.4: Silicon samples used in the study.

The structure of the implantation damage was studied with cross-sectional TEM. The samples were thinned using ion milling and TEM images were obtained with a JEOL 200 CX operating at 200 kV. For studying cavities or bubbles with minimal contrast from the unavoidable accompanying lattice damage, specimens were tilted from their <110> orientation by few degrees in order to reduce diffraction effects. They were also imaged in under-focus and over-focus conditions to highlight the cavity edges with Fresnel contrast. In all the TEM pictures the as-implanted surface is indicated by an arrow and a letter *S*. THDS was used in the "oven configuration" (see appendix.1) with a heating rate of 5 K/s.

3.2.2 Conventional (isochronal) ramp annealing

3.2.2.1 200°C implantation

The thermal desorption spectrum of helium from the silicon sample implanted at 200°C obtained with a heating rate of 5 K/s is shown in Fig.3.33. Helium release clearly occurs partially at low temperature from 700 to 900 K and finally in a high temperature regime centered at about 1300 K with all the helium being released by 1400 K. The amount of helium retained in the sample is obtained by integrating the desorption curve. At an implantation temperature of 200°C, 90% of the implanted helium is retained in the sample. The cross-sectional micrograph of the 200°C implanted sample, Fig.3.34, shows a wide band of spherical bubbles with diameter ranging from 2 to 7 nm [David *et al.* 2001]. Helium bubbles can be seen as white spots with a dark edge in underfocus and as dark centers with a white edge in overfocus. The surrounding dark contrast visible in the band is due to the lattice damage. The band extends up to 630 nm. The largest bubbles are located in the deeper part.

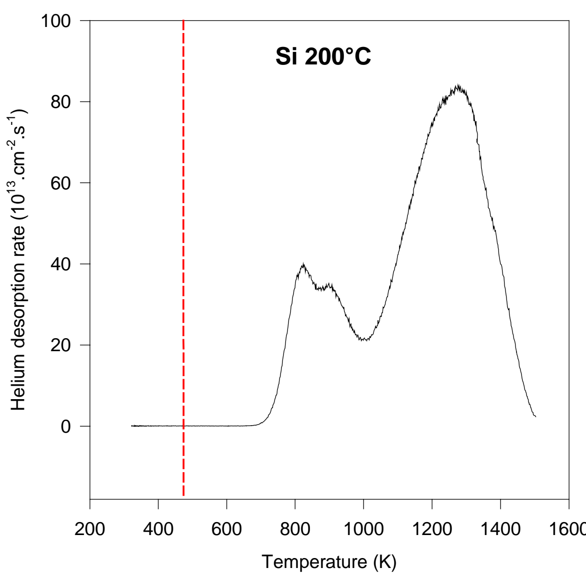

Figure 3.33: Helium desorption spectrum obtained after helium implantation at 200°C in silicon ($5x10^{16}$ cm^{-2}, 50 keV). Heating rate: 5 K/s. The red dashed line indicates the temperature of implantation.

Figure 3.34: cross-section TEM micrograph of bubbles in the 200°C-implanted silicon sample with helium at $5x10^{16}$ cm^{-2} and 50 keV. Kinematical diffraction condition: underfocus.

3.2.2.2 400°C implantation

For an implantation temperature of 400°C, helium release occurs only in the high temperature regime centered at about 1200-1300 K, with all the helium being released at 1400 K (Fig.3.35). A shoulder peak seems to appear at a temperature of 1000 K. At this implantation temperature only 66% of the implanted helium is retained in the sample. On the TEM micrograph, Fig.3.36, two regions of damage can be distinguished: a 350 nm wide buried layer made of spherical bubbles and certainly clusters of point defects and below this band up to the surface a region of spherical bubbles with few extended defects. Bubble diameter ranges from 7 to 20 nm. A few bubbles are elongated, indicating the beginning of a faceting process.

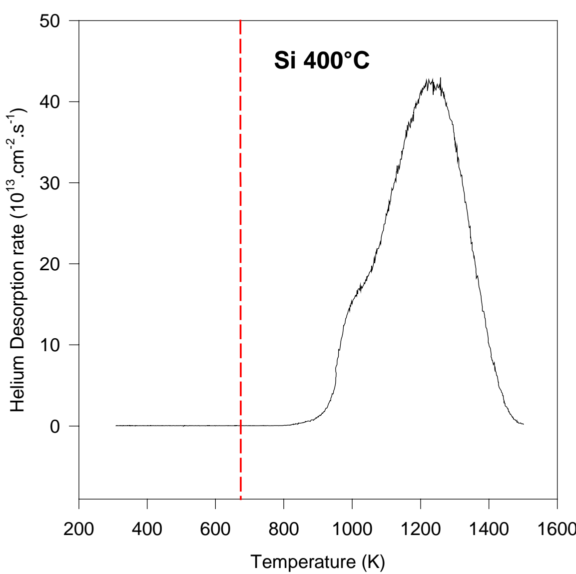

Figure 3.35: Helium desorption spectrum obtained after helium implantation at 400°C in silicon ($5x10^{16}$ cm^{-2}, 50 keV). Heating rate: 5 K/s. The red dashed line indicates the temperature of implantation.

Figure 3.36: cross-section TEM micrograph of bubbles in the 400°C-implanted silicon sample with helium at $5x10^{16}$ cm^{-2} and 50 keV. Kinematical diffraction condition: underfocus.

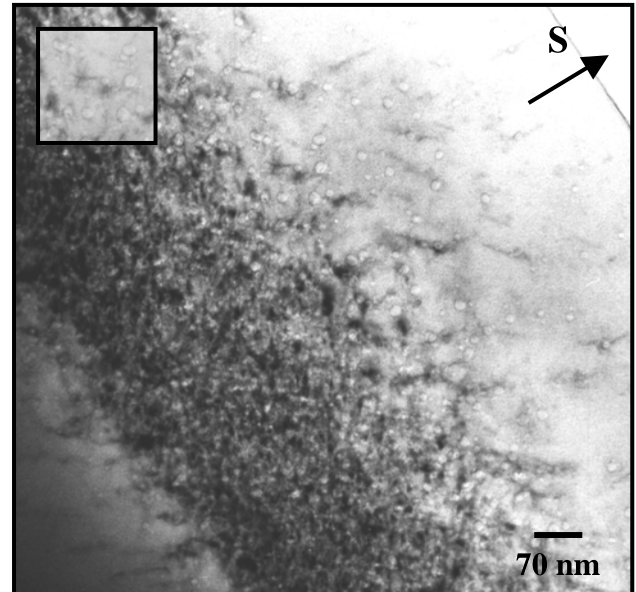

3.2.2.3 500°C implantation

At implantation temperature of 500°C, release of helium occurs between 900 and 1400 K and the shoulder peak observed previously at 1000 K is now clearly defined (Fig.3.37). Only 28% of the implanted helium is left in the sample. The TEM image in Fig.3.38 shows that two populations of bubbles can be distinguished: a population of small spherical bubbles with a mean diameter of 7 nm and a population of large faceted bubbles with diameter of about 20 nm. The faceting of these bubbles is typical of bubbles empty of gas, i.e. cavities [Follstaedt *et al.* 1993]. Moreover the bubble/cavity density seems to be lower than the one observed for the lower temperatures.

Figure 3.37: Helium desorption spectrum obtained after helium implantation at 500°C in silicon ($5x10^{16}$ cm^{-2}, 50 keV). Heating rate: 5 K/s. The red dashed line indicates the temperature of implantation.

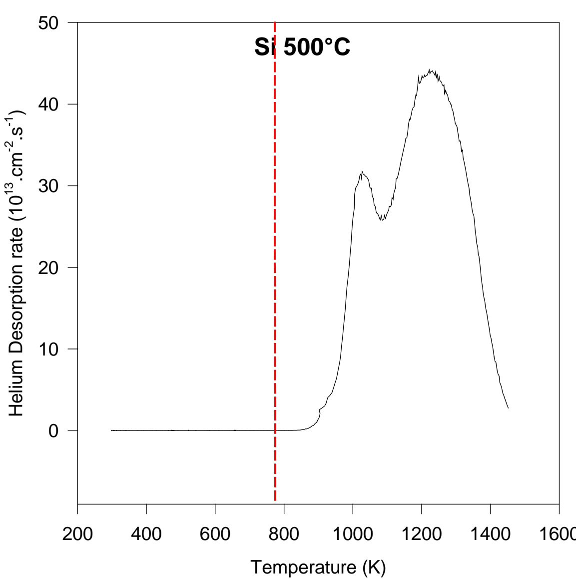

Figure 3.38: cross-section TEM micrograph of bubbles in the 500°C-implanted silicon sample with helium at $5x10^{16}$ cm^{-2} and 50 keV. Kinematical diffraction condition: underfocus.

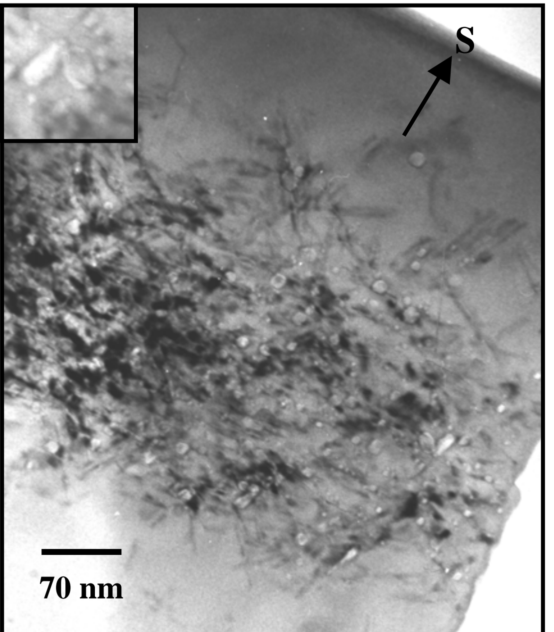

3.2.2.4 600°C implantation

Fig.3.39 shows that at the implantation temperature of 600°C the very small amount of helium retained in the sample after implantation (0.02%) is released at high temperature only, at about 1200 K. To confirm that the observed spectrum was due to the release of helium from the sample and not to the background, a desorption measurement with the quadrupole in scanning mode was proceeded on another part of the sample. In this mode the quadrupole is asked to scan over a range of masses during a short time (220 ms). The results presented in Fig.3.40 clearly show that the observed peak is due to helium release from the sample and that the background is low. In Fig.3.41 a well-defined 250 nm wide bubble/cavity band is observed. The biggest cavities (~20 nm) are now clearly faceted (see inset in Fig.3.41) but small spherical bubbles (~2-3 nm) are still observed.

Figure 3.39: Helium desorption spectrum obtained after helium implantation at 600°C in silicon ($5x10^{16}$ cm^{-2}, 50 keV). Heating rate: 5 K/s. The red dashed line indicates the temperature of implantation.

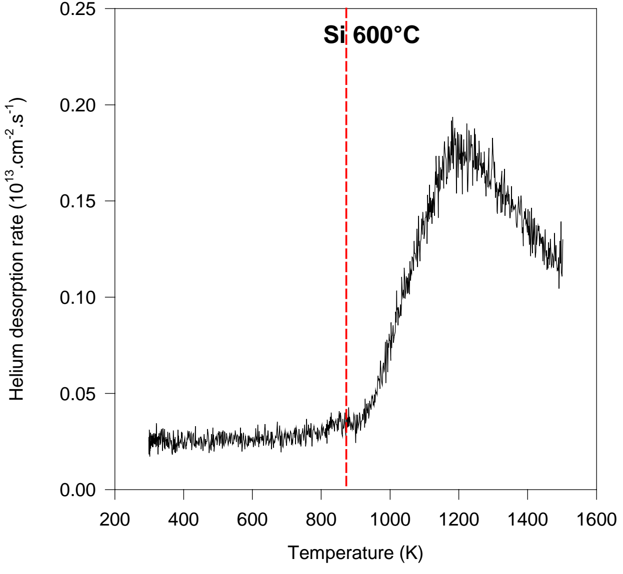

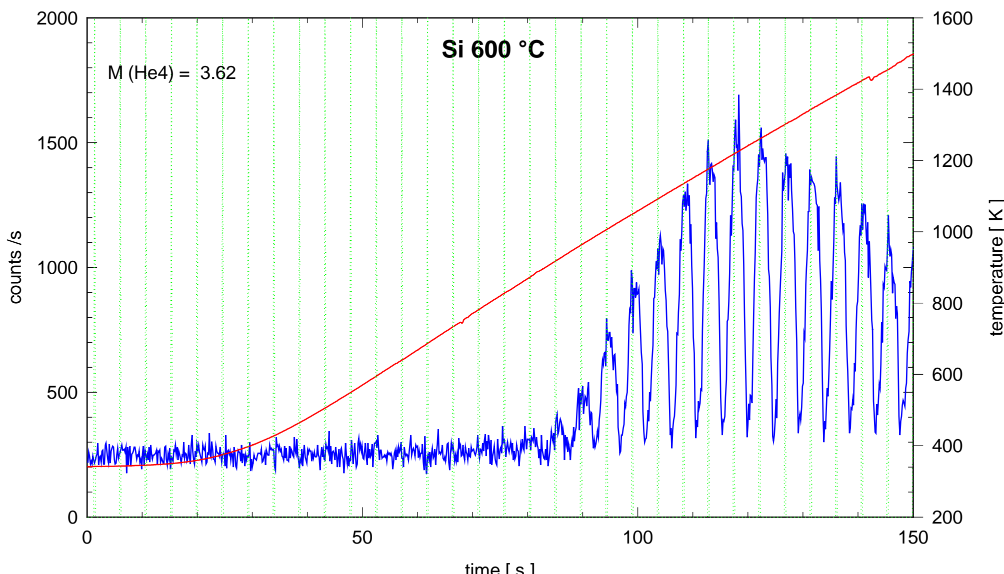

Figure 3.40: Helium desorption spectrum obtained after helium implantation at 600°C in silicon ($5x10^{16}$ cm^{-2}, 50 keV) while scanning from mass 3.2 to 4.03. Scanning speed 10 s/amu. Heating rate: 5 K/s. The green dashed lines indicate the mass of ^{3}He.

Figure 3.41: cross-section TEM micrograph of bubbles in the 600°C-implanted silicon sample with helium at $5x10^{16}$ cm^{-2} and 50 keV. Kinematical diffraction condition: underfocus.

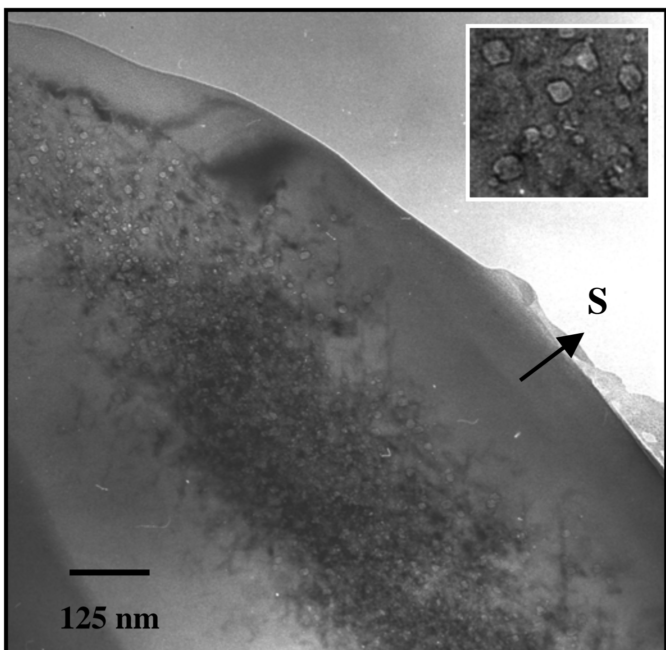

3.2.2.5 800°C implantation

At 800°C-implantation, Fig.3.42, not much difference from 600°C is observed apart from the helium content which is even lower (0.01%). Again a scanning mode desorption spectrum was obtained and shows that helium is released from the sample (Fig.3.43). It also confirms

that the release of helium is surprisingly initiated at a temperature below the implantation temperature.

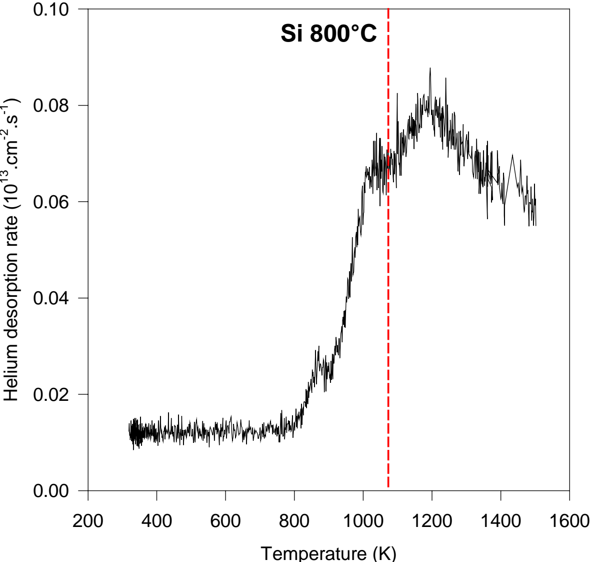

Figure 3.42: Helium desorption spectrum obtained after helium implantation at 800°C in silicon ($5x10^{16}$ cm^{-2}, 50 keV). Heating rate: 5 K/s. The red dashed line indicates the temperature of implantation.

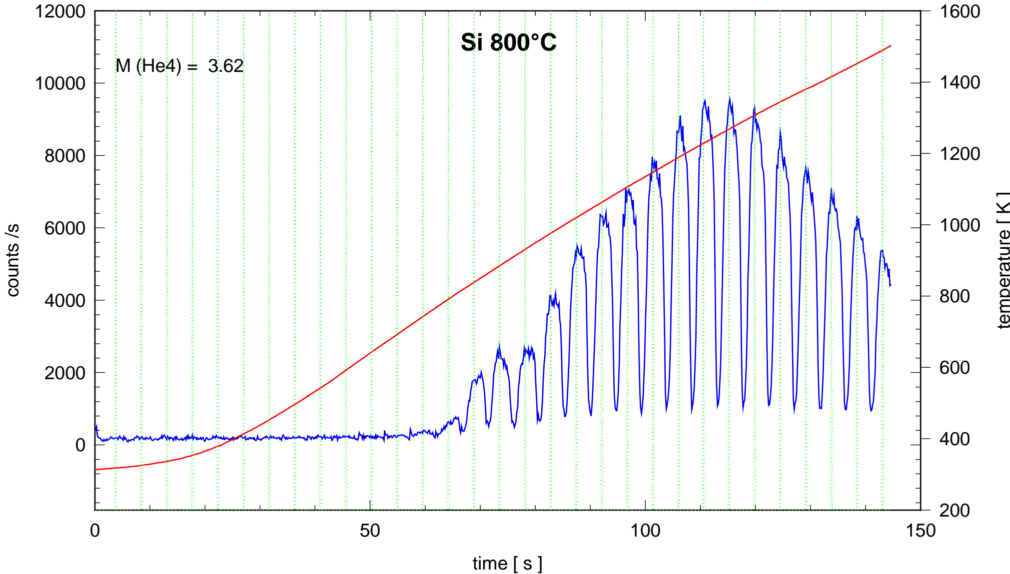

Figure 3.43: Helium desorption spectrum obtained after helium implantation at 800°C in silicon ($5x10^{16}$ cm^{-2}, 50 keV) while scanning from mass 3.2 to 4.03. Scanning speed 10 s/amu. Heating rate: 5 K/s. The green lines indicate the mass of ^{3}He.

Fig.3.44 reveals that no bubbles/cavities are left in the sample after this high temperature implantation. Only extended defects are observed.

Figure 3.44: cross-section TEM micrograph of bubbles in the 800°C-implanted silicon sample with helium at $5x10^{16}$ cm^{-2} and 50 keV.

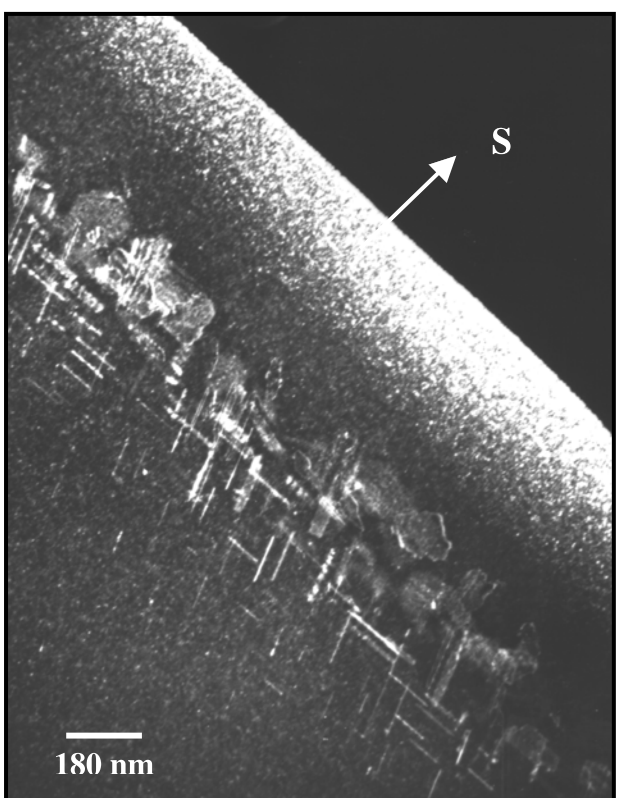

3.2.3 Partial annealing measurements

In order to obtain more information, the different samples were also subjected to partial annealing (Fig.3.45a). The sample is annealed by steps instead of one single continuous run. The sample is first heated up to a certain temperature and cooled down. This is repeated each time with a temperature increment of 50 K. This method keeps the release rates low, i.e. no saturation of the quadrupole, and allows a better analysis of the desorption mechanism. Considering that the release is a first order desorption process and that for the initial part of each desorption curve the number of filled traps (N) is constant, the Arrhenius graph of the release rate versus $1/T$ can be plotted (Fig.3.45b).

It was found by Griffioen *et al.* [1987] that the release rate of helium from bubbles in silicon could be described rather well by a model based on the permeation of helium from bubble to the sample surface. The helium release rate can be written as (eq.3.4):

$$\frac{dN}{dt} = A\exp\left(-\frac{\Delta H}{kT}\right) \tag{3.4}$$

where ΔH is the activation enthalpy for permeation, i.e. the sum of the migration enthalpy and the solution enthalpy of helium (eV), k the Boltzmann constant ($eV.K^{-1}$), and T the absolute temperature (K). The activation enthalpy for permeation can be derived from the slopes of the curves in the partial annealing plot. Furthermore, the pre-exponential factor A_i of the different partial annealing can be also derived from the measurements, with i denoting the ith partial annealing. The pre-exponential factor A depends on the morphology of the bubbles system. For isolated bubbles A can be written as (eq.3.5) [Griffioen *et al.* 1987]:

$$A = -3NP/(rR) \tag{3.5}$$

where N is the number of filled traps, R the average distance of the bubbles to the surface, r the bubble radius and P the permeation rate factor which is pressure dependent. For a bubble layer with helium gas at low pressure, A is described by (eq.3.6) [Godey *et al.* 2000]:

$$A = -NP/(d_c R) \tag{3.6}$$

where d_c is the effective thickness of the cavity layer, i.e. the void fraction times the layer thickness. It can be calculated that inter-bubble diffusion of helium within the bubble band is fast compared to the release rate. Therefore, it is justified to consider the bubble band as a single gas reservoir. However, the effects of helium pressure on permeation are not well known but should be taken into account.

The results presented in Fig.3.45 show that helium release mechanism is always governed by a single activation energy whatever the implantation temperature may be. Indeed, in all implanted samples, the slopes of the Arrhenius plots are found to be identical. The activation energy of the process has been found to be equal to 1.8 eV. This value is in line with those already found by diverse authors [Griffioen *et al.* 1987, Godey *et al.* 2000, Wieringen *et al.* 1956] in case of room temperature (RT) implantations, see Table.3.5.

Implantation parameters			**Activation energy (eV)**	**Source**
Energy (keV)	**Dose ($He.cm^{-2}$)**	**Temperature (°C)**		
2.5	$2x10^{16}$	RT	1.70	Griffioen *et al.* [1987]
1600	$5x10^{16}$	RT	1.83	Godey *et al.* [2000]
50	$5x10^{16}$	200-800	1.80	This work

Table 3.5: Activation energy for He permeation from bubbles in silicon.

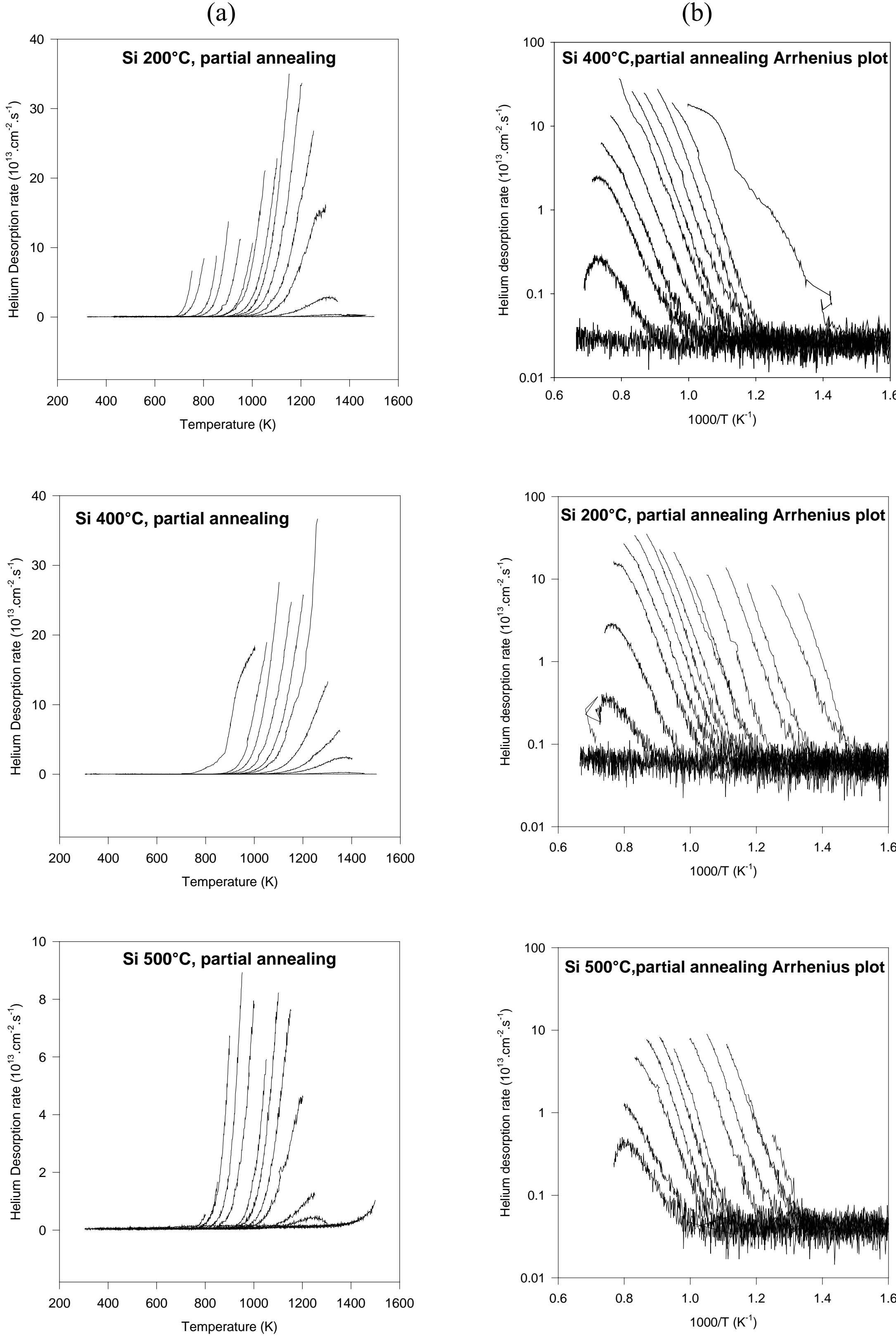

Figure 3.45: (a) Partial desorption spectrum of the silicon samples implanted with helium at the indicated temperature (50 keV and $5x10^{16}$ cm^{-2}). Heating rate: 5 K/s. **(b)** Partial annealing Arrhenius plots derived from the desorption measurements of (a).

3.2.4 Discussion

It is well known that the most stable position of helium in silicon is the interstitial position. Simulations [Alatalo *et al.* 1992] and RBS (Rutherford Backscattering) measurements [Allen *et al.* 1993] have shown that the helium sits preferentially in a tetrahedral interstitial site (T_d) which is the lowest energy configuration. Moreover, helium atoms seem to occupy adjacent T_d sites to form complexes. The solution enthalpy of interstitial helium in silicon is low, H_S = 0.46 eV, whereas the migration energy is large, E_{mig}^{He} = 1.34 eV. These values have been obtained by Van Wieringen and Warmoltz [1956] and are shown in the potential energy diagram of the system He-Si (Fig.3.46).

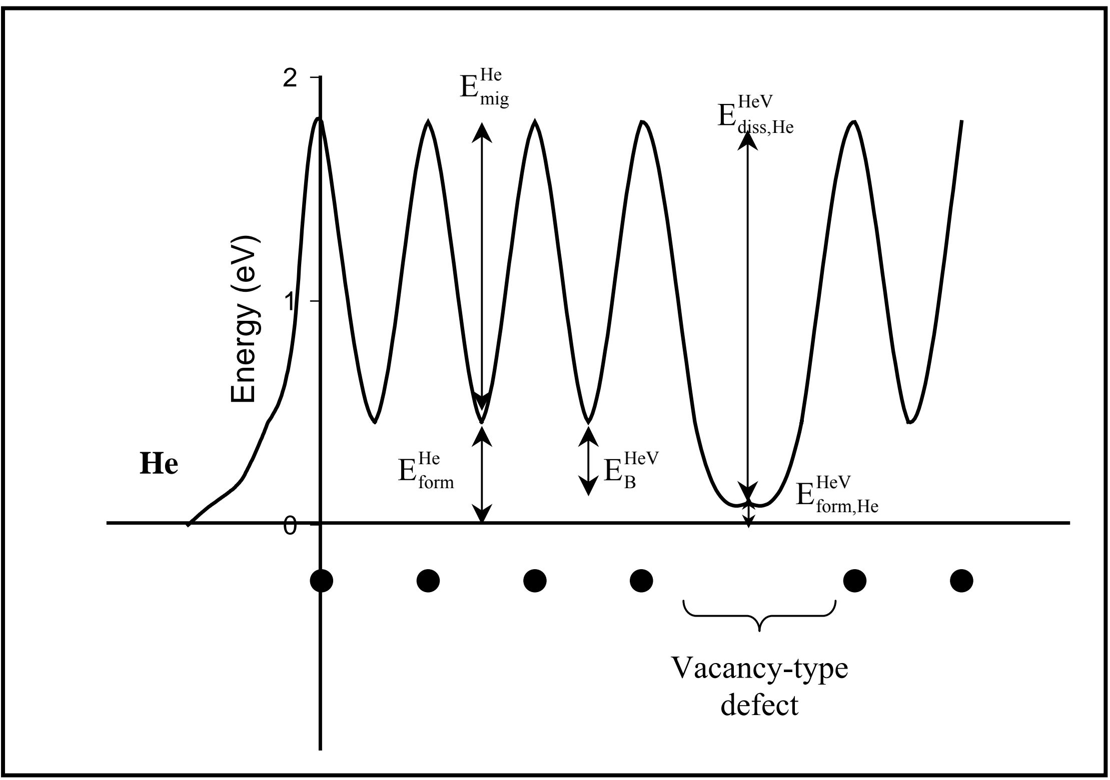

Figure 3.46: Potential energy diagram of helium in interaction with silicon. Helium at an interstitial position and helium at a vacancy are indicated. E_{form}^{He}, E_{mig}^{He} : formation and migration energies of interstitial He, $E_{form,He}^{HeV}$, $E_{diss,He}^{HeV}$: formation and migration energies of helium in interaction with a vacancy-type defect, E_{B}^{HeV} : bending energy of He with a vacancy-type defect.

A direct consequence is that the dissociation energy of helium from any defect in silicon should not exceed 1.7 eV, assuming that the van der Waals binding of helium with silicon can be neglected. Applying simple first-order detrapping mechanism (Eq.3.7):

$$\frac{dN}{dt} = -N\nu \exp\left(-\frac{Q}{kT}\right) = -N\nu \exp\left(\frac{\Delta S}{k} - \frac{E_{diss}}{kT}\right) \quad (3.7)$$

where N is the number of filled traps,ν = the attempt frequency (s^{-1}), Q the activation energy, E_{diss} the dissociation energy (eV), k the Boltzmann constant ($eV.K^{-1}$) and T the absolute temperature (K), with attempt frequencies of the order of the Debye frequency ($\nu = 10^{13}$ s^{-1}) and neglecting entropy effects, desorption temperatures not higher than 644 K would be expected. However, desorption results presented above show helium desorption temperatures as high as 1300 K (Fig.3.33). Thus entropy effects seem to be important. By analysis of the desorption peak obtained for helium desorption from cavities, Van Veen *et al.* [1991, 1993] has found a value of $\Delta S = -8k$, with k the Boltzmann constant, for the entropy of solution. The negative entropy change is explained as follow: the helium goes from the gas phase with high entropy to the interstitial state where it can be considered as an harmonical vibrating particle in a deep potential well with a low entropy. Thus, for cavities or bubbles entropy effects should be taken into account. For small defects, i.e. for monovacancies and small vacancy clusters, the trapped state of the helium can be described as a particle vibrating with a frequency ω_t in a three-dimensional potential well. It is evident that in this case the entropy change, from the trapped state to the interstitial state, will be small and thus the entropy effects can be neglected so that the desorption from these defects is found in the expected temperature region.

Another striking effect is the pressure within the bubbles. The detrapping of helium from defects can be written as follows (eq.3.8):

$$\frac{dN}{dt} = -4\pi r D c_{He} N = -4\pi r D N \exp\left(\frac{\mu_{He}}{kT} - \frac{G_{He}}{kT}\right) \quad (3.8)$$

where c_{He} is the helium concentration, μ_{He} the chemical potential of the helium, G_{He} the Gibbs free energy of the bulk dissolved helium, D the diffusivity of the helium and r the radius of the defect. For high helium pressure (> 100 MPa) the concentration can no longer be derived from the ideal gas law, but μ_{He} must be derived from the equation of state of high pressure helium [Mills *et al.* 1980]. In Fig.3.47, the calculated desorption spectra for different bubble sizes and pressures are shown [from Van Veen *et al.* 1991]. The change in size and/or in the chemical potential of helium, induces differences in the temperature T_p of maximum release and in the FWHM-width $T_+ - T_-$.

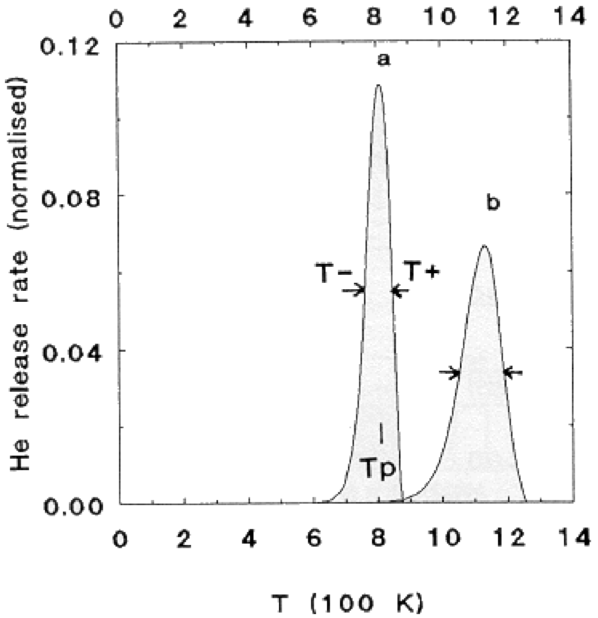

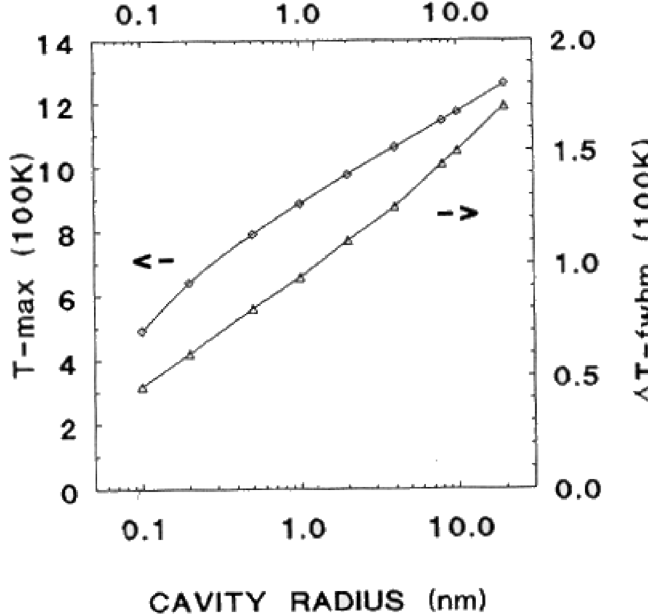

Figure 3.47: (a) Calculated desorption spectra for cavities in silicon with a) r = 0.6 nm and P = 15 kbar, b) r = 10 nm and P = 1 kbar. The helium dissociation energy is 1.7 eV and the heating rate 10 K/s. **(b)** Temperature at peak maximum (T_P) and the FWHM temperature interval (T_+ , T_-) of calculated desorption peaks for bubbles with r = 1 nm and varying pressure. The solid lines indicate results of calculation using Mills EOS. The dashed lines represent results for ideal gas. **(c)** T_P and the FWHM versus cavity radius. (see ref. [Van Veen *et al.* 1991])

The increase of the pressure in a bubble considerably enhances the detrapping probability. The effect can be again attributed to the entropy change. In the bubble at high pressure the entropy of the gas will be lower than in the void. The entropy difference ΔS = S(dissolved He)-S(He in bubbles) will be increased leading to a shift of the temperature of maximum release towards the low temperature side.

Two desorption processes are distinguished to describe the helium release from silicon. The low temperature side, is generally governed by helium release from interstitial position and/or from small unstable defects. This process involves diffusion of helium through the silicon lattice. In this study, it is never observed since the implantations were carried out at high temperatures. As for helium release in the high temperature side it is described by permeation

from voids to the surface. Indeed, the peak observed at 1200-1300 K for 200-600°C implantation temperatures is identified from earlier work [Griffioen *et al.* 1987, Van Veen *et al.* 1993], as release by permeation from interior voids. The peak at 800 K observed for the 200°C implantation is similar to the desorption from voids but is shifted to lower temperature. It is ascribed to pressurized helium bubbles as explained above. A peak at 800 K in silicon has been also assigned to pressurized argon bubbles in argon-irradiated silicon [Van Veen *et al.* 1991]. The temperature of maximum release as well as the FWHM value observed is in line with the calculated values for a bubble of 1 nm presented in Fig.3.47. Moreover, the dark contrast visible in the TEM image (Fig.3.34) around some of the bubbles is also consistent with an overpressurized state [Fichtner *et al.* 1997]. The shoulder peak at 1000 K appearing for the 400 and 500°C implantations could be also related to the nucleation of larger overpressurized bubbles with increasing implantation temperature. From Fig.3.47, the observed temperature of maximum release and the FWHM value is in accordance with a bubble size of 3 nm. At an implantation temperature of 800°C, the very small helium release detected can not be attributed to permeation from cavities since none of them are observed by TEM. It seems that the only defects created during this high temperature implantation are stacking faults, dislocations and {311} defects. These defects, which offer less room for helium than cavities, could be responsible for this small release. It is quite surprising that some helium is still present in the sample after such high implantation temperature. So is its release at a lower temperature than the implantation temperature. This could be explained by the residual He staying in the implantation chamber after implantation. He is still highly mobile and because of the very high permeability of silicon an equilibrium will be established between He in the chamber and He in the sample. During cooling down, the He concentration decreases but a small amount will be trapped in the sample at the above mentioned defects.

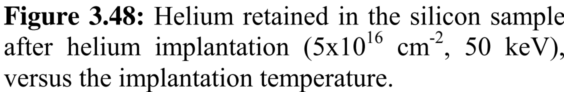

Figure 3.48: Helium retained in the silicon sample after helium implantation ($5x10^{16}$ cm^{-2}, 50 keV), versus the implantation temperature.

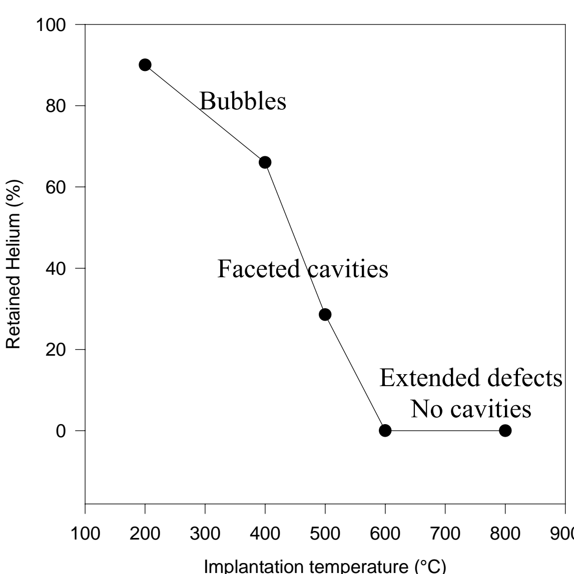

The amount of retained helium in the samples, derived from the desorption results, is plotted in Fig.3.48 versus the implantation temperature. It is clearly observed that the amount of retained helium decrease with implantation temperature. The amount is dramatically reduced at 600°C, temperature at which a strong faceting of cavities is observed.

3.2.5 Conclusion

The helium desorption from helium implanted silicon at high temperature has been studied. From this study some important processes and behaviour has been discovered:

(1)-A temperature of 600°C is needed during implantation to create cavities empty of gases.

(2)-Entropy effects play a major role in the helium desorption from bubbles.

(3)-Helium release from voids/bubbles in silicon is well described by permeation from cavities to the surface.

(4)-Partial desorption results show that the release of helium by permeation from bubbles/voids to the surface has an activation energy 1.8 eV whatever the implantation temperature may be, and also whatever the implantation energy may be.

References

[Alatalo *et al.* 1992] M. Alatalo, M.J. Puska, R.M. Nieminen, *Phys. Rev. B*, **46**, 12806 (1992).

[Allen *et al.* 1993] W.R. Allen, *Mat. Res. Soc. Symp. Proc.*, **279**, 433 (1993).

[David *et al.* 2001] M.L. David, M.F. Beaufort, J.F. Barbot, *to be published* (2001).

[Fichtner *et al.* 1997] P.F.P. Fichtner, J.R. Kaschny, R.A. Yankov, A. Mücklich, U. Kreiβig, W. Skorupa, *Appl. Phys. Lett.* **70**, 732 (1997).

[Follstaedt *et al.* 1993] D.M. Follstaedt, S.M. Myers, H.J. Stein, *Mat. Res. Soc. Symp. Proc.* **279**, 105 (1993).

[Godey *et al.* 2000] S. Godey, E. Ntsoenzok, T. Sauvage, A. van Veen, F. Labohm, M.F. Beaufort, J.F. Barbot, *Mater. Sci. Eng. B* **73**, 54 (2000).

[Griffioen *et al.* 1987] C.C. Griffioen, J.H. Evans, P.C. de Jong, A. van Veen, *Nucl. Instr. Meth. Phys. Res. B* **27**, 417 (1987).

[Mills *et al.* 1980] R.L. Mills, D.H. Liebenberg, J.H. Bronson, *Phys. Rev. B* **21**, 5137 (1980).

[Raineri *et al.* 2000] V. Raineri, M. Saggio, E. Rimini, *J. Mater. Res.* **15**, 1449 (2000).

[Van Veen *et al.* 1991] A. van Veen, in: *Fundamental Aspects of Inert Gases in Solids*, S.E. Donnelly, J.H. Evans (Eds)., NATO ASI series B, Physics 279, Plenum Publishing Corp., New York, 1991, pp 41-57.

[Van Veen *et al.* 1993] A. van Veen, A.H. Reader, D.J. Gravesteijn, A. van Gorkum, *Thin Solid Films*, **241**, 206 (1993).

[Wieringen *et al.* 1956] A. van Wieringen, N. Warmoltz, *Physica*, **22**, 849 (1956).

[Ziegler *et al.* 1985] J.F. Ziegler, J.P. Biersack, U. Littmark, *The Stopping and Range of Ions in Solids*, (Pergamon Press, New York, 1985).

4-Helium implantation in silicon carbide

4.1 High energy implantation

Silicon carbide (SiC) is a semiconductor which offers many technological opportunities for applications in electronic devices operating under extreme conditions such as high temperature, high power and high-frequency applications [Capano *et al.* 1997]. As ion beams are already widely used in semiconductor technology, ion implantation in SiC could thus be used to dope it or to lower the diffusion temperature of dopants. A fundamental understanding of irradiation damage in SiC as well as its recovery is thus needed for advances in technological applications. High-dose implantation of light particles has recently received growing interest as a technique to control the charge carrier lifetime in silicon power devices and to create gettering sites such as bubble structures in the case of helium implantation in silicon [Follstaedt *et al.* 1996, Raineri *et al.* 1995]. As previously seen (cf. §.3), under appropriate conditions, helium implantation into silicon leads to cavity formation that can trap by chemisorption metallic impurities [Follstaedt *et al.* 1996]. MeV ion implantation gives the opportunity to produce a thicker damage layer at a few microns deep. SiC is, however, easily amorphized by ion implantation at room temperature. Damage produced by light ions leads to amorphization when the elastic energy density exceeds $2x10^{21}$ keV/cm^3 for a room temperature implantation [Spitznagel *et al.* 1986]. Recrystallisation is strongly expected during the post-implantation annealing involved in the control of cavity morphology as well as their thermal stability. "Explosive" regrowth has been found to take place at temperatures above 1450°C [McHargue *et al.* 1993]. This temperature can, however, be lowered using the ion-beam-induced epitaxial crystallization (IBIEC) process [Heera *et al.* 1995] as observed in several semiconductors.

In this study we report an investigation of bubble formation by high dose MeV helium implantation into n-type 4H-SiC. Different anneals have been performed with the intent of forming stable cavities. After giving details on experimental procedures, the results are presented along with their interpretation. We then discuss our results in the light of relocation processes and finally present some conclusions.

4.1.1 Experimental procedure

Commercially single crystals of n-4H-SiC were used in this study. The $(0001)_{Si}$ faces of samples were room temperature implanted at 1.6 MeV using a Van de Graaff accelerator (CERI, Orléans) with a dose of $1x10^{17}$ ions/cm^2. SRIM simulation [Ziegler *et al.* 1985] shows that the maximum of the particle distribution R_p is expected at about 3.6 μm from the surface ($\Delta R_p \approx 0.1$ μm) with a maximum in the deposited elastic energy density of approximately 10^{22} keV/cm^3. A maximal peak concentration of about 4 at.% He is predicted for this implantation. This value is much larger than the threshold concentration of 1.6 at.% found to form stable cavities in silicon [Follstaedt *et al.* 1996]. After implantation, some of the samples were subjected to subsequent anneals. The first anneal was carried out at 800°C for 30 min in an evacuated quartz tube within a tubular furnace. In addition, an in-situ TEM anneal up to 820°C was done using a heating sample holder in order to follow the changes in the microstructure of the buried layer. The second anneal was done for 30 min at 1500°C under high vacuum ($<10^{-6}$ Pa) with a slow heating rate. In that case, the whole annealing procedure took 6.5 hours. Conventional TEM observations were made using a JEOL 200CX microscope operating at 200 kV while high resolution experiments were performed with a JEOL 3010 operating at 300 kV. Cross sectional TEM foils were prepared by ion beam milling to electron transparency. X-ray diffraction (XRD) measurements in the symmetrical position (θ, 2θ) were conducted with the Cu $K_{\alpha 1}$ radiation (λ = 0.154 nm) from a 5 kW RIGAKU RU-200 generator. The X-ray penetration depth in SiC for the studied Bragg reflections varies from 10 to 20 μm. Infrared Reflectivity (IRR) measurements were performed with a BOMEM MB 100 FTIR spectrometer at a near normal incidence with wave numbers ranging from 300 to 6000 cm^{-1}.

4.1.2 Results and discussion

4.1.2.1 As-implanted

A low magnification cross sectional TEM image aligned near a $[11\bar{2}0]$ direction shows that helium implanted at a dose of $1x10^{17}$ cm^{-2} produces a continuous damaged layer of approximately 650 nm in width at about 3.6 μm deep below the surface, as expected from

SRIM calculations. A closer view shows that this damaged band is made up of three different regions denoted by A, B and C in Fig.4.1. A selected area diffraction pattern of the B layer

Figure 4.1: Cross sectional TEM image of 4H-SiC subjected to room temperature helium implantation (1.6 MeV, $1x10^{17}$ cm^{-2}, no anneal). In the inset, diffraction pattern of the B zone (amorphous state).

shows a halo pattern corresponding to the amorphous phase while A and C are crystalline 4H-SiC. The 400 nm wide amorphous region B can be divided in two regions B1 and B2. The B1 region is related to the presence of small bubbles, 1-2 nm in diameter whereas the B2 part does not show any visible defects. Their widths are about 280 and 120 nm respectively. However, in contrast to what can be observed in implanted silicon under the same implant conditions, zones of dark contrast, A and C, are found outside the central band B. The black contrast observed in these surrounding layers may result from defects not resolvable by TEM. The A band, lying in front of the B layer shows a wider extent (170 nm) and a lower defect density than the C one located below (55 nm). The C band also contains some small bubbles whereas no bubble is visible in the A band. High dose implantation of helium at room temperature into SiC thus produces small bubbles located at the end of the damage layer. A similar damage structure has been already reported in 6H-SiC implanted at 650 °C with 180 keV O^+ [Ishimaru *et al.* 1999]. The authors argue that this is the consequence of the elastic loss profile and of in-situ defect annealing during implantation. Previous studies [Grimaldi *et al.* 1997, Frangis *et al.* 1996] on irradiated 6H-SiC with 1 MeV He ions at $2x10^{17}cm^{-2}$ have

already reported the presence of an amorphous buried layer in the region where the elastic loss exceeds the critical value of $2x10^{21}$ keV/cm^3. They also report observation of defect clustering in the regions adjacent to the amorphous band. However, they do not mention any bubble formation. In hot-pressed 4H- and 6H-SiC, observations of platelets have been reported for implantation of 2450 at.ppm He [Chen *et al.* 2000]. These platelets of 9 nm in diameter do not show any major evolution until annealed at 1100°C anneals. Platelets have also been observed for hydrogen implantations using similar conditions but after annealing only. [Grisolia *et al.* 2000]**.** In the case of high implanted doses, we do not observe any platelets of cavity-type but we do observe bubbles and point defects clusters. The same behavior also occurs in 6H-SiC since we only observe prismatic loops after a $2x10^{16}$ He.cm^{-2} implantation followed by an annealing at 800°C [Oliviero *et al.* 2000].

Figure 4.2: X-ray (0008) Bragg reflection for the unimplanted 4H-SiC (dotted line) and implanted 1.6 MeV, $1x10^{17}$ cm^{-2}sample (solid line).

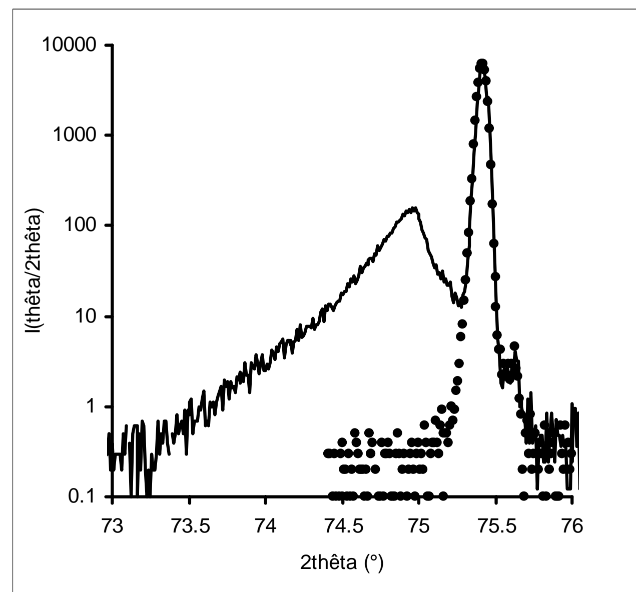

Fig.4.2 shows an X-ray diffraction experiment in the symmetrical position (θ, 2θ) for the (0008) Bragg reflection. Two peaks are clearly observed: a sharp peak due to the unperturbed SiC and a broadened peak, towards the low angle side, ascribed to an oriented dilatation along the c-axis inside the crystalline perturbed regions. The mean value of the dilatation is calculated using Eq.(4.1):

$$\frac{\Delta c}{c} = -ctg\theta.\Delta\theta \qquad (4.1)$$

and is found to be ~ $5x10^{-3}$. This dilatation could be ascribed to clustering of interstitials in the (0001) plane and/or to the stress induced by the amorphous layer of lower density.

The FTIR spectrum exhibits an interference pattern as shown in Fig.4.3, relative to the weak modification of the optical refractive index n of the implanted layer. The position of the perturbed band d is calculated using Eq.(4.2):

$$d \approx \frac{1}{2n.\Delta f} \qquad (4.2)$$

where Δf is the spacing between two reflectance minima. With a mean value of Δf ~ 450 cm^{-1} and taking n(SiC) ~ 3.1 [Harris *et al.* 1995, Declémy *et al.* 2002] we obtain d ~ 3.6 μm. This value is consistent with SRIM calculations.

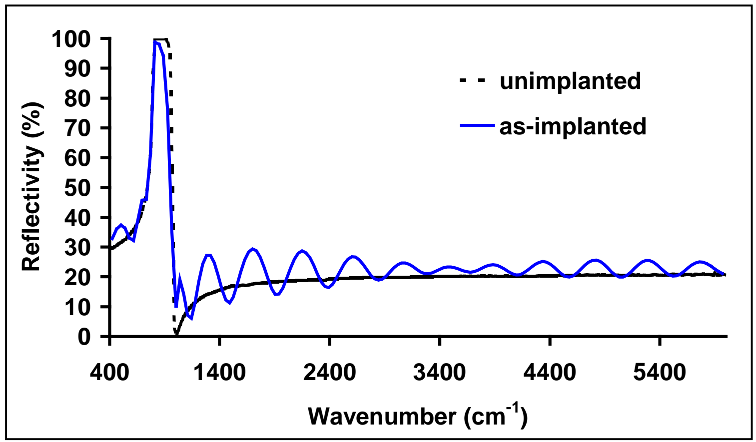

Figure 4.3: IR spectra for the unimplanted sample (dashed line) and as-implanted 4H-SiC (solid line).

4.1.2.2 Observations after annealing at 800°C for 30 min

As observed before annealing, a closer view of the damaged layer annealed at 800°C for 30 min, Fig.4.4, shows three different regions, labelled also A, B and C. In the B region, no TEM change is observed after annealing. As seen above, this central region is still amorphous and can be divided into two parts: B_1 where numerous small bubbles are still present and B_2 a region free of bubbles (see Fig.4.5). Concerning the A and C regions, however, we note that their widths and interface appearances have changed. The A and C layers expand respectively over 300 and 65 nm leading to a 765 nm damaged layer. It seems that all the interfaces are relatively sharper and that the size and density of residual defects in both these outside layers are greater than in the as-implanted sample, Fig.4.1. Numerous small bubbles are still present in the C region for instance as indicated by an arrow on Fig.4.5. A micro-diffraction pattern show that the A and C regions are single crystalline SiC.

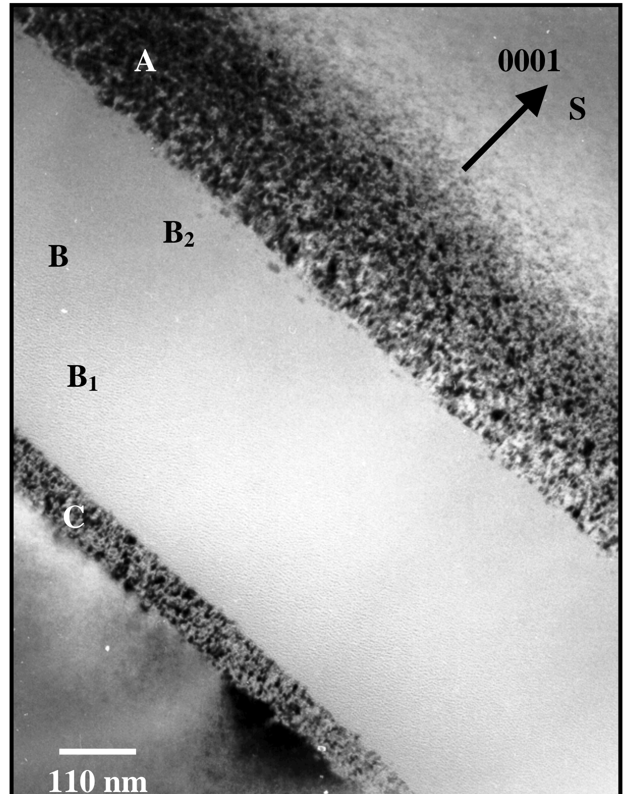

Figure 4.4: Cross sectional TEM image of 4H-SiC subjected to room temperature helium implantation (1.6 MeV, $1x10^{17}$ cm^{-2}) and annealing (800°C , 30 min).

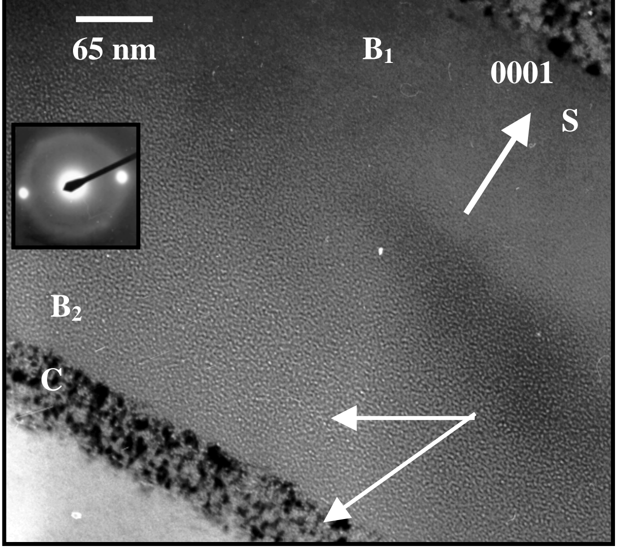

Figure 4.5: Closer view of the damaged band (B1 and C regions) for the visualization of the bubbles (1.6 MeV, $1x10^{17}$ cm^{-2}, 800°C 30min). In the inset, the diffraction pattern shows a halo corresponding to the amorphous state (B1) and diffraction spots due to the crystalline region (C).

Figs.4.6 show a set of HRTEM images taken outside the damage region (Fig.4.6a) and next to the a/c interface between the B and A regions (Fig.4.6b) and between the B and C regions (Fig.4.6c). In the region located in front of the buried layer, Fig.4.6a, we observe a periodicity of straight fringes of about 1.005 nm corresponding to the lattice constant of 4H-SiC along the [0001] direction, as expected. Near the a/c interface the fringes become wavy. In Fig.4.6b, we see that the transition of amorphous (B) to crystalline SiC (A) takes place over 30 nm since small islands of crystalline SiC are visible up to this distance. Numerous stacking faults are present in these crystalline regions. The C region mainly consists of defects such as stacking faults perpendicular to the [0001] direction, Fig.4.6c.

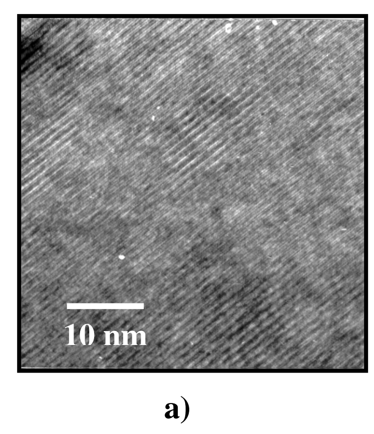

a)

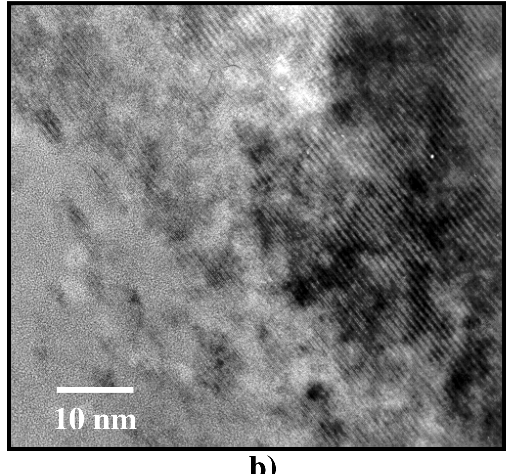

b)

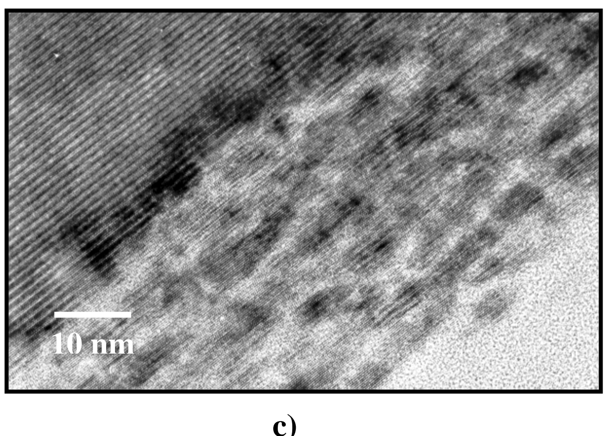

c)

Figure 4.6: Set of High Resolution TEM images taken **(a)** outside the damage region, **(b)** next to the a/c interface in the B1 region (upper part), **(c)** next to the a/c interface in the C region (lower part).

The effect of the 800°C-30 min annealing on the X-ray diffraction curve is shown on Fig.4.7. The perturbed diffraction peak towards the low angle side becomes, after annealing, a wide plateau that corresponds to dilatations of $\Delta c/c$ extending from 3.10^{-3} to $6.5\ 10^{-3}$. After annealing, the FTIR spectrum of the sample still exhibits an interference pattern with few modifications in comparison with the as-implanted sample. These modifications are ascribed to the weak widening of the buried layer as observed by TEM.

Figure 4.7: X-ray (0008) Bragg reflection for the implanted 4H-SiC (solid line) and annealed 800°C-30 min (dotted line).

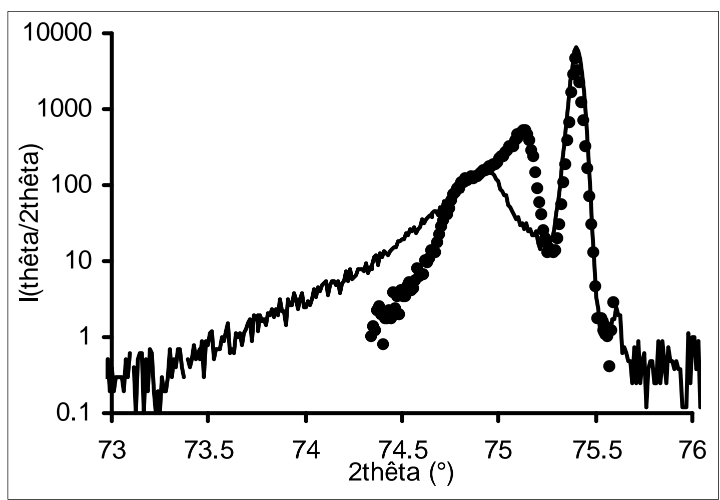

These observations are consistent with previous studies [Ishimaru *et al.* 1997] where only a small recovery of the damaged layer is observed after a 800°C 30 min anneal performed on a 6H-SiC sample implanted with 8 MeV Si^{3+} ions at a dose of $1x10^{17}$ cm^{-2}.

4.1.2.3 Annealing at 1500°C for 30 min

Fig.4.8 shows a cross sectional TEM image after a 1500°C anneal for 30 min. The buried layer width is now reduced to 400 nm. A low density of small defects is still observed on both sides. These defects extend up to the surface but to only few hundred nm into the bulk. The magnified view in Fig.4.9 shows that the buried layer contains bubbles and can be divided in three different regions noted a1, b1 and c1. In the central region b1 of 150 nm width, columns of black contrast slightly inclined from the substrate [0001] are observed, Fig.4.10. In the a1 and c1 parts of 150 and 100 nm width respectively, columns of black contrast appear perpendicular to the [0001] direction. A selected area diffraction pattern, see Fig.4.11, does not present any halo pattern showing the complete recrystallization of the amorphous layer during this 1500°C anneal.

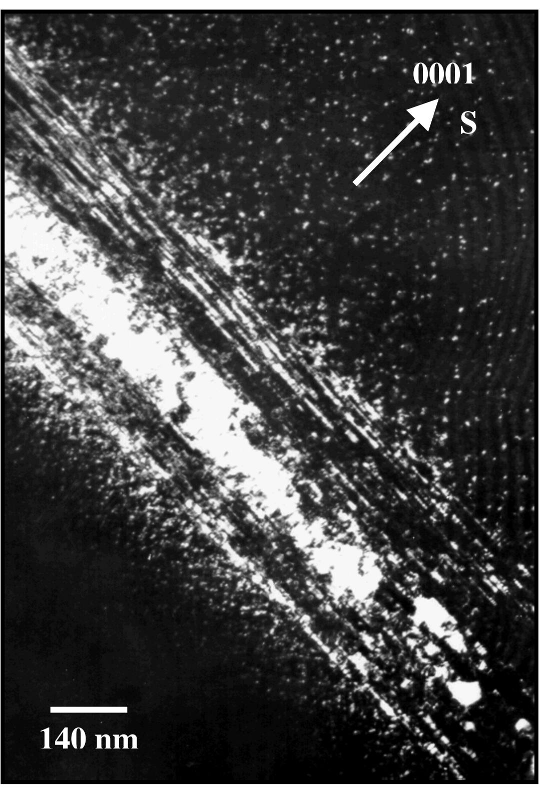

Figure 4.8: A dark-field image of the 1500°C annealed sample (30 min) showing the damaged band.

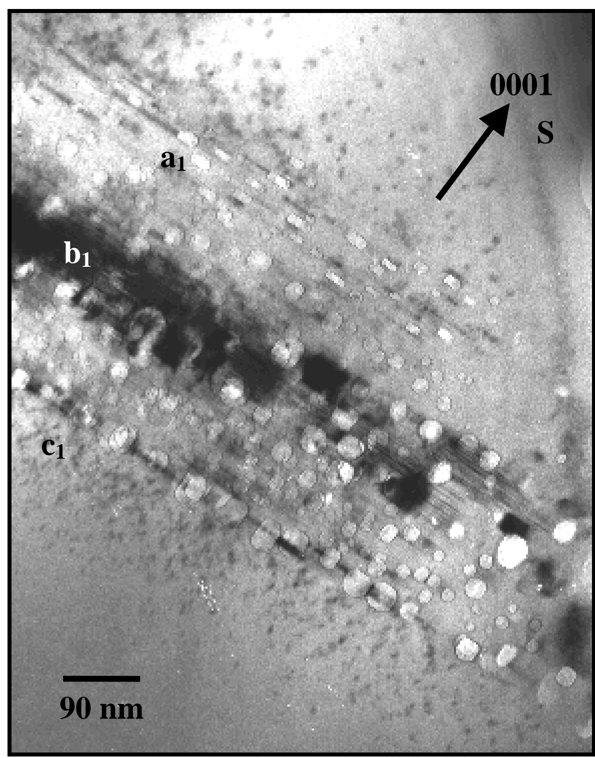

Figure 4.9: A bright field image in under-focus condition of the 1500°C annealed sample (30 min). Visualization of the bubbles.

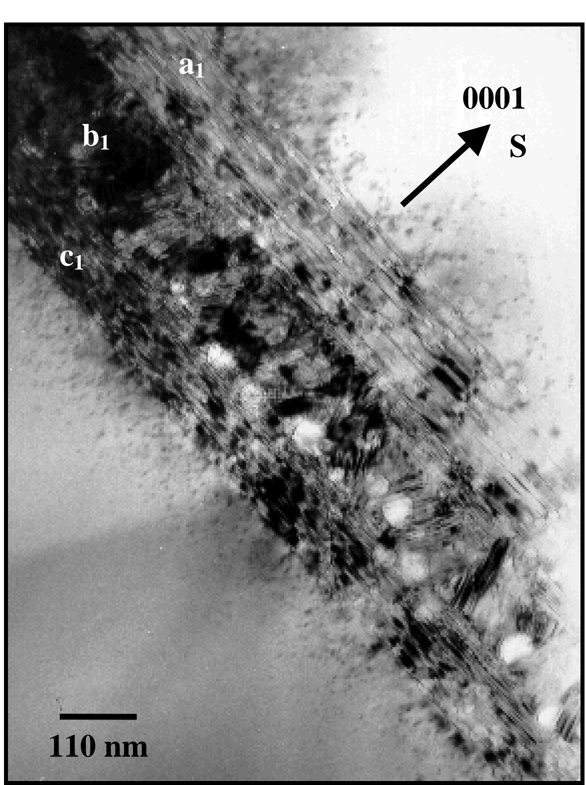

Figure 4.10: Bright field image of the recrystallization layer after the implantation and the 1500°C annealing.

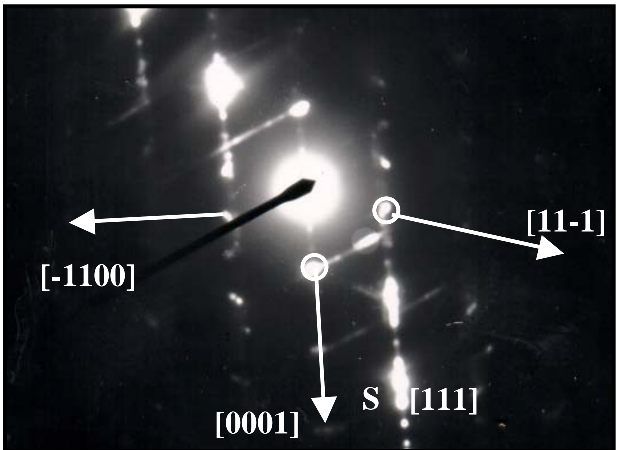

Figure 4.11: Diffraction pattern of the damaged band. As seen the (0001) 4H-SiC correspond to the [111] 3C-SiC.

The $(\bar{1}10)$ pattern of 3C-SiC is observed as well as the lattice spots due to the 4H-SiC. A circle marks the 111 and the equivalent reflections. The [111] direction of 3C-SiC coincides with the [0001] direction of 4H-SiC and the other $[11\bar{1}]$ with the $[\bar{1}102]$. This clearly shows that the 3C-SiC has grown epitaxially on the 4H-SiC. Diffuse streaks are also observed on the diffraction pattern in Fig.4.11 and are attributed to the presence of stacking faults as observed

in Fig.4.10 for example. The epitaxial regrowth initiates from the a/c interfaces leading to the formation of the a1 and c1 regions and is followed by columnar growth of 4H-SiC and epitaxial growth of 3C-SiC leading to the formation of the b1 region. The mechanism of this polytypism transition during annealing is not yet understood. Similar behavior has been observed in MeV-ion implanted 6H-SiC followed by a 1000°C annealing [Ishimaru *et al.* 1997]. The atomic configuration for the recrystallization during annealing is proposed in Fig.4.12. In this configuration the $(\bar{1}102)$ plane of layer-by-layer 4H-SiC coincides with the (0001) plane of columnar 4H-SiC. The bond mismatches existing at the interface between the columnar and layered regions may lead to the formation of numerous stacking faults as observed. These latter are known to have a low energy of formation in SiC, $\gamma_{4H} = 14.7 \pm 2.5$ mJm^{-2} [Hong *et al.* 2000].

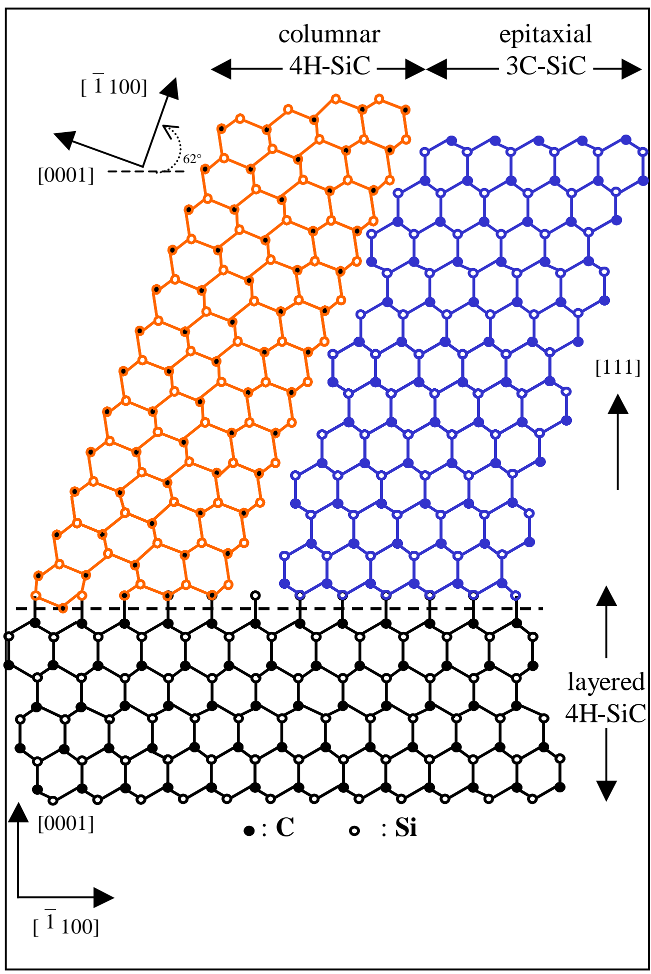

Figure 4.12: Model for the atomic configuration of the recrystallization observed after the 1500°C anneal.

It is likely that upon annealing at 1500°C the He outgases from the sample. Although no helium release experiment has been reported yet in SiC, we will assume in the following that bubbles are empty of He and thus will be referred to as cavities or voids.
Bright field images in the underfocus condition of Fig.4.9 shows numerous cavities distributed all over the buried layer, contrary to what is mentioned above after the 800°C anneal (Fig.4.4) where bubbles are present only in a part of the B layer. Obviously, the 1500°C anneal also enlarges the cavities. Their size, shape and density are found to depend on their position in the layer. In the center of the band, the cavities have a rather circular shape with a size ranging from 15 to 50 nm or are faceted with facets along the $[\bar{1}100]$ and [0001] directions. Towards the implanted surface, they become smaller and in the last 150 nm they appear cylindrical in the $[\bar{1}100]$ direction. The density does not seem to vary ($\approx 10^{16}$ cm^{-3}). In the a1 region, no cavities are observed directly after implantation and even after the 800°C anneal. Below the center of the band, in the c1 region, the cavity density increases roughly by a factor 2 whereas the size decreases. They are circular or slightly elongated with a diameter in the range 5-25 nm. This cavity band ends with a row of large faceted cavities (≈ 30 nm). We do not observe dislocation loops contrary to what was expected from a previous study [Grimaldi *et al.* 1997]. The authors mention that cavities are always accompanied by faulted dislocation loops of interstitial type. The doses used, however, are smaller than the one implanted in this study.

In the X-ray diffraction spectrum, the satellite diffraction peak observed before annealing has disappeared. The IR reflectivity spectrum exhibits an interference pattern as seen before, which is consistent with TEM observations. Indeed, no great variation of the width of the perturbed band that corresponds to the optical interface located at about 3.6 μm from the surface is observed. These observations show an almost complete structural recovery of the initially perturbed crystalline regions of the as-implanted sample.

4.1.2.4 In situ annealing

An in situ annealing experiment has been performed in the JEOL 200CX. The starting temperature for observations was 350°C and the final was 820°C. During the in-situ annealing, no clearly visible change in the bubble size has been seen in the amorphous zone (B). Fig.4.13 shows a bright field image obtained at the end of the annealing experiment. The buried layer can also be divided in three different regions A, B and C. The amorphous central

region B, 280 nm thick, is a continuous layer of small cavities whereas the two outside regions, A and C, contain small defects. For oneself we note that the A region shows a higher density of defects near the a/c interface. When comparing with the 800°C annealing (§ 4.1.1.2) we note that this region corresponds to the amorphous region (B2); i.e. the one with no bubbles. This suggests that the electron beam induces the epitaxial regrowth of this layer. No growth occurs on the deeper a/c interface showing that the bubbles stabilize the amorphous layer. The recovery of defects under the ion beam is clearly shown in the deeper band C since no dark contrast spot is present near the edge of the sample.

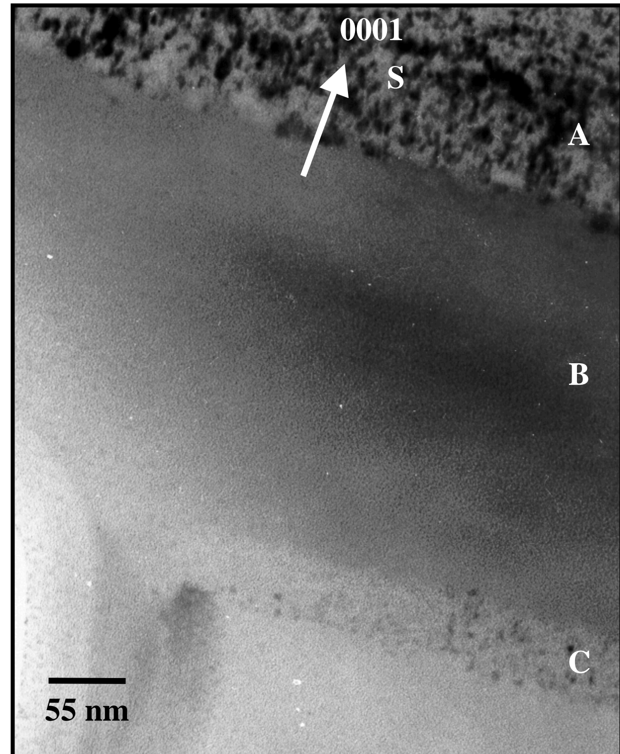

Figure 4.13: TEM image of the damaged zone after helium implantation and in-situ annealing up to 820°C.

4.1.3 Modelisation of the damaged structure

TEM investigations of the damage induced by 10^{17} ions/cm^2 He implantation at 1.6 MeV in 4H-SiC show that a three layer structure can be distinguished: two outside layers which mainly consist of point defect clusters and an amorphous layer in the middle. Similar results have been reported for heavier ions [Ishimaru *et al.* 1999, Pacaud *et al.* 1996]. Even after high temperature annealing, a three-layer structure is still observed.

4.1.3.1 Derivation

To model our observations, i.e. the damaged structure in layers, we consider the transport of atoms within the collision area and their relocation under ion bombardment. The mathematical formalism of mass transport in two element solids was developed and applied in the case of metals (Sigmund approach). It is based on the solutions of the non-linear integro-differential mixing equation [Sigmund *et al.* 1993, Sckerl *et al.* 1998]. In this study we consider a simplified calculation by introducing the relocation function $w_i^{(K,L)}$ that defines the frequency probability of relocation of *i*-atoms from the *K*-th to the *L*-th monolayer; the solid being divided into layers of equal thickness h_0. Thus, the time variation of concentration for *i*-th type atoms in the *K*-th monolayer is described by:

$$\frac{dc_i^{(K)}}{dt} = \sum_{L=1}^{\infty} w_i^{(L,K)} c_i^{(L)} - \sum_{L=-\infty}^{\infty} w_i^{(K,L)} c_i^{(K)} \tag{4.3}$$

with $\frac{d}{dt}\left(\sum c_i^{(K)}\right) \neq 0$

The first term of Eq.(4.3) gives the flux of *i*-atoms arriving into the *K*-th monolayer and the second term describes the flux of *i*-atoms leaving the *K*-th monolayer (the negative values of *L* including zero give the possibility of *i*-atoms to go out of the solid). Since the relocated atoms are forming Frenkel pairs, and because of the non-homogeneous distribution of energy losses, atoms are transferred to the periphery of the activated region. This results an excess of vacancies in the R_p region ($\sum c_i^{(K)} < 1$) and an excess of interstitials in the periphery ($\sum c_i^{(K)} >$ 1). The flux of atoms driven out of the activated area is given by:

$$F_i = -\frac{\partial c_i}{\partial t} = -\frac{\partial}{\partial x}\left(D_i \frac{\partial c_i}{\partial x}\right) \tag{4.4}$$

where D_i is the diffusion coefficient of *i*-atoms that can be written in the form

$$D_i = \frac{1}{6} l_i^2 w_i(x) \tag{4.5}$$

$l_i = h_0$ being the jump distance between neighboring monolayers and $w_i(x)$ the displacement frequency which is supposed to be proportional to the nuclear energy losses $(dE/dx)_n$ given by SRIM calculations. Thus,

$$D_i \ \alpha \ (\frac{dE}{dx})_n \tag{4.6}$$

From Eq. (4.6) different areas in the SiC damaged zones can be distinguished. When the displacement rate is maximum (around R_p) the flux of redistributed atoms approaches zero $\frac{\partial}{\partial x}(\frac{dE}{dx})_n \approx 0$, i.e. fluxes in and out are compensated. This zone can thus be considered as an area highly enriched by vacancies and interstitials. In the areas where $\frac{\partial}{\partial x}(\frac{dE}{dx})_n$ is maximum ($R_p \pm \Delta R_p$) atomic motion takes place, i.e. the flux of relocated atoms approaches maximum value. From the viewpoint of point defects the region above the region of maximum displacement rate is enriched in vacancies while the region behind is enriched by interstitials and is not highly affected by displacements. Thus, differences are expected after subsequent annealing.

In this work, the relocation function $w_i^{(K,L)}$ is defined as

$$w_i^{(L,K)} = w_i^0 \exp[-\frac{1}{2}\left(\frac{h_0(K-1)-R_p}{\Delta R_p}\right)^2 - \frac{1}{2}\left(h_0\frac{|K-L|}{l_i}\right)^2] \tag{4.7}$$

where w_i^0 is a constant proportional to the flux of incident ions and dependent on the energy of ions. As seen from Eq.(4.7), $w_i^{(L,K)}$ results in the product of the probability of relocation between K and L monolayers with the displacement rate, which is proportional to the nuclear energy losses. $l_i = h_0$ is the jump distance between neighboring monolayer.

4.1.3.2 Simulations and comparison with experimental results

The variations of concentration for the *i*-th atoms are shown in Fig.4.14 as a function of depth with regards to R_p for two different values of the diffusion coefficient D. The curves are normalized with $\sum_{i=1}^{n} c_i = 1$ for an unperturbed monolayer. To take into account the skewness of

the nuclear energy loss profile, two straggling values ΔR_{p1} (above R_p) and ΔR_{p2} (behind R_p) are distinguished according to the SRIM calculations. Since the displacement rate of Si (i=1) and C (i=2) atoms depends on their threshold displacement energy in the crystal sites, two different displacement rates w_i^0 evaluated from SRIM calculations are taken into account

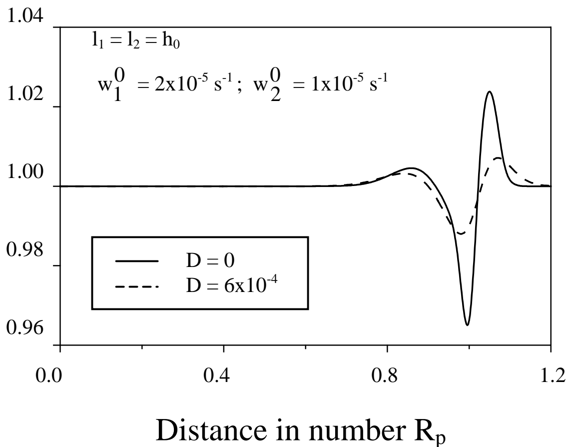

Figure 4.14: The concentration profiles of atoms after implantation calculated for two values of the diffusion coefficient D (before annealing: D=0, after high temperature annealing: D= 6x10^{-4}). ΔR_{p1}=0.4µm and ΔR_{p2}=0.1µm are taken from SRIM calculations and reflect the inhomogeneous displacement rate of atoms. l_i is the characteristic relocation length of i-type atoms and W_i^0 is the displacement rate depending on the threshold displacement energy (i=1 for Si atoms and i=2 for C atoms).

although that leads to only small modifications to the curves. Fig.4.14 shows that three different regions can be distinguished and that transport of atoms exists from the highly perturbed area to the periphery. The central region shows an excess of vacancies while an excess of interstitials appears on both sides. As the temperature increases, the irradiated system tends to relax via atomic movement and differences in concentration become less pronounced. It is difficult to compare the width of the regions with those obtained from TEM results since the TEM resolution does not allow us to detect point defects. However, the curves predict two outside layers of different widths and different concentrations of point defects in agreement to what is observed by TEM. Moreover, the highly damaged zone with excess of vacancies corresponds to the amorphous zone (labelled B) including the bubbles. The difference is also manifest after annealing (1500°C) where the periphery regions recrystallize epitaxially whereas the central one consists of differently oriented crystallites with equiaxed structure (Fig.4.9). Moreover, when comparing to TEM results, we see that large circular cavities are formed in the area of R_p where the flux of atoms is nearly zero.

Our calculations predict a ballistic displacement of atoms. SiC being a two-component target, ballistic mobilities of Si and C atoms differ and redistribution of the two components under irradiation is expected, leading to the formation of new phases, such as graphite for example. This has already been reported in oxygen-ion-implanted silicon where compositional fluctuations in the damaged zone have been observed. Carbon atoms have been found to accumulate in the periphery of the buried amorphous zones [Barradas *et al.* 2000, Ishimaru *et al.* 2000]. Composition changes have been also reported in Ar-bombarded SiC [Miotello *et al.* 1993]. This will be the next step of our calculations.

4.1.4 Summary

Implantation at room temperature of high dose helium ions into SiC leads to the formation of small bubbles. However, the critical dose for forming bubbles exceeds the dose for amorphization and a multilayer structure is observed; an amorphous layer surrounded by crystalline zones of point defects. Only a slight recovery of the damaged layer is observed after a 800°C-30 min annealing. No change in bubble morphology is observed. The in-situ annealing shows that the electron beam induces the epitaxial regrowth of the amorphous layer only from the upper interface in the region free of bubbles. The presence of bubbles in the other amorphous region prevents the electron beam induced recrystallisation. At higher temperature (1500°C) recrystallization take place resulting in a complex structure with inclusions of epitaxial 3C-SiC and columnar growth of 4H-SiC. The 1500°C anneal relaxes the structure and enlarges the cavities. However, their size, shape and density are found to be different depending on their position in the damaged band.

The multilayered structure has been analysed using a mathematical formalism considering the atomic relocation between monolayers. It is shown that atomic displacements initiate mass-transport. By comparing the calculated profiles with the TEM results we note that the circular bubbles are formed where fluxes of atoms initiated by displacement processes are negligible whereas smaller bubbles (or voids) and epitaxial recrystallization occur in the region of excess interstitials where the flux is maximum.

References

[Barradas *et al.* 2000] N.P. Barradas, C. Jeynes and S.M. Jackson, *Nucl. Inst. and Meth. B* **136/138**, 1168 (1998).

[Capano *et al.* 1997] M.A. Capano, R.J. Trew, *MRS Bull* **19-20**, 19 (1997).

[Chen *et al.* 2000] J. Chen, P. Jung, H. Trinkaus, *Phys. Rev. B* **61,** 12923 (2000).

[Declémy *et al.* 2002] A. Declémy, E. Oliviero, M.F. Beaufort, J.F. Barbot, M.L. David, C. Blanchard, Y. Tessier, E. Ntsoenzok, *Nucl. Inst. and Meth. B* **186**, 318 (2002).

[Frangis *et al.* 1996] N. Frangis, J. Van Landuyt, M.G. Grimaldi, L. Calcagno, *Nucl. Inst. and Meth. B* **120**, 186 (1996).

[Follstaedt *et al.* 1996] D.M. Follstaedt, S.M. Myers, G.A. Petersen, J.W. Medernach, *J. Electron. Mater.* **25**, 157 (1996).

[Grimaldi *et al.* 1997] M.G. Grimaldi, L. Calcagno, P. Musumeci, N. Frangis, J. Van Landuyt, *J. Appl. Phys.* **81**, 7181 (1997).

[Grisolia *et al.* 2000] J. Grisolia, F. Cristiano, B. De Mauduit, G. Ben Assayag, F. Letertre, B. Aspar, L. Di Cioccio, A. Claverie, *J. Appl. Phys.* **87,** 8415 (2000).

[Harris *et al.* 1995] G. L. Harris, *Properties of silicon carbide* (INSPEC, London) (1995).

[Heera *et al.* 1995] V. Heera, J. Stoemenos, R. Kögler, W. Skorupa, *J. Appl. Phys.* **77**, 2999 (1995).

[Hong *et al.* 2000] M.H. Hong, A.V. Samant, P. Pirouz, *Phil. Mag. A* **80**, 919 (2000).

[Ishimaru *et al.* 1997] M. Ishimaru, S. Harada, T. Motooka, T. Nakata, T. Yoneda, M. Inoue, *Nucl. Inst. and Meth. B* **127/128**, 195 (1997).

[Ishimaru *et al.* 1999] M. Ishimaru, R. M. Dickerson, K.E. Sickafus, *Appl. Phys. Lett* **75,** 352 (1999).

[Ishimaru *et al.* 2000] M. Ishimaru, R. M. Dickerson, K.E. Sickafus, *J. Electrochemi. Soc.* **147,** 1979 (2000).

[McHargue *et al.* 1993] C.J. McHargue, and J.M. William, *Nucl. Instrum. Methods Phys. Res. B* **80/81**, 889 (1993).

[Miotello *et al.* 1993] A. Miotello, L. Calliari, R. Kelly, N. Laidani, M. Bonelli, L. Guzman, *Nucl. Inst. and Meth. B* **80/81**, 931 (1993).

[Oliviero *et al.* 2000] E. Oliviero, M.F. Beaufort, A. Declemy, G. Blondiaux, E. Nstoenzok, J.F. Barbot, MRS Boston (2000).

[Pacaud *et al.* 1996] Y. Pacaud, W. Skorupa, A. Perez-Rodriguez, G. Brauer, J. Stoemenos, R.C. Barklie, *Nucl. Inst. and Meth. B* **112**, 321 (1996).

[Raineri *et al.* 1995] V. Raineri, P.G. Fallica, G. Percolla, A. Battaglia, M. Barbagallo, S.U. Campisano, *J. Appl. Phys.* **78**, 3727 (1995).

[Sckerl *et al.* 1998] M.W. Sckerl, N.Q. Lam, P. Sigmund, *Nucl. Inst. and Meth. B* **140**, 75 (1998).

[Sigmund *et al.* 1993] P. Sigmund, A. Oliva, *Nucl. Inst. and Meth. B* **82**, 269 (1993).

[Spitznagel *et al.* 1986] J.A. Spitznagel, S. Wood, W.J. Choyke, N.J. Doyle, J. Bradshaw, S.G. Fishman, *Nucl. Instrum. Methods Phys. Res. B* **16**, 237 (1986).

[Ziegler *et al.* 1985] J.F. Ziegler, J.P. Biersack, U. Littmark, *The Stopping and Range of Ions in Solids* (Pergamon Press, New York, 1985).

4.2 He desorption from low dose He implanted SiC: a study of bubble precursors

4.2.1 Experimental procedure

6H-SiC samples produced by "Electroschmelzwerk Kempten", *n*-type 4H-SiC single crystals with (0001) surface orientation produced by CREE and polycrystalline SiC grown by CVD were used in this study (see Table.4.1). The samples were in-situ implanted (see appendix 1) with helium ions at doses ranging from $1x10^{13}$ cm^{-2} to $1x10^{15}$ cm^{-2} with energies varying from 100 eV to 3 keV. The mean depth of the implanted helium atoms, calculated with SRIM simulation [Ziegler *et al.* 1985], varied from 1.7 nm to 28 nm, with corresponding straggling of 1 nm and 13.7 nm, for 100 eV and 3 keV helium ions, respectively. The implantation dose is determined by integration of the measured target current. In fact this overestimates the implanted dose because secondary electrons are not suppressed in the THDS apparatus, i.e. there is no Faraday cup. So to get rid of the contribution of secondary electrons, the real implanted dose is obtained by reducing the measured dose of 20%.

Sample	Polytype	Type	Orientation	Mode of growth	Origin
SiC 1	4H	n	0001	epitaxy	CREE
SiC 2	6H	-	-	-	Electroschmelzwerk Kempten
SiC 3	Poly	-	-	CVD	-

Table 4.1: Different SiC samples used in the study.

4.2.2 6H-SiC

4.2.2.1 Dose variation

The evolution of desorption spectra with the dose has been measured for different energies ranging from 100 eV to 3 keV (cf. appendix.2). The lowest dose studied was $1x10^{13}$ cm^{-2} due to the detection limit of the apparatus and the highest was $1x10^{15}$ cm^{-2} which is lower than the minimum helium concentration to form bubbles in SiC. In silicon, the critical implantation dose below which bubbles cannot be formed has been estimated to be $1x10^{16}$ cm^{-2} [Myers *et al.* 1993, Fedorov *et al.* 1998, Raineri *et al.* 2000].

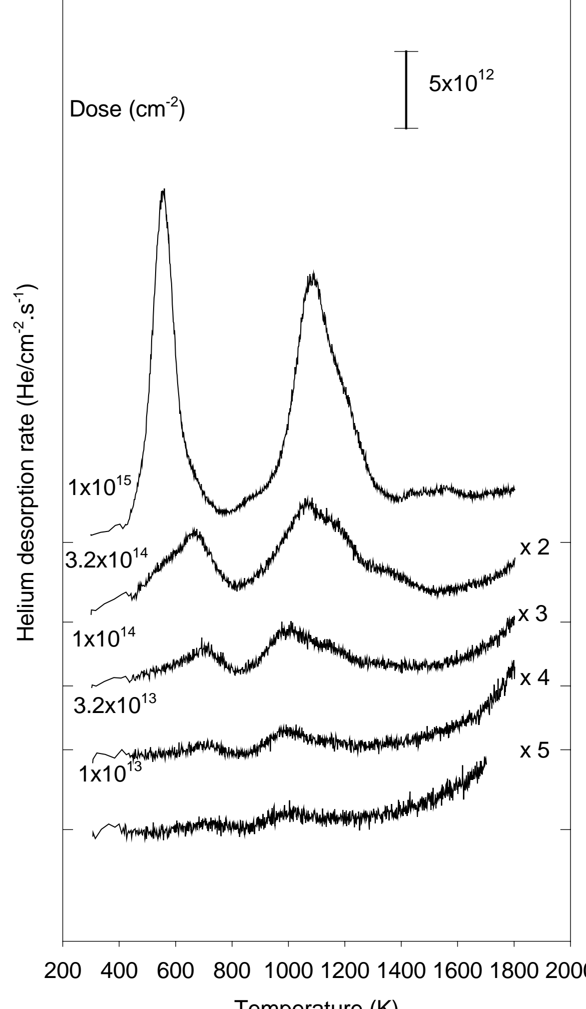

Figure 4.15: Desorption spectra obtained for 6H-SiC implanted with 1 keV He ions at the indicated doses.

Fig.4.15 shows the desorption spectra for a 1 keV helium implant. As seen, two broad desorption peaks are clearly distinguished, at temperatures of about 600 and 1200 K. Typical first-order desorption peaks, describing the release of a single helium from a trapping site, have FWHM values of 0.07 T_m (peak temperature), i.e. 40 K and 80 K for peaks at 600 and 1200 K respectively. These peaks are thus made up of at least two desorption peaks that can

not be resolved without any fitting procedure. This is clearly shown for the $3.2x10^{14}$ cm^{-2} dose where shoulder peaks arise toward the low temperature side for the first group (600 K) and toward the high temperature side for the second (1200 K). With increasing dose the amplitude of these shoulder peaks becomes dominant inducing a shift of the maximum temperature of the group. From now on we will consider them as groups of peaks. In Fig.4.16, the values of the difference in temperature of maximum release between the two limiting doses ($1x10^{13}$ and $1x10^{15}$) are plotted for each group as function of the implantation energy. It can be observed that the shift in temperature is maximum for implantation energy of 1.5 keV for the first group while for the second group maximum shift occurs at 500 eV.

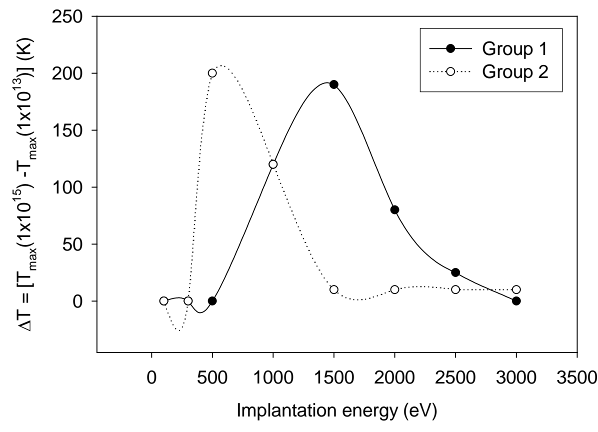

Figure 4.16: Evolution of the temperature difference between the two limit doses with implantation energy.

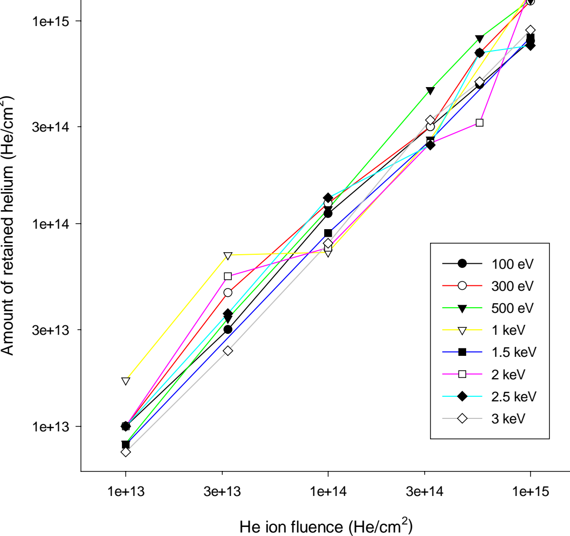

Figure 4.17: Amount of retained helium versus the He ion fluence for 6H-SiC implanted at different energies.

The amount of retained helium in the sample, Fig.4.17, is obtained by integration of the He desorption rate. The amount of helium increases in nearly all cases linearly with increasing dose and the ratio retained/implanted is close to 1 for all doses studied. Helium saturation has thus not been reached. This is in agreement with previous results obtained in SiC converted graphite where a saturation amount of $4.2x10^{17}$ $He.cm^{-2}$ was observed [Yamauchi *et al.* 1998]. In general, the retained fraction is expected to be some tens % lower

than unity due to the backscattering of some of the incident ions. The backscattered fraction is found to be close to 10% for a 1 keV implant. This value is lower than the sensitivity of the measurements.

4.2.2.2 Energy variation

The evolution of the thermal desorption spectra for increasing energy is shown in Figs.4.18a and b at doses of $1x10^{14}$ cm^{-2} and $1x10^{15}$ cm^{-2}, respectively. In both cases, the first group is

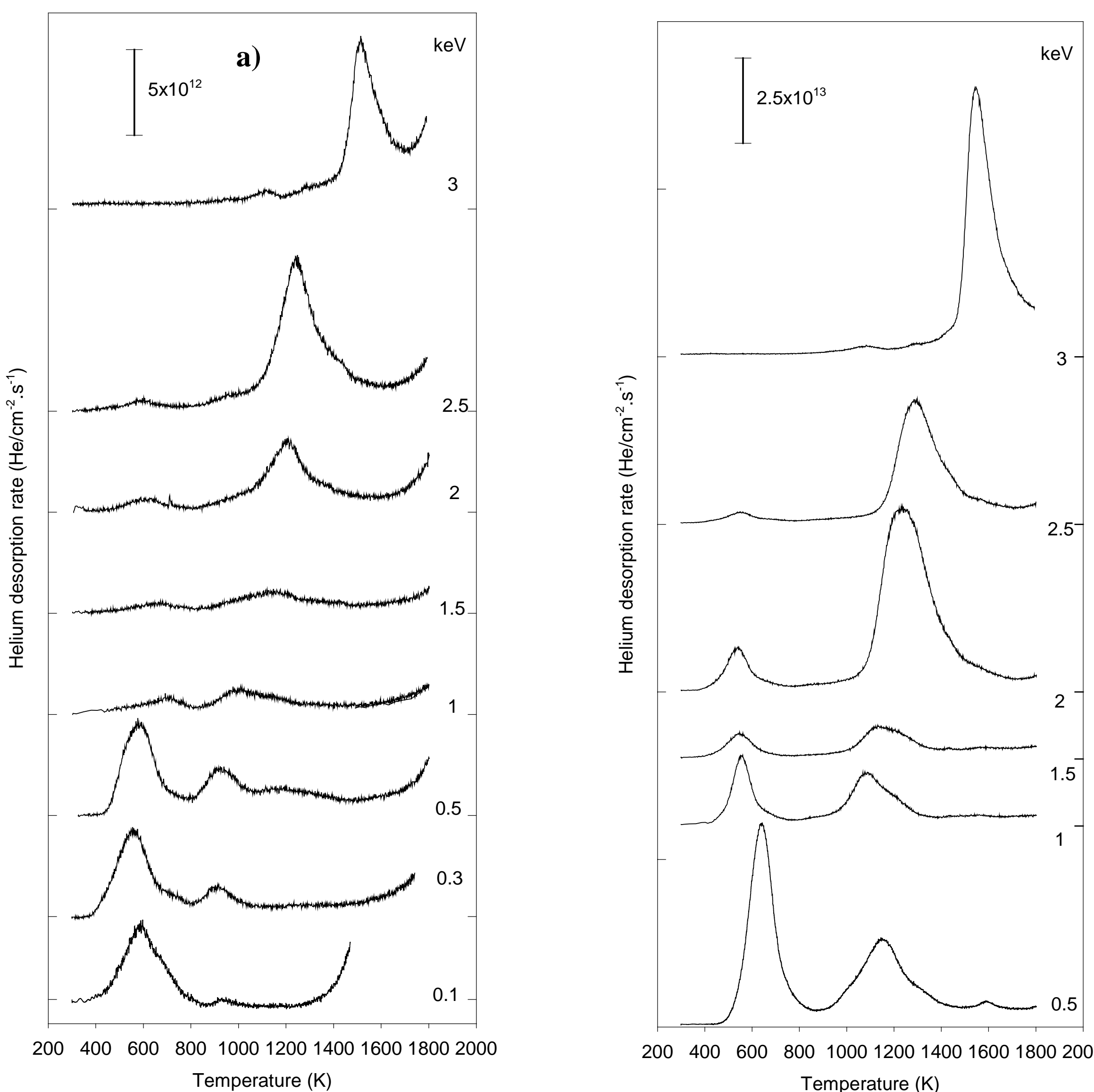

Figure 4.18: Evolution of desorption spectra obtained for 6H-SiC implanted with He at different energies for a dose of $1x10^{14}$ cm^{-2} **(a)** and of $1x10^{15}$ cm^{-2} **(b)**.

dominant at low incident energies while the second one becomes dominant with increasing energies. Fig.4.19 shows the relative population for the two groups derived from figures 4.18a

and b taking into account the sensitivity of the apparatus for each measurement. It is clearly observed that the population of helium in the high temperature group increases with increasing helium ion energy, or implantation depth, while the population in the first group decreases.

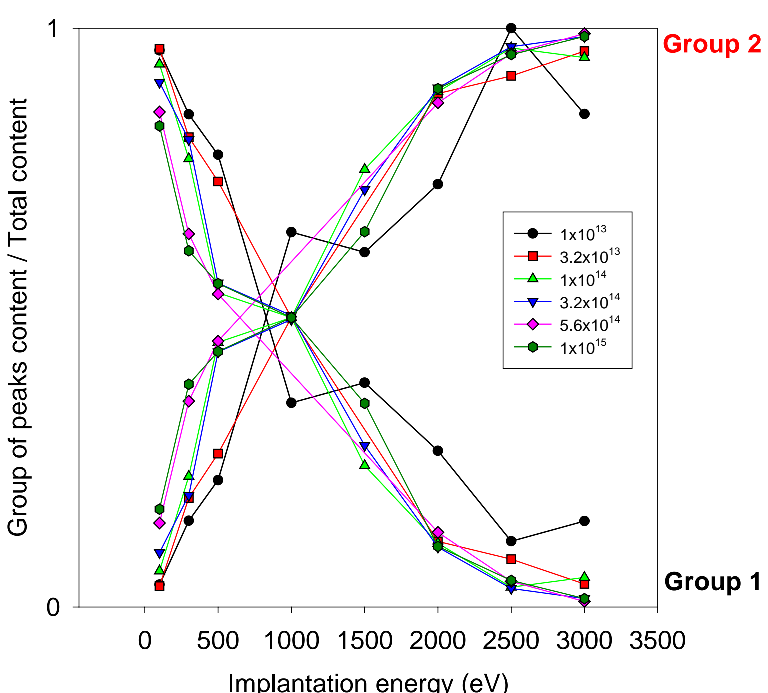

Figure 4.19: Group of peaks populations versus the implantation energy for 6H-SiC. Each set of point, with lines to guide the eye, represents one dose. Group 1 denotes the group at 600 K and group 2 the peak at 1200 K

4.2.3 4H-SiC

4.2.3.1 Conventional studies

The desorption spectra of 1 keV He implanted 4H-SiC CREE sample for doses ranging from $1x10^{13}$ cm^{-2} to $1x10^{15}$ cm^{-2} are shown in Fig.4.20. As reported above in case of irradiated 6H-SiC, Fig.4.15, two groups of peaks are observed at 600 and 1200 K. Likewise, the amount of helium increases linearly with increasing dose and the ratio retained/implanted is close to unity. However, for the same energy (1 keV), the population was found to be equivalent in both groups for the 6H-sample (Fig.4.15) while now for the 4H, the population of He in the second group of peaks is higher than in the first group whatever the dose may be.

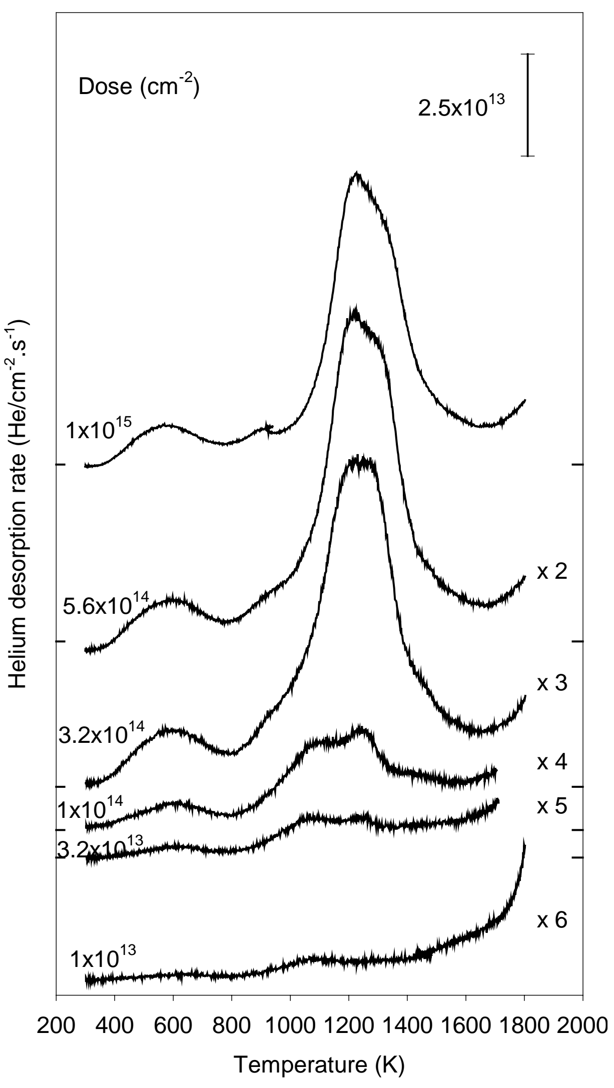

Figure 4.20: Desorption spectra obtained for 4H-SiC implanted with 1 keV He ions at the indicated doses.

4.2.3.2 High dose experiment

In Fig.4.21 an additional desorption spectrum for a dose of 1x10^{16} cm^{-2} is also plotted. The two groups are still observed with a strong background signal due to the saturation of the quadrupole. Additional helium implants and thermal desorption have been performed on this sample, after the high dose measurement. Only a group centered at 600 K is now observed as seen in Fig.4.22. This behavior is observed whatever the energies (Fig.4.23) and dose may be (Fig.4.24). This clearly shows that no recovery of defects created during the first step of experiment (implantation at a dose of 1x10^{16} cm^{-2} and helium desorption) has occurred. This has been only observed in this case, i.e. after a pre-implantation at dose of 1x10^{16} He.cm^{-2}.

Figure 4.21: Desorption spectra obtained for 4H-SiC implanted with 1 keV He ions at the indicated doses.

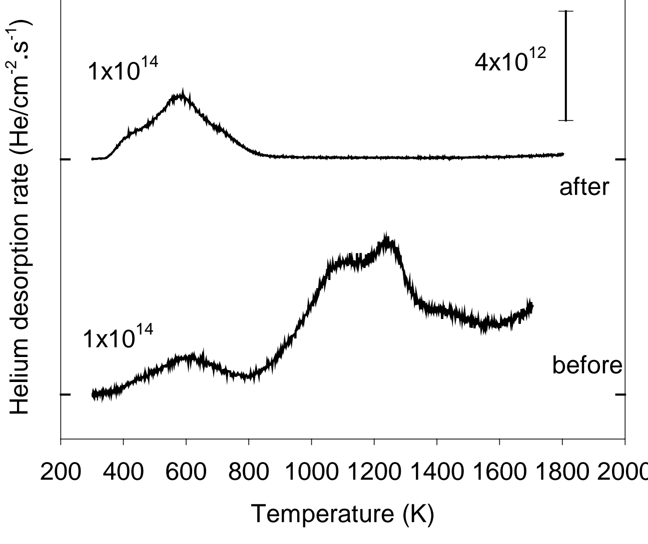

Figure 4.22: Desorption spectra obtained for 4H-SiC implanted with 1 keV He ions at $1x10^{14}$ cm^{-2} before and after the high dose experiment.

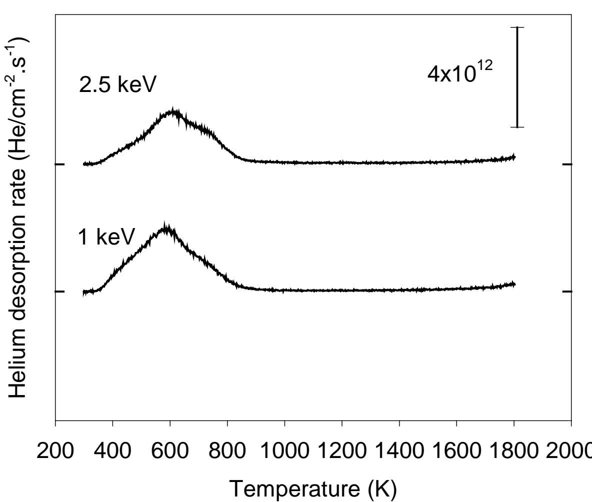

Figure 4.23: Evolution of desorption spectra obtained for 4H-SiC implanted with He at different energies for a dose of $1x10^{14}$ cm^{-2} after modification of the sample.

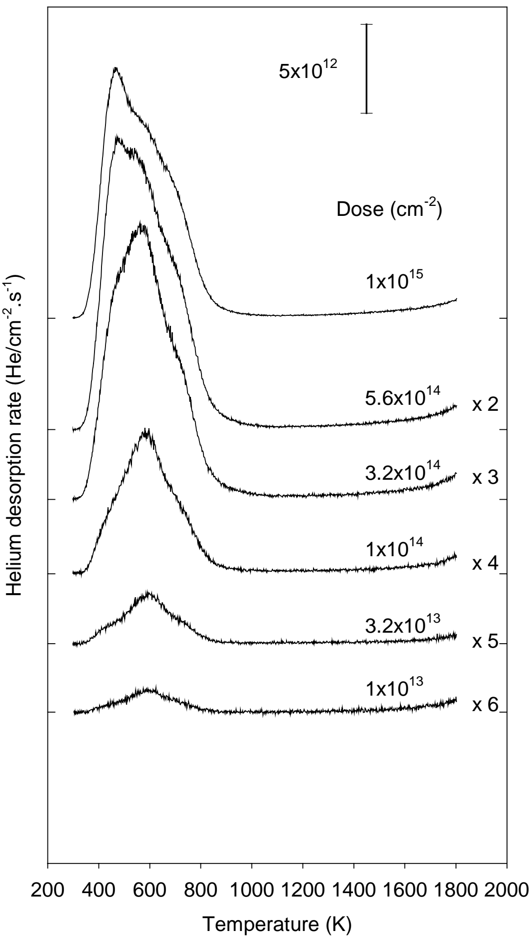

Figure 4.24: Desorption spectra obtained for 4H-SiC implanted with 1 keV He ions at the indicated doses after modification of the sample.

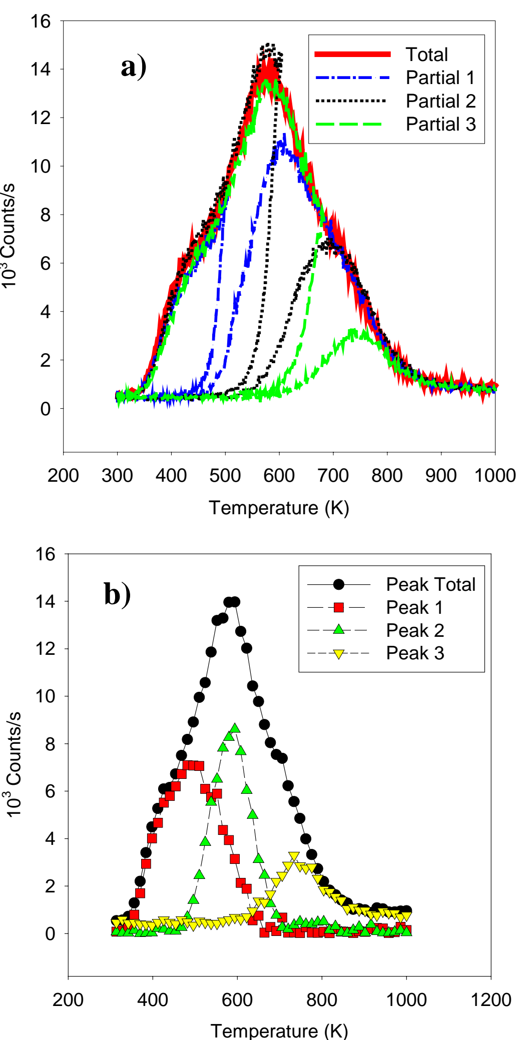

Figure 4.25: **(a)** Partial annealing desorption spectra obtained for "modified" 4H-SiC implanted with 1 keV He ions at the dose of $1x10^{14}$ cm^{-2}.
(b) interpolation of data from (a)

Partial annealing was used to study this "new" group of peaks. It consists in heating the sample up to a temperature at which not all the helium has yet desorbed, in cooling it down and in heating it up again until 1800 K (Fig.4.25a). By interpolation of the data, i.e. by subtracting, for each partial, the residual amount of helium (detected when heating up again) to the total peak, it is clearly shown in Fig.4.25b that the temperature of maximum release depends on the amount of retained helium in the sample. For a first-order desorption model describing the release from one single defect, only a reduction of the amplitude of the peak is expected. It can be assumed that the broad group of peaks is made of more than three different peaks. Indeed, the FWHM value of the three peaks is still larger than expected for a first-order desorption.

4.2.3.3 Reproducibility

Further experiments on bulk 4H-SiC implanted at doses up to $1x10^{15}$ He.cm^{-2} have shown that the first group of peaks is not always present. Indeed, in Figs.4.26 and 4.27, only the group of peaks at high temperature contributes to the desorption spectra whatever the energy or dose may be (see appendix 2). The behavior of this group is, however, similar to the one reported before (§ 4.2.1) even if it is found at slightly higher temperature (~1400 K). The presence of the first peak for doses lower than $1x10^{16}$ He.cm^{-2} seems to depend on sample and/or on sample preparation.

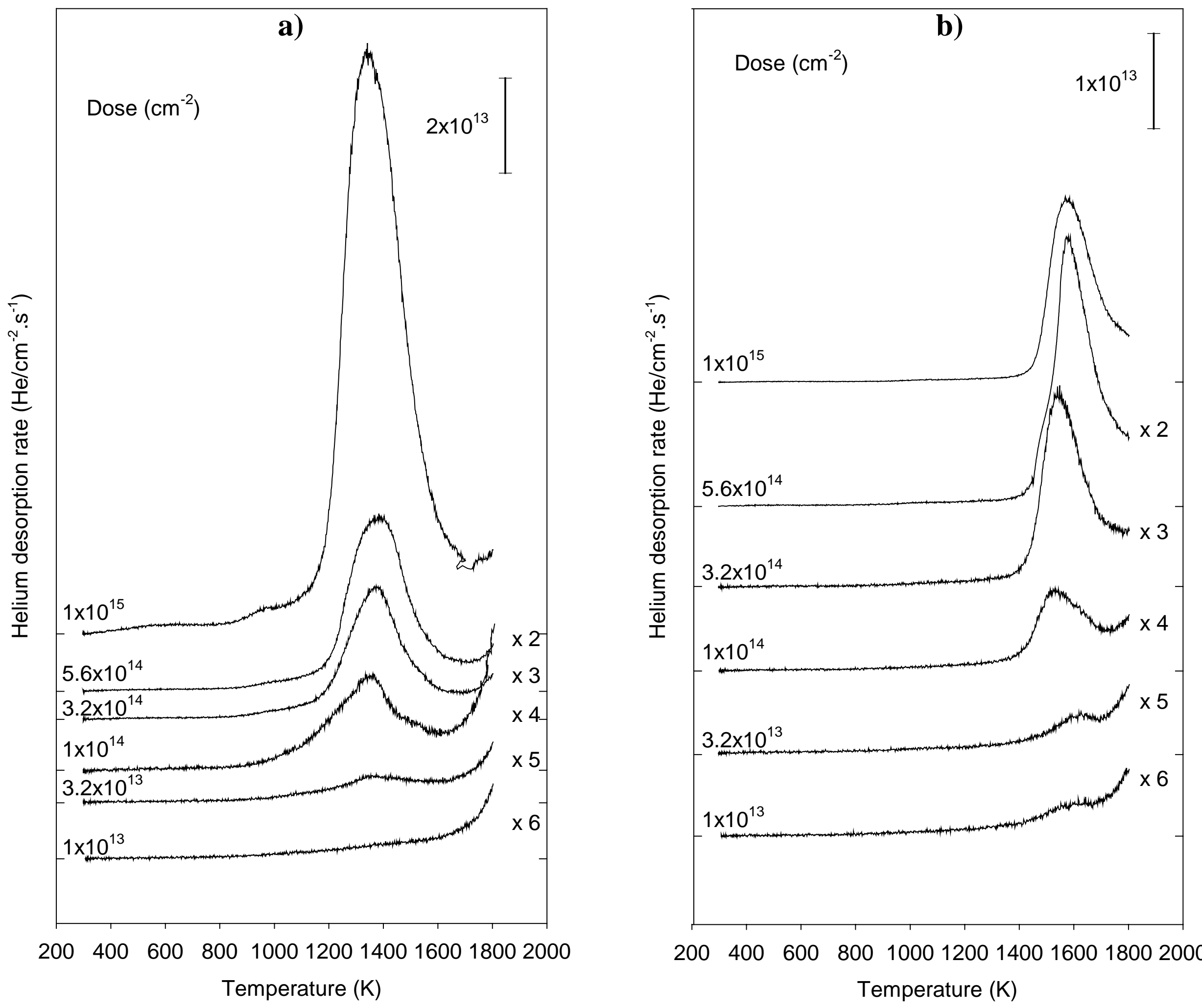

Figure 4.26: Desorption spectra obtained for 4H-SiC(2) implanted with 1 keV **(a)** and 3 keV **(b)** He ions at the indicated doses.

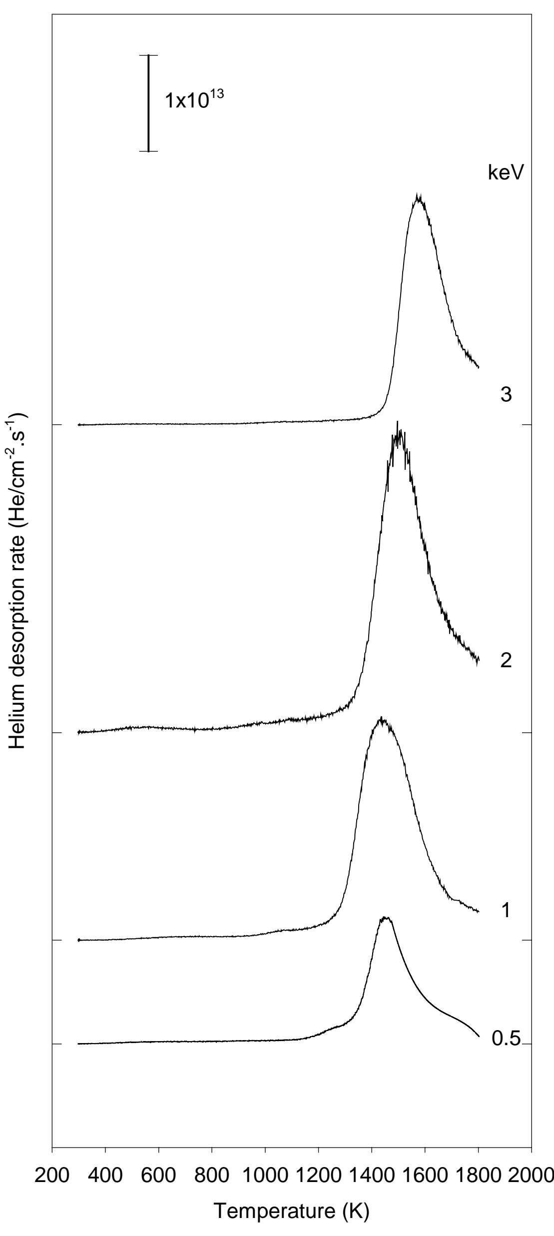

Figure 4.27: Evolution of desorption spectra obtained for 4H-SiC implanted with He at different energies for a dose of $1x10^{15}$ cm^{-2}

4.2.4 CVD SiC

The desorption results Figs.4.28-29 obtained on CVD SiC show that the same tendency observed in 6H-SiC is followed. Two groups of peaks are distinguished, whose position, population and presence evolve with implantation energy and dose. Nevertheless, the second peak is found at a lower temperature than previously reported for 6H and 4H-SiC. At an implantation energy of 500 eV release of helium is found to occur only at 600 K. On increasing the dose to a dose $3.2x10^{14}$ cm^{-2} a shoulder peak arises towards the higher

temperature side (800 K). For a 1 keV implantation, two groups of peaks are observed at 600 K and at 900 K. The population of helium in the two groups of peaks increases with increasing dose. But for low doses (up to $1x10^{14}$ cm^{-2}) the population of the first peak is dominant while for higher doses the population of the second peak becomes dominant. This evolution of peak population with increasing dose has been only observed in this case, i.e. for CVD SiC.

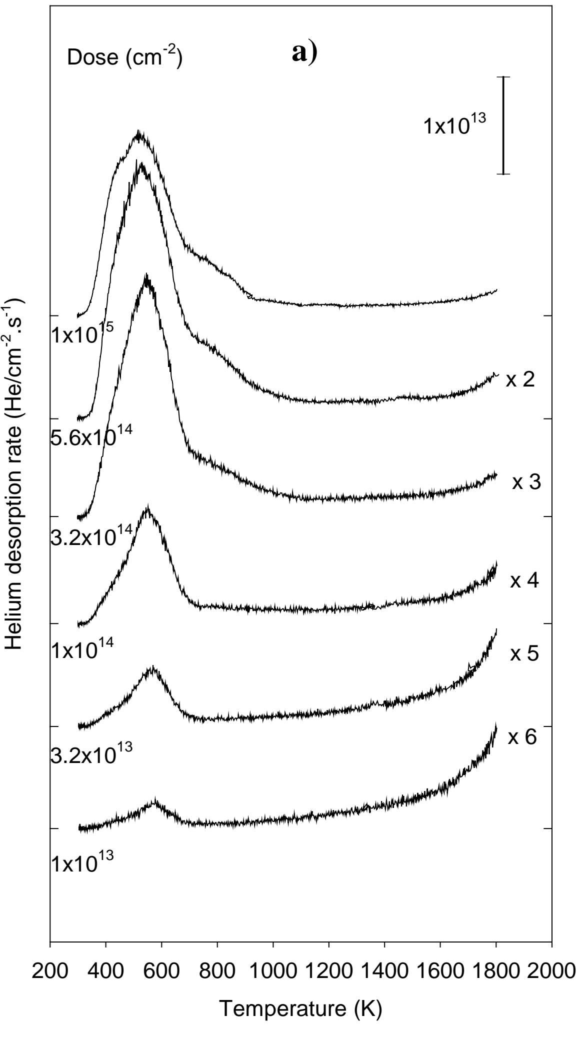

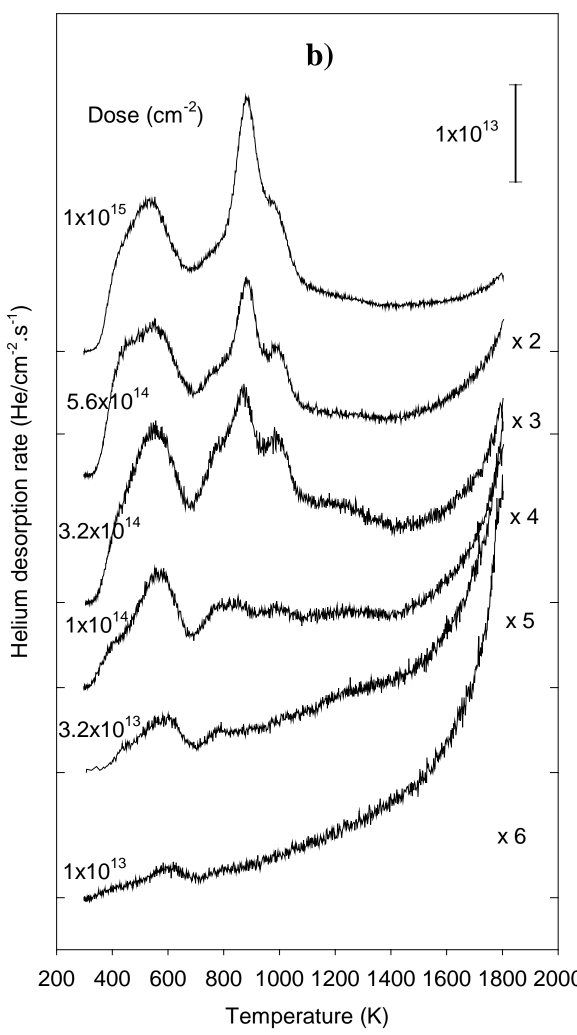

Figure 4.28: Desorption spectra obtained for CVD-SiC implanted with **(a)** 500 eV and **(b)** 1 keV He ions at the indicated doses.

For the 3 keV implantation two groups of peaks are also observed at 600 K and at 1000 K. The helium population in the second group of peaks is always found to be higher, i.e. for all doses. The evolution of the desorption spectra for a constant dose of $1x10^{15}$ cm^{-2} with increasing implantation energy (Fig.4.30) shows that the first group of peaks stays centered

on 600 K with its helium population decreasing while the second group of peaks is found to shift towards the higher temperature side (from 800 K at 500 eV, to 1100 K at 3 keV) with an increasing helium population.

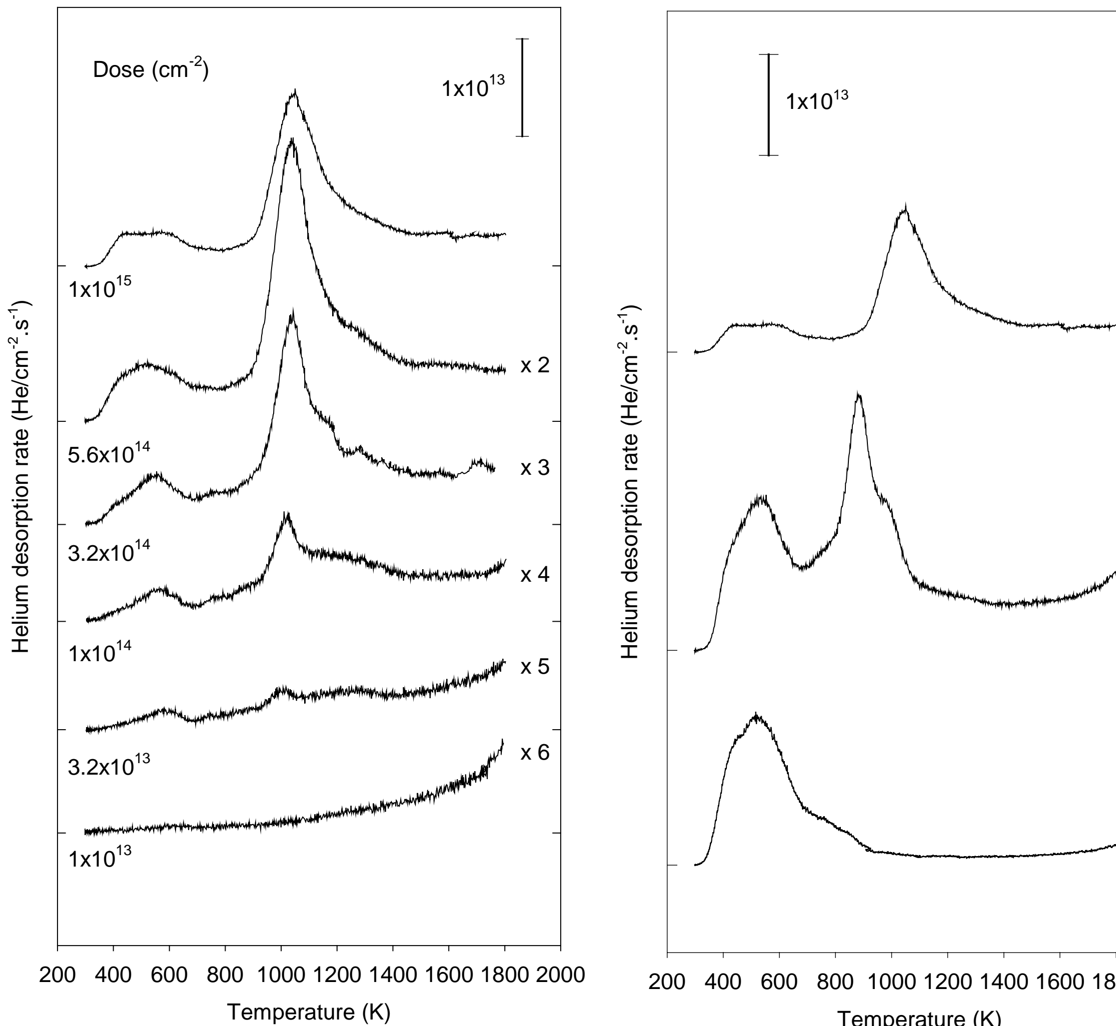

Figure 4.29: Desorption spectra obtained for CVD-SiC implanted with 3 keV He ions at the indicated doses.

Figure 4.30: Evolution of desorption spectra obtained for CVD-SiC implanted with He at different energies for a dose of $1x10^{15}$ cm^{-2}

4.2.5 Discussion

In order to relate the desorption peaks to particular types of defects, the mobility of the point defects during implantation has to be considered. Literature values for the migration energies of the point defects in SiC are given in Table 4.2.

Defect	E_{mig} (eV)	E_{form} (eV)	Source
He	1.10	0.70 (T_C), 1.07 (T_{Si})	Jung *et al.* [1992]
Si-Vacancy	2.88	14.28	Huang *et al.* [1995]
C-Vacancy	2.61	9.58	Huang *et al.* [1995]
Si-interstitial	4.12	2.09 (T_{Si}), 5.96 (T_C)	Huang *et al.* [1995]
C-interstitial	1.29	3.07 (T_C), 3.04 (T_{Si})	Huang *et al.* [1995]

Table 4.2: Formation and migration energies of point defects in silicon carbide given by the literature. T_{Si} denotes the silicon sub-lattice and T_C the carbon sub-lattice.

It was found by Huang *et al.* [1995] that a silicon vacancy migrates directly from one lattice site to another whereas a carbon vacancy migrates with the assistance of a silicon vacancy (indirect migration mechanism). Both types of interstitial migrate directly. It should be noted that none of the point defects is found to be mobile in SiC at room temperature (RT), the temperature of our implantations. An activation energy lower than 0.8 eV is required to migrate at RT on a timescale of 30 minutes (time required for the implantation procedure). However, bubbles are found to be readily formed at RT in the case of high dose helium implantation in SiC [Oliviero *et al.* 2001]. So during implantation, even at RT, the generated vacancies and self interstitials must be mobile, and in addition to recombining they may cluster and/or create a variety of defects through combining with impurities or pre-existing defects. This effect is observed for silicon in which interstitials are mobile even at temperature as low as 4 K and vacancies are highly mobile at 70 K. At high dose radiation enhanced diffusion plays an important role. In our low dose experiments radiation enhanced diffusion is not a dominant mechanism. It was shown that in all cases nearly 100 % of the implanted helium is trapped. Thus, helium is probably first trapped in shallow structural defects explaining the high trapped fraction. Upon subsequent annealing, during ramp heating, nucleation and growth of defect clusters takes place.

The properties of single He atoms or small clusters in the silicon carbide lattice are the basis for any fundamental understanding. The crucial parameters are the energies of He atoms at different sites in perfect and imperfect lattices since they determine the solubility, the paths of migration, the trapping to defects and the early stages of cluster formation. The formation energy of an interstitial helium E^{He}_{form}, the formation and migration energies of a vacancy and a

self-interstitial are predicted by atomistic calculations. These data are listed in Table.4.2 (see also appendix 2) and are schematically represented in the potential energy diagram (Figs.4.31-32). For SiC, the potential energy diagram of the system He-SiC is difficult to establish because of the lack of data and the fact that this two elements material shows two different interstitial sites (T_C and T_{Si}) each of them having two different configurations (tetrahedral or octahedral) and two vacancy types. Recent work by Allen *et al.* [1994] on the lattice location of helium implanted in SiC couldn't distinguished helium placement in either T-sites (tetrahedral interstices) or S-sites (substitutional site, i.e. a vacancy) for either the Si or C sub-lattice. On the other hand, the occupation of, or positioning near the ideal O-site (octahedral interstices) is prohibited. With the first MD calculations results obtained by Huang *et al.* [1994, 1995], two potential diagrams can be plotted: one for the silicon sub-lattice (Fig.4.31) and one for the carbon sub-lattice (Fig.4.32). However, these data have to be confirmed by additional calculations and/or be compared with experimental results.

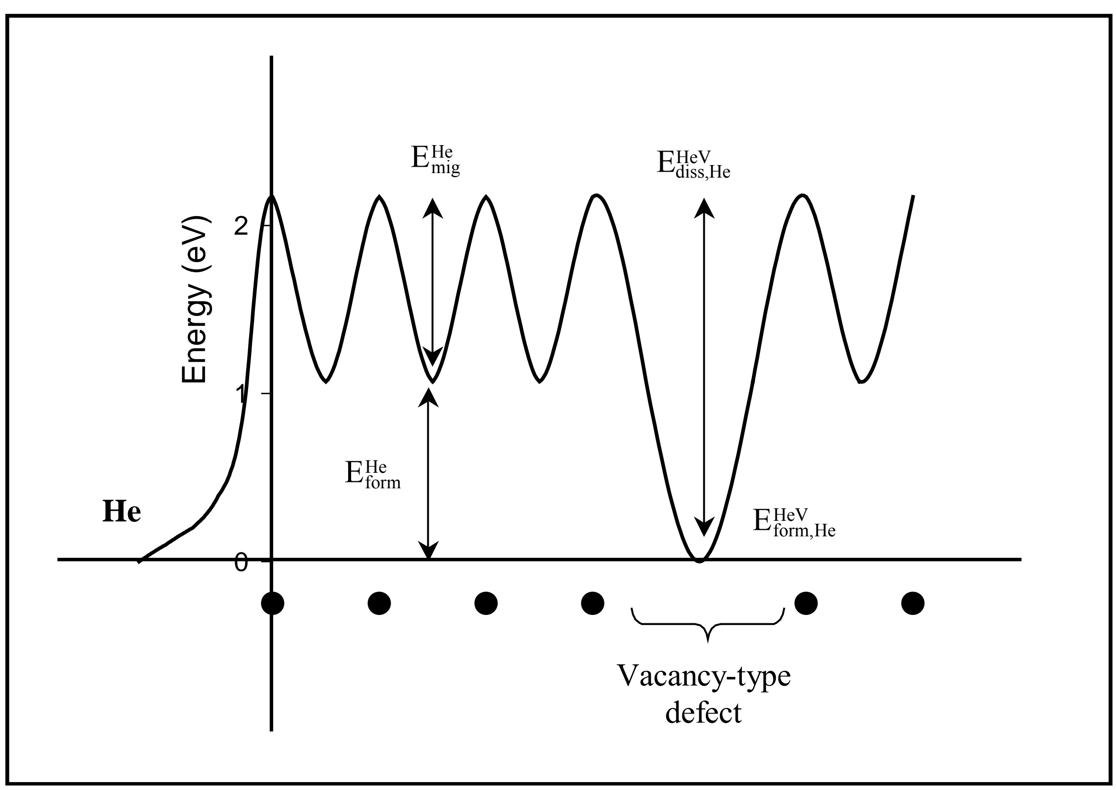

Figure 4.31: Potential energy diagram of helium in interaction with silicon carbide in the silicon sub-lattice. Helium at an interstitial position and helium at a vacancy are indicated.

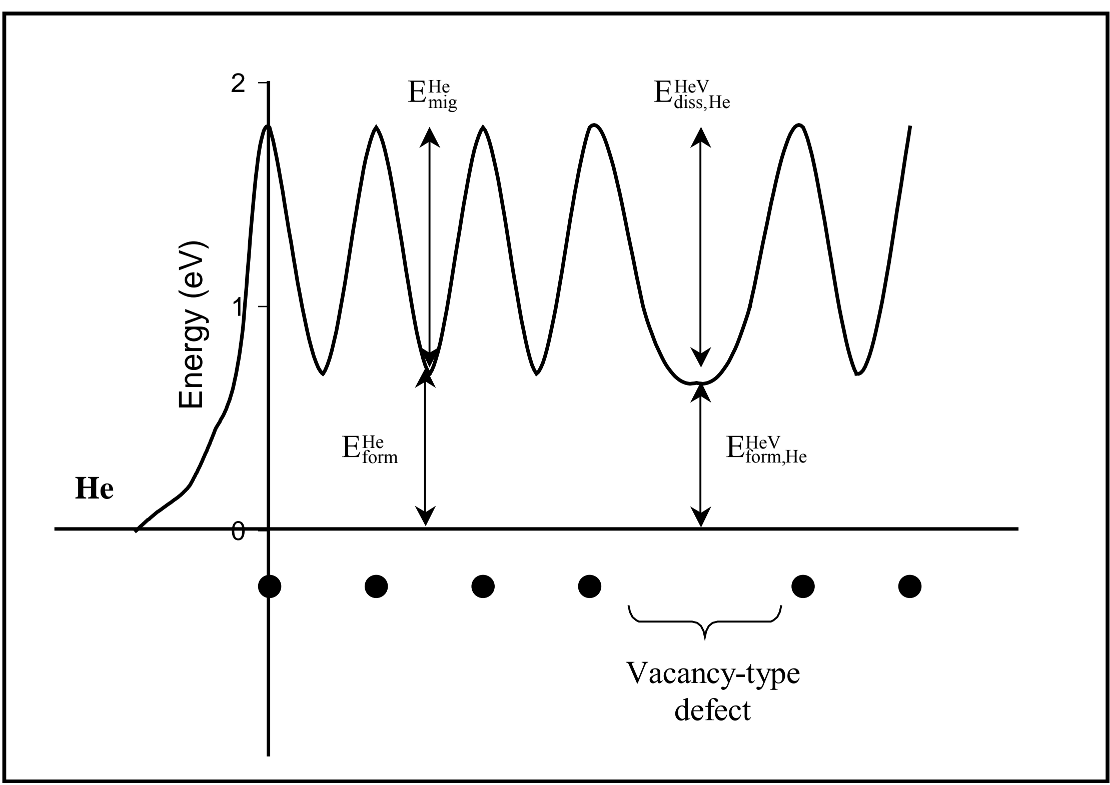

Figure 4.32: Potential energy diagram of helium in interaction with silicon carbide in the carbon sub-lattice. Helium at an interstitial position and helium at a vacancy-type defect are indicated.

In SiC, thermal helium desorption spectrometry shows that in case of low dose and low energy implantations, at least two types of defects are responsible for the trapping of helium, leading to two groups of peaks in the desorption spectra. Their presence, their temperature of maximal release as well as their helium population strongly depend on implantation parameters as well as the quality of the materials. However, applying simple first-order detrapping mechanisms with attempt frequencies of the order of the Debye frequency ($\nu = 10^{13}$ s^{-1}), the dissociation of the two groups of peaks can be roughly estimated (see Table.4.3). For the first-order desorption mechanism the desorption rate L(T) is given by Eqn.(4.8)

$$L(T) = -\frac{dN_{tr}}{dt} = N_{tr}\,\nu \exp\left(-\frac{E^{diss}}{kT}\right) \tag{4.8}$$

where N_{tr} is the number of helium filled traps, ν the attempt frequency, E^{diss} the dissociation energy, k the Boltzmann constant and T the absolute temperature. Using the relation between

the peak maximum temperature (T_{max}) and the corresponding dissociation energy given by Eqn.(4.9) where β is the ramp rate:

$$\frac{E_{diss}}{kT_{max}^2} = \frac{\nu}{\beta} \exp\left(-\frac{E_{diss}}{kT_{max}}\right) \tag{4.9}$$

a dissociation energy of 1.5 eV is found for the first group of peaks (at 600 K) and a dissociation energy of 3.2 eV for the second group (at 1200 K) in case of 6H and 4H-SiC. For the CVD-SiC, the first group has also a dissociation energy of 1.5 eV but the second group is found at about 1000 K giving a dissociation energy of 2.7 eV.

Sample	**6H-SiC**		**4H-SiC**		**CVD-SiC**	
Temperature (K)	600	1200	600	1200	600	1000
Dissociation energy (eV)	1.5	3.2	1.5	3.2	1.5	2.7

Table 4.3: Dissociation energy of He from defects in silicon carbide calculated by first-order desorption model.

In ***6H-SiC***, the evolution of each peak content with energy (Fig.4.19) is certainly due to a reduced probability for helium to escape to the surface when the helium is implanted deeper. It can also be assumed that for higher energies more defects are created and thus helium is trapped in more and larger defect clusters. This could imply that the group of peaks at low temperature is due to interstitial He and clusters of interstitial He, maybe in near-surface sites or to He release from pre-existing shallow structural defects while the group at high temperature is related to the de-trapping of He from He-vacancy clusters (see Table.4.4). The dissociation energy of 1.5 eV for the first group is in good agreement with the migration energy of interstitial helium quoted in literature [Jung 1992]. The shift observed for the two peaks with increasing dose or energy (Fig.4.15 and Fig.4.18) can be ascribed to He-vacancy clustering in an Ostwald ripening process. When increasing the dose/energy, He-vacancy clusters grow in an Ostwald ripening process and thus form more stable defects which dissociate at higher temperature. In the same time He-interstitials can be trapped by these more stable defects, reducing the size of He-interstitial clusters and thus lowering their temperature of dissociation.

6H-SiC		
Group of peaks at	600 K	1200 K
Energy variation	No shift of T_{max} Disappears at 3 keV Dominant for low energies	Shift of T_{max} towards high T° with increasing energy Dominant for high energies
Dose variation	Shift of T_{max} towards low T° with increasing dose at high energies for which the group is not dominant Population increase with dose	Shift of T_{max} towards high T° with increasing dose at low energies for which the group is not dominant Population increase with dose
Possible identification	He and/or cluster of He in interstitial position or He in pre-existing shallow structural defects	He de-trapping from He-vacancy clusters
Estimated dissociation energy (eV)	1.5 In agreement with the migration energy of interstitial helium (1.1 eV)	3.2

Table 4.4: Summary of the results obtained on He desorption from 6H-SiC.

For ***4H-SiC***, the results obtained on the first sample are in line with those obtained for the 6H-SiC. The two group of peaks are observed at nearly the same temperatures (600 K and 1200 K) and can also be ascribed to interstitial He and to detrapping of He from He-vacancy clusters. The fact that helium population is higher in the second group of peaks contrary to what was observed in 6H for a given energy might be ascribed to some surface effects, the 4H sample was polished (by Cree) contrary to the 6H sample which was used in the as-grown state.

After high dose experiment ($1x10^{16}$ cm^{-2}), the sample has experienced irremediable structural changes so that only a group of peaks at 600 K is observed in the desorption spectra for either low or high implantation energy and for both low and high doses. Even for annealing at high temperature (1800 K) for long time the sample couldn't be restored, i.e. no recovery of the damage occurs. The structural change due to the high dose implantation is thus thermally stable. The exact nature of this damage is unknown for the moment but could be related to the sample surface modification. When removing the sample from the desorption apparatus, a dark spot the size of the implanted area was visible on the surface of the sample. Moreover, desorption spectra obtained by Yamauchi *et al.* [1998] on isotropic graphite show also one single peak at 600 K with the same FWHM value. The dark spot might be a graphite layer. He implantation into this layer would lead to the single observed peak at 600 K. Experiments are in progress in order to characterize the surface of the sample. For an implantation energy of 1

keV, SRIM calculations [Ziegler *et al.* 1985] give a number of total displacement of 0.1 per ion per angstrom. For the implantation dose of $1x10^{16}$ $He.cm^{-2}$, a value of 1 dpa (displacements per atom) is found whereas McHargue *et al.* [1993] have shown that amorphization of SiC occurs for displacement values superior to 0.2-0.3 dpa. Thus, during the high dose experiment, amorphization of the sample has occurred. Afterwards, during the heating ramp, recrystallization takes place triggering off the observed helium release starting at 1200 K. This is in good agreement with the recrystallization temperature of 1173 K found in SiC [Hojou *et al.* 1996]. Moreover, polytypism is strongly expected as already observed after recrystallization of an amorphous layer induced by He implantation [Hojou *et al.* 1996]. As seen in Fig.4.33 amorphization has occurred only for the 1 keV implantation at high dose ($1x10^{16}$). For all other implantations, even for the highest dose used, the level of induced damage was below the threshold for amorphization.

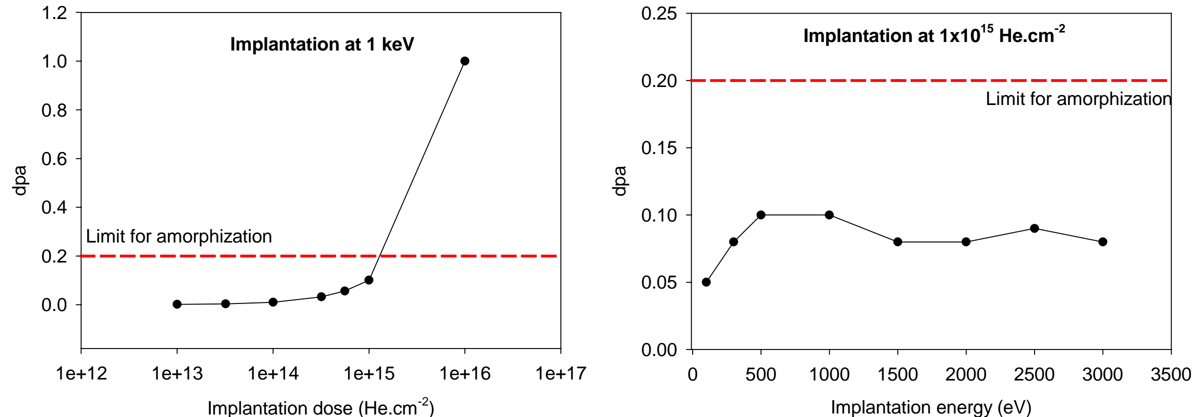

Figure 4.33: (a) displacement versus dose for He implantation in SiC at 1 keV and **(b)** displacement versus energy for He implantation in SiC at a dose of $1x10^{15}$ cm^{-2}, obtained from SRIM 2000. The dashed line indicates the threshold for amorphization.

For the second bulk 4H-SiC sample, only a group of peaks at 1400 K is contributing to the desorption spectra for all energies and doses. Its evolution with energy and doses is however similar to the one of the group at 1200 K previously observed. Thus this group is also ascribed to He detrapping from He-vacancies clusters. These results show that the defects associated to the first group of peaks at 600 K are not always present and depend on the sample. Again, this behavior could be ascribed to some surface effects. As previously seen, the state of the surface can strongly modify the helium release.

In ***CVD-SiC*** the same tendency observed for the 6H and 4H is followed but the release of helium in the high temperature regime is found to occur at a lower temperature (1000 K) than previously observed. This behavior may be ascribed to the quality of the materials since it is well known that many impurities are introduced in the sample during CVD process. CVD usually gives β-SiC, i.e. a cubic structure, with grain sizes of few micrometers. Jung *et al.* [2000] and Chen *et al.* [2000], have shown that bubbles can be easily formed in CVD SiC at grain boundaries (GB) for implanted doses as low as 200 atppm He. GB are pre-existing defects that act as strong gettering centers. Implanted helium, even at very low dose, is trapped at these defects and agglomerate to form bubbles. It is possible that the observed desorption peak at 1000 K is due to He detrapping from He-vacancy clusters at GB and not from He-vacancy clusters in the bulk. Moreover, the lower temperature of maximum release (1000 K) could be explain by the fact that He diffusion along grain boundaries is easier than in bulk material.

Considering all these results, the following remarks can be made. THDS shows that after low dose and low energy He implantation into SiC, all the implanted helium is trapped in at least two type of defects. The helium release in the high temperature regime can be ascribed, without too much controversy, to helium release from vacancy related defects, i.e. He_nV_m clusters (bubbles precursors). The temperature of maximum release, at a given implantation dose and energy, can vary with samples, as seen for CVD-SiC, but the group of peaks is still attributed to release from He_nV_m clusters. The shift towards higher temperature observed in all cases with increasing energy or dose is consistent with He_nV_m clusters that grow when more defects are created and that become more stable. For the low temperature regime at 600 K, several identifications are emerging. From the results in 6H-SiC, it can be assumed that He is trapped in either an interstitial position or in pre-existing shallow structural defects. But, as seen in 4H-SiC the surface state seems also to strongly affect this group of peak. The roughness of the sample might favor this helium trapping. Moreover, after the high dose experiment, i.e. after amorphization and recrystallisation of the sample, only a group of peaks at 600 K is observed and is related to He desorption from a carbon layer. If it is the same defect as observed in other cases, the group of peaks at 600 K would be due to He desorption from a carbon layer present on the sample's surface.

4.2.6 Conclusion

Thermal Helium Desorption Spectrometry (THDS) was used to characterize the helium implantation-induced defects in SiC. Two types of defect were clearly distinguished in 4H and 6H-SiC leading to two different groups of peaks in the desorption spectra: one group at low temperature centered at 600 K and an other group at high temperature centered at 1200 K. The first group (at 600 K) might be attributed to interstitial He and clusters of interstitial He to He trapped in pre-existing shallow structural defects or to He desorption from a over surface carbon layer. The second group (at 1200 K) could be related to the de-trapping of He from He-vacancy clusters. Ostwald ripening processes are suggested to occur when increasing the dose and/or the energy and induce a shift of the 1200 K desorption peak towards higher temperature. All the implanted helium appears to be trapped at room temperature. However, the intrinsic properties of the materials used in the study seem to play an important role since different behaviors were observed for the different samples. Indeed, for CVD-SiC, a group of peaks at 1000 K was observed in addition to the first group at 600 K. This peak could be related to He detrapping from grain boundaries. Finally, the state of the surface seems to be a determinant parameter for the helium trapping/release behavior.

References

[Allen *et al.* 1994] W.R. Allen, *J. Nucl. Mater.* **210**, 318 (1994).

[Chen *et al.* 2000] J. Chen, P. Jung, H. Trinkaus, *Phys. Rev. B* **61**, 12923 (2000).

[Fedorov *et al.* 1998] A.V. Fedorov, A. van Veen, *Computational Materials Science*, **9**, 309 (1998).

[Hojou *et al.* 1996] K. Hojou, S. Furuno, K.N. Kushita, H. Otsu, Y. Furuya, K. Izui, *Nucl. Instrum. Methods Phys. Res. B* **116**, 382 (1996).

[Huang *et al.* 1994] H. Huang , N. Ghoniem, *J. Nucl. Mater.* **215**, 148 (1994).

[Huang *et al.* 1995] H. Huang, N.M. Ghoniem, J.K. Wong, M.I. Baskes, *Modelling Simu. Mater. Sci. Eng.* **3**, 615 (1995).

[Jung 1992] P. Jung, *J. Nucl. Mater.* **191-194**, 377 (1992).

[Jung *et al.* 2000] P. Jung, H. Klein, J. Chen, *J. Nucl. Mater.* **283-287**, 806 (2000).

[McHargue *et al.* 1993] C.J. McHargue, J.M. Williams**,** *Nucl. Instr. Methods Phys. Res. B* **80-81**, 889 (1993).

[Myers *et al.* 1993] S.M Myers, D.M. Bishop, D.M. Follstaedt, H.J. Stein, W.R. Wampler, *Mater. Res. Soc. Symp. Proc.* **283**, 549 (1993).

[Oliviero *et al.* 2001] E. Oliviero, M.L. David, J. Nomgaudyte, L. Pranevicius M.F. Beaufort, A. Declémy, J.F. Barbot , *J. Appl. Phys.* accepted (2001).

[Raineri *et al.* 2000] V. Raineri, M. Saggio, E. Rimini, *J. Mater. Res.* **15**, 1449 (2000).

[Yamauchi *et al.* 1998] Y. Yamauchi, Y. Hirohata, T. Hino, *Fusion Eng. and Des.* **39-40**, 427 (1998).

[Ziegler *et al.* 1985] J.F. Ziegler, J.P. Biersack, U. Littmark, *The Stopping and Range of Ions in Solids* (New York: Pergamon), (1985).

5-Discussion: He bubble formation in Si

Even if many experiments have been performed to study He bubbles/cavities in silicon, so far no clear understanding of their nucleation and growth process has emerged. In order to well describe this phenomena, bubble nucleation and growth during implantation and bubble growth during annealing have to be distinguished. In the following in the highlight of much experimental work, we will discuss bubble formation.

5.1 During implantation at room temperature

5.1.1 Bubble nucleation

Implantation of He in silicon creates point defects (V, I). These primary defects, including He atoms, can be seen as the bubble precursors. If impurities or pre-existing defects are already present in the material, they might also play the role of precursors. Let's consider in the following the easiest configuration with vacancies, self-interstitials and helium only. First, the mobility of these entities has to be taken into account. Vacancies and self-interstitials are known to be highly mobile at room temperature while He is not mobile [Baskes *et al.* 1989, Weringen *et al.* 1956]. It is clear that vacancies and self-interstitials can easily recombine. For example, according to SRIM calculations, a 50 keV He ion products nearly 190 Frenkel defects in silicon, although only a few percent will survive the displacement cascade recombination (~3 % for low doses [Svensson *et al.* 1993]). Nevertheless, these defects will play the role of bubble precursors, since He atoms are particularly expected to strongly interact with vacancies. It is highly probable that self-interstitials, as primary defects (i.e. single interstitials and not clusters of interstitials), will not play a major role in the initial stage of bubble nucleation/growth. As mentioned above, if pre-existing defects such as dislocations or extended defects, i.e. agglomerates of interstitials, already exist, they will strongly favor the formation of bubbles at their vicinity. This was observed for extended defects [Peeva *et al.* 2002, Myers *et al.* 1999]. Self-interstitials will thus be left apart for the moment. At the initial stage (i.e. at low dose), when displacement cascades do not overlap, vacancies and implanted He may cluster separately or may interact. The isolated vacancy (monovacancy) cannot be observed at room temperature [Cerofolini *et al.* 2000]. Moreover, it has been found that a divacancy is more stable than two isolated vacancies by 1.5 eV [Hastings *et al.* 1997]. The

divacancy V_2 is one of the prominent defects appearing after particle irradiation as observed by DLTS (cf. §2). Vacancies are thus expected to cluster. Of course higher order clustering is possible. It was shown that, vacancies form larger clusters in order to minimize energy and that the hexavacancy is the most stable of the small vacancy clusters. The other possibility is that a vacancy cluster directly with a He atom. But, it was shown that the monovacancy-helium interaction is repulsive [Alatalo *et al.* 1992]. Estreicher *et al.* [1997] have proved that helium can be dissolved exothermically in a divacancy. As for the helium, it seats preferentially in T_d sites and tends to cluster, the energy per atom gained when forming a pair being – 0.04 eV [Alatalo *et al.* 1992]. The conclusion to be drawn from all this is that bubble nucleation may result from the clustering of a divacancy with a helium atom (HeV_2), of a divacancy with two helium (He_2V_2) or of multivacancies with helium (He_nV_m). In any case, gas atom-vacancy clusters are formed which can thereafter act as nucleation centers. When collision cascade overlapping occurs, the following implanted helium and surviving vacancies can be trapped at the existing nuclei leading to the beginning of the growth stage since bubble growth starts when stable embryos are formed. In Fig.5.1, a schematic representation of the bubble nucleation is proposed.

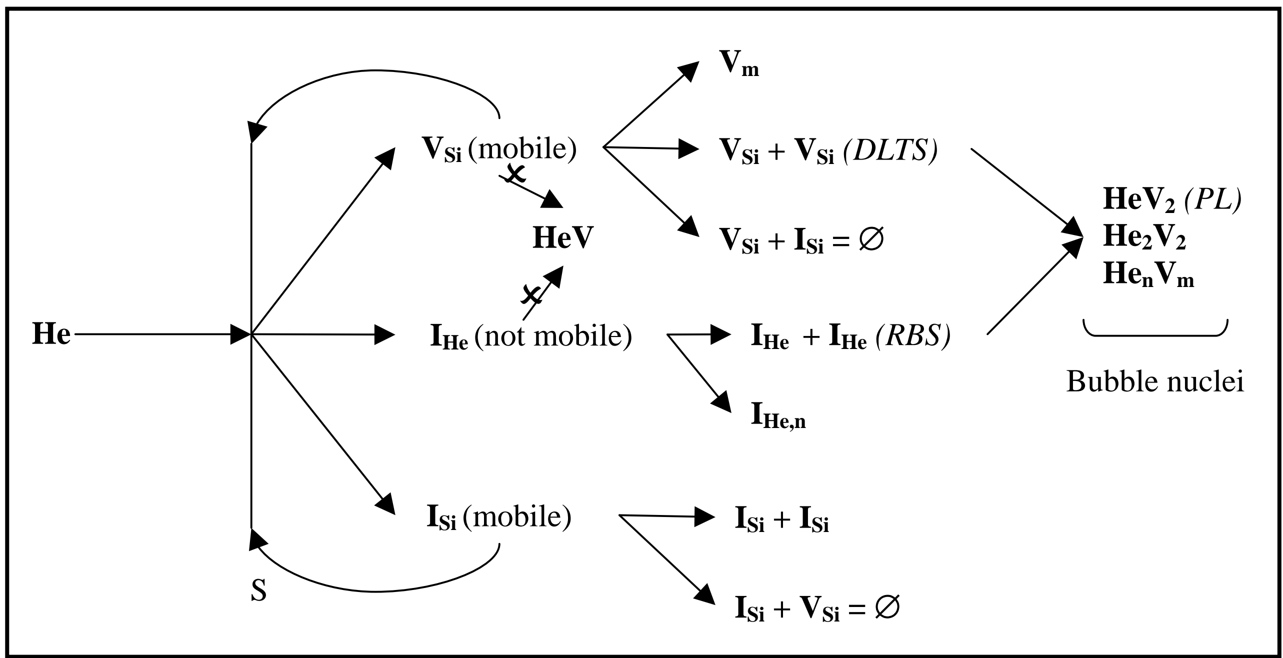

Figure 5.1: Schematic view of bubble nucleation in He implanted silicon.

5.1.2 Bubble growth

From a general point of view, bubble growth mechanisms depend on many parameters such as the production rate and migration rate of self-interstitials, vacancies and helium atoms, the nature and concentration of sinks, and the sink strength. Information on the first stage of bubble growth process are difficult to obtain since TEM is not able to detect clusters of size below the resolution limit of about 1 nm. However, it can be assumed that a bubble grows by diverse mechanisms that will be described later. The simplest process would be that the bubble grows by collection of vacancies, helium atoms or even of helium-vacancy complexes. Another mechanism that can also be envisaged is migration and coalescence. Oswald ripening is unlikely because of the continuous helium and vacancy supply during implantation. Loop punching can also occur but is more expected for isolated bubbles, i.e. in regions where the vacancy production rate is low. With increasing dose up to $1x10^{16}$ cm^{-2}, He_nV_m clusters grow and small bubbles are created. These small bubbles can be observed by TEM. It was found that for increasing dose (from $1x10^{16}$ up to $1x10^{17}$ cm^{-2}), the bubble density increases while the diameter of bubbles (1-2 nm) slightly increases [Raineri *et al.* 2000]. Simulation of the formation of bubbles with the program MODEX [Federov 2000] has shown that during implantation the mean bubble size saturates at about 1 nm. It thus can be assumed that when implanting at higher dose, more nuclei are formed leading to a higher ~1 nm bubble density. Thereafter, coarsening occurs explaining the small evolution of bubble size.

5.1.3 Critical dose for bubble formation

It was found that a dose of about 10^{16} cm^{-2} is needed in order to obtain bubble/cavities after subsequent annealing [Myers *et al.* 1993, Fedorov *et al.* 1998, Raineri *et al.* 2000]. Because helium has a high permeability in silicon, it can easily escape from the sample during annealing step. Thus during implantation, stable He-vacancies complexes need to be created that won't dissociate at low temperatures. As seen by THDS [Van Veen 1991], He dissociates from small vacancy-helium clusters at low temperature (400 K) leaving small vacancy clusters that will also dissolve and recombine with interstitials. As an example divacancies anneal out at temperatures above 350 °C [Libertino *et al.* 1997]. On the contrary for bubbles (i.e. bigger vacancy-helium clusters), because of entropy effects, helium release will occurs at

higher temperature (1200 K) and clusters left in the sample will be more stable allowing the growth of bubbles/cavities. It seems that the critical size for helium-vacancies clusters corresponds to the TEM detection limit (~1 nm). Indeed, bubbles/cavities have never been observed after annealing if bubbles were not seen in the as-implanted samples [Raineri *et al.* 2000]. The size of bubbles in the as-implanted sample is not the only limiting parameter. As stated by Fedorov [2000] the density of stable clusters is also a determining factor for the formation of cavities. As mentioned above, during annealing small clusters dissociate providing a source of mobile vacancies. The vacancy diffusion length inside the damaged area should be less than the distance to the surface in order to allow retrapping by the bigger clusters. Then, cavity formation occurs. Otherwise, an alternative route for bubbles/cavities formation is found. This was clearly revealed by the medium dose study (cf. §3). As seen, for medium dose implantations small bubbles (~1 nm) are observed in the as-implanted sample. However this leads to a diluted system after annealing. For the low flux, where fewer vacancies are produced, it is assumed that the bubble density in the as-implanted sample is smaller. During annealing small clusters dissociate and vacancies are lost and the bigger clusters grow by trap-mutation or loop punching leading to the diluted system. With increasing flux, it is assumed that the density increases in the as-implanted sample leading, after annealing to a system closer to a condensed one.

5.2 Bubble growth during annealing

During annealing two effects occur simultaneously: the growth of bubbles and the He desorption. It should be considered that at some point only cavities will be present, i.e. bubbles empty of helium. It is often found that Oswald ripening (OR) and migration and coalescence (MR) are the two mechanisms responsible for bubble/cavities growth. They are briefly described below.

- Oswald Ripening (Fig.5.2b)

  This mechanism is based on the fact that the coexistence of bubbles with different sizes and pressures induces a concentration gradient. Helium atoms or vacancies permeate from the small bubbles to larger bubbles. This mechanism is stopped when bubble sizes become homogenous and/or when distances between bubbles become too large to create a concentration gradient.

- Migration and Coalescence (Fig.5.2a)

  This mechanism relies on the fact that bubbles can migrate and that coalescence occurs when bubbles come into contact with each other. The random migration of bubbles is due to atoms changing their position on the bubble surface. This can occur by surface diffusion, by volume diffusion or by vapor transport. The bubble diffusion coefficient is inversely proportional to the bubble radius. Thus small bubbles are expected to migrate easily. This mechanism is limited by the bubble diffusion length.

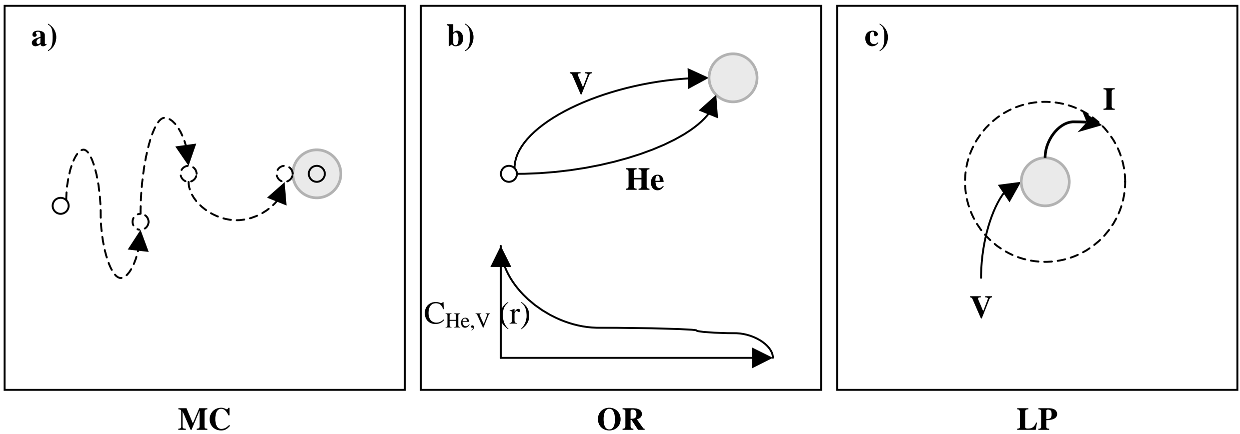

Figure 5.2: Schematic representations of the coarsening mecanims:
(a) Migration and coalescence, **(b)** Oswald Ripening, **(c)** Loop Punching.

Raineri *et al.* [2000] states, in a recent review on bubbles in silicon, that both mechanisms take place. Direct coalescence is observed in case of a very high local density of small cavities/bubbles and is found to occur at temperature up to 1000 °C. But ripening is found to be the main mechanism. Recently, Donnelly *et al.* [2001] have studied bubble growth by in situ annealing TEM experiments. They have also found that bubble growth is due to Oswald ripening and coalescence in the early stages of annealing at 700 °C. Motion of small bubbles was not observed but direct coalescence sometimes occurred. For annealing up to 850 °C, motion of small bubbles doesn't occur but migration and coalescence of a few large bubbles was recorded.

It should be noted, as shown in §3, that an alternative bubble growth occurs when no or less vacancies are available. Indeed, loop punching and trap-mutation can be seen as alternative mechanisms in case of a lack of vacancies. These two mechanisms have been already

described in previous sections. Loop punching is schematically represented in Fig.5.2c. It is evident that these two mechanisms are limited to bubbles and cannot be applied in case of cavities.

Finally, no clear evidence of the mechanism involved in bubble growth has emerged up to now. Different processes are competing or occur simultaneously depending on many parameters such as bubble size, density, pressure, annealing temperature and time. It is thus difficult, or even impossible to propose a general mechanism for bubble/cavity growth. Invariances of the two coarsening mechanisms (OR and MC) should maybe be investigated in order to construct bubble growth mechanisms maps as done in metals [Schroeder *et al.* 1991, Goodhew, 1991].

References

[Alatalo *et al.* 1992] M. Alatalo, M.J. Puska, R.M. Nieminen, *Phys. Rev. B* **46**, 12806 (1992).

[Baskes *et al.* 1989] M.I. Baskes, J.S. Nelson, A.F. Wright, *Phys. Rev. B* **40**, 6085 (1989).

[Cerofolini *et al.* 2000] G.F. Cerofolini, F. Corni, S. Frabboni, C. Nobili, G. Ottaviani, R. Tonini, *Mat. Sci. Eng.* **27**, 1 (2000).

[Donnelly *et al.* 2001] S.E. Donnelly, V.M. Vishnyakov, R.C. Birtcher, G. Carter, *Nucl. Inst. and Meth. B* **175-177**, 132 (2001).

[Estreicher *et al.* 1997] S.K. Estreicher, J. Weber, A. Derecskei-Kovacs, D.S. Marynick, *Phys. Rev. B* **55**, 5037 (1997).

[Fedorov *et al.* 1998] A.V. Fedorov, A. van Veen, *Computational Materials Science*, **9**, 309 (1998).

[Fedorov 2000] A.V. Fedorov, Ph.D thesis, Technological University of Delft, 2000.

[Goodhew 1991] P.J. Goodhew**,** in: *Fundamental Aspects of Inert Gases in Solids*, S.E. Donnelly, J.H. Evans (Eds), NATO ASI series B, Physics 279, Plenum Publishing Corp., New York, 1991, pp 349-356.

[Hastings *et al.* 1997] J.L. Hastings, S.K. Estreicher, P.A. Fedders, *Phys. Rev. B* **56**, 10215 (1997).

[Libertino *et al.* 1997] S. Libertino, J.L Benton, D.C. Jacobson, D.J. Eaglesham, J.M. Poate, S. Coffa, P.G. Fuochi, M. Lavalle, *Appl. Phys. Lett.* **71**, 389 (1997).

[Myers *et al.* 1993] S.M Myers, D.M. Bishop, D.M. Follstaedt, H.J. Stein, W.R. Wampler, *Mater. Res. Soc. Symp. Proc.* **283**, 549 (1993).

[Myers *et al.* 1999] S.M Myers, D.M. Follstaedt, *J. Appl. Phys.* **86**, 3048 (1999).

[Peeva *et al.* 2002] A. Peeva, J. Kaschny, R. Kögler, W. Skorupa,(Gadest 2001),published in Solid State Phenom. **82-84** 399 (2002).

[Raineri *et al.* 2000] V. Raineri, M. Saggio, E. Rimini, *J. Mater. Res.*, **15**, 1449 (2000).

[Schroeder *et al.* 1991] H. Schroeder, P.F.P. Fichtner, *J. Nucl. Mater.* **179-181**, 1007 (1991).

[Svensson *et al.* 1993] B.G. Svensson, C. Jagadish, J.S. Williams, Nucl. *Instr. Meth. Phys. Res. B* **80-81** 582 (1993).

[Van Veen 1991] A. van Veen, in: *Fundamental Aspects of Inert Gases in Solids*, S.E. Donnelly, J.H. Evans (Eds), NATO ASI series B, Physics 279, Plenum Publishing Corp., New York, 1991, pp 41-57.

[Weringen *et al.* 1956] A. van Weringen, N. Warmoltz, *Physica* **22**, 849 (1956).

6-Conclusion

Defects induced by helium implantation in silicon and in silicon carbide have been studied. First, the effects of medium doses MeV implantation in silicon have been investigated. In this particular dose regime, the influence of dose-rate on bubbles and defects formation has been examined. The effects of varying the dose have been also described. Thereafter, the influence of annealing time on bubbles and defects formations in case of high dose MeV implantation has been studied. Finally, high temperature 50 keV He implantations in silicon at a dose of $5x10^{16}$ cm^{-2} have been investigated by conventional and partial desorption techniques as well as TEM. In SiC, bubble formation by high doses MeV helium implantation has been investigated and different anneals have been performed with intent to form stable cavities. THDS was used to study the helium bubbles precursors in SiC.

We have shown that the nucleation and growth of He induced cavities in silicon as well as the related defects in the case of a $2x10^{16}$ He/cm^2 implantation at 1.6 MeV follow an alternative route. After annealing, a buried layer is observed, in which planar clusters of helium bubbles lying on the {001} planes are randomly distributed. At these latter, prismatic punching is found to occur and gliding dislocations loops are emerging. It is determined that such He bubble structures nucleate and grow by the formation of He-filled platelet structures, almost certainly by the trap-mutation process, which transform into planar clusters of spherical bubbles upon thermal annealing. The rows of loops dislocations, which extended over a few micrometers away from the buried layer, are related to these clusters. We have shown that the clusters act as dislocation loop sources, due to the induced stress in the matrix. Within the bubble band, some of the bubbles are bounded to Frank dislocation loops. We have shown that these Frank loops are generated by loop punching.

We have shown the dose-rate, i.e. the vacancy production rate, to strongly influence the formation of He induced cavities in silicon, in the case of a $2x10^{16}$ He/cm^2 implantation at 1.6 MeV. In all the as-implanted samples, a layer of small helium bubbles is observed. On the TEM micrographs no visible differences are noticed for the different fluxes. However, after annealing, complete different features of the micro-structural evolution of the cavity systems are observed for each flux. For the lowest flux, platelets and planar clusters of helium bubbles are distributed along R_p range and are surrounded by a tangle of dislocations. No continuous bubble band is observed. For the medium and the highest flux, a continuous bubble band is observed, intersected by rather homogeneous distributed planar clusters of helium bubbles

from which prismatic punching is found to occur. The emerging gliding dislocation loops are found to extend over few micrometers away from the buried layer. Within the bubble band, some of the bubbles are bounded to Frank dislocation loops showing that loop punching is involved in the bubble growth. The width of the bubble band, the cluster size, habit planes as well as their concentration are shown to be dose-rate dependent. These behaviors are discussed in terms of vacancy concentration, over-pressured He_nV_m clusters and of trap-mutation process.

Defects in silicon induced by high dose helium implantation are shown to be strongly dependent on the incident energy range. In the case of MeV Helium implants in silicon at a dose of 10^{17} cm^{-2} followed by an 800°C annealing two different layers of damage are observed. The first one is made up of a large density of bubbles with embedded dislocations whereas the second, located behind the first, contained two types of extended defects: {113}'s and Frank loops. The extended defects are greatly affected by the annealing time whereas the bubble morphology do not really change. For a 15 min anneal, only Frank dislocation loops bound to bubbles are observed. For longer annealing time {113} defects are formed implying the trapping of Si interstitials at the small interstitial clusters already formed during the implantation. With increasing annealing time, {113} defects are found to dissociate and only Frank loops homogeneously distributed and with a roughly constant size are observed. These defects are more stable than {113}'s and longer annealing times are needed to dissolve them, as observed after a 17 h anneal. Further studies are necessary to determine the decay rates of both defects, the dominant loss mechanism of interstitials and the role of the bubble band in the injection of interstitial atoms that have escaped from the damage region. All these results have shown that the involved processes are different to those already observed for keV implantation where only one layer of bubbles was observed whatever the annealing time may be.

In case of high temperature keV implantation, it has been shown that the helium release from bubbles/cavities is well described by a permeation process with an activation energy of 1.8 eV as previously found for room temperature keV or MeV implantations. Helium release from bubbles is thus shown to be independent of implantation parameters. As expected the amount of helium retained in the sample is found to decrease with increasing implantation temperature and to be drastically reduced for the 600°C-implantation. However, even for 800°C-implantation, where no bubbles/cavities are detected by TEM, a very small amount of helium is retained in the sample certainly at the observed extended defects. Finally, it has

been shown that pressure/entropy effects plays a major role on the helium desorption from bubbles.

Implantation at room temperature of high dose helium ions into SiC is shown to lead to the formation of small bubbles. However, the critical dose for forming bubbles exceeds the dose for amorphization and a multilayer structure is observed: an amorphous layer surrounded by crystalline zones of point defects. Only a slight recovery of the damaged layer is observed after a 800°C-30 min annealing with no change in bubble morphology. The in-situ annealing has shown that the electron beam induces the epitaxial regrowth of the amorphous layer only from the upper interface in the region free of bubbles. The presence of bubbles in the other amorphous region prevents the electron beam induced recrystallisation. At higher temperature (1500°C) recrystallization is taking place resulting in a complex structure with inclusions of epitaxial 3C-SiC and columnar growth of 4H-SiC. The 1500°C anneal relaxed the structure and enlarged the cavities. However, their size, shape and density are found to be different depending on their localisation in the damaged band.

Simultaneously, the multilayered structure is simulated using a mathematical formalism considering the atomic relocations between monolayers. It is shown that atomic displacements initiate mass-transport. By comparing the calculated profiles with the TEM results we note that the circular bubbles are formed where flux of atoms initiated by displacement processes is negligible whereas smaller bubbles (or voids) and epitaxial recrystallization occur in the region of excess interstitials where the flux is maximum.

THDS has shown that in 6H and 4H-SiC, in case of low dose and low energy implantations, two types of defect can be clearly distinguished leading to two different groups of peaks in the desorption spectra: one group at low temperature centered at 600 K and an other group at high temperature centered at 1200 K. The first group (at 600 K) might be attributed to interstitial He and clusters of interstitial He, to He trapped in pre-existing shallow structural defects or to He desorption from an over surface carbon layer. The second group (at 1200 K) could be related to the de-trapping of He from He-vacancy clusters. In CVD-SiC the first group of peak is also observed with another group of peak at 1000 K certainly due to He detrapping from grain boundaries. This study has shown that helium trapping in SiC strongly depends on the intrinsic properties and qualities of the materials. Moreover, the state of the surface seems to be a determinant parameter for the helium trapping/release behavior.

Appendix 1: Experimental techniques

A.1.1 Thermal Helium Desorption Spectrometry (THDS)

The principle of this technique, Fig.A.1.1, has been described by Kornelesen and van Gorkum [1981] and by van Veen *et al.* [1981,1991]. A typical experiment can be divided into four steps.

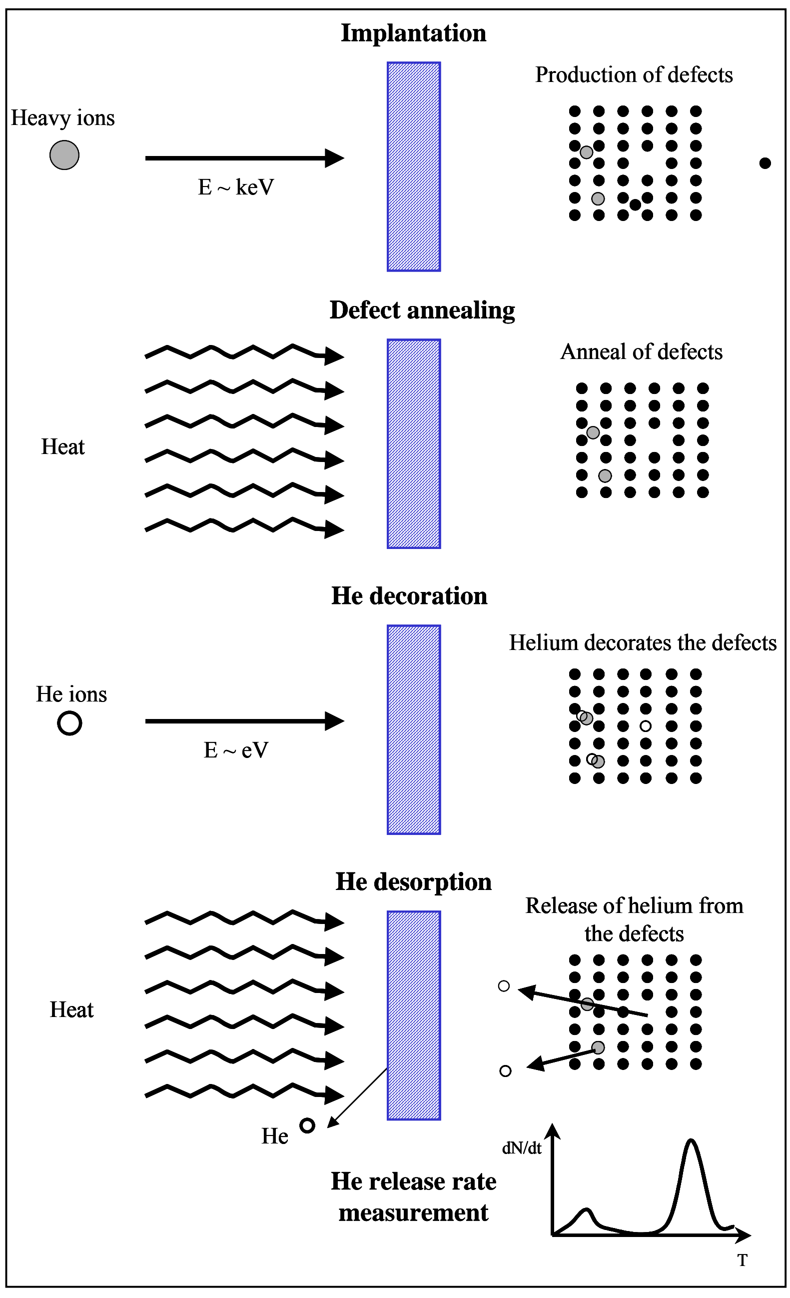

Figure A.1.1: The principle of a typical THDS experiment.

The first step is the **damage production step**: point defects are created in the sample by implantation of gas or metal ions. These points defects, i.e. implanted gas atom, self-interstitials and vacancies, depending on their mobility during implantation and on the concentration of intrinsic traps in the material, can be trapped in the sample, can recombine or can migrate to the implanted surface and be released. In the case of gas ions, implanted gas atoms are accumulated in the material and are trapped at pre-existing defects and/or at the defects created during implantation.

The second step is the **defect anneal step**: the sample is subjected to annealing at a given temperature to restore the crystal.

The third step is the **helium decoration step**: low energy helium implantation is used to decorate the defects with helium ions. The helium ion is chosen because of its low solubility in most materials and therefore its high sensitivity for open volumes. Moreover helium is chemically-inert in most materials. The ideal experiment requires that the introduction of the helium do not induce extra damage. It can be calculated that the kinetic energy of the helium should be below the threshold for damage production as follows: $E_{th} = E_d/G(m,M)$, where E_d is the displacement energy and $G(m,M) = 4mM/(m+M)^2$ is the factor for maximum energy transfer in a single collision of helium (mass m) with the atoms (mass M) of the material. Thus introduction of helium by ion irradiation is limited to a certain maximum energy. When light impurities are present in the material, threshold energies may be lower because collision sequences in which the impurity is involved may occur. For helium energies higher than the threshold energy, Frenkel pairs are formed which give rise to the building of vacancies. A consequence of low energy helium implantation is that the helium is introduced at a rather shallow depth below the surface (typically 1 nm deep). However at low defect concentrations the helium, if it is mobile at room temperature in the material, can reach deeper-lying defects by diffusion.

Finally, the fourth step is the **helium desorption step** which leads to the desorption spectrum: the helium release rate is monitored while heating the sample with a constant heating rate $\beta = dT/dt$ (in the range 1-10 K/s) up to a certain temperature. From the desorption peaks contributing to the desorption spectrum the population of defects can be derived in a quantitative way. Analysis of the desorption peaks yields values of the defect detrapping enthalpies, jumping frequencies, diffusion enthalpies [Kornelsen *et al.* 1981, Redhead 1981, Van Veen 1987]. The method gives unambiguous results when defect densities are low and therefore the helium diffusion length is larger than the average distance between the defects. At higher densities retrapping of detrapped helium plays a role. A description of the trapping

and de-trapping processes has been given in a article [Buters *et al.* 1987]. For defect assignment, use is made of the opportunity offered by low energy sub-threshold helium irradiation to decorate defects in a controlled way with an increasing amount of helium. Also a method is employed where self-interstials are injected into the sample by irradiation with low energy heavy ions. Interaction of the self-interstitial with vacancy complexes leads to size reduction or removal of the complexes.

In our experiment, the ions used for creating damage are the same as the probing atoms, that is to say helium. Therefore, our typical experiment can be described only by steps 1 and 4. Steps 2 and 3 are not required.

A.1.2 Equipment

The experimental set-up developed by Van Veen *et al.* [1981] is shown in figures A.1.2-3. The set-up can be used in two different configurations:

- "In-situ implantation" configuration,
- "Oven" configuration.

The basement of the set-up consists of an ultra high vacuum (UHV) working chamber, a quadrupole and a calibration system. The ultra high vacuum in the working chamber is achieved by a sequence of a turbo-molecular pump, a diffusion pump and a backing pump in series. This combination provides the low hydrogen background pressure necessary for measurements of helium release. The quadrupole used in the set-up shown in Fig.A.1.3 is a Balzers QMG 111 B analyzer. The calibration system consists of a 1*l* volume filled with the calibration gas (helium) at a known pressure, typically 2×10^{-5} mbar. During the calibration procedure 1 cm^3 of gas from the 1*l* volume is released into the working chamber and is measured by the quadrupole. The volume of 1 cm^3 at 2×10^{-5} mbar pressure and at room temperature contains 5.3×10^{11} molecules (or atoms for noble gases). The number of gas atoms or molecules divided by the total number of recorded counts yields the sensitivity Q. For helium, a typical value is Q = 10^6-10^7 He/count.

- *"In-situ implantation " configuration (Fig.A.1.3):*

The samples, which are held in a rack (Fig.A.1.2), are facing an ion gun on one side and an electron gun on the other side (see Fig.A.1.3). Three different samples can be put inside the system and can be selected by moving the rack up or down. A diaphragm (ϕ = 25 mm) is used for implantation and is removed during annealing. The ion gun can form gas ions and implant them into the sample with a maximum energy of 3 keV. A Wien ExB filter provides mass separation so that only the desired ions are implanted. Sweep plates located directly in front of the sample ensure a uniform dose distribution over the implanted area. The electron gun used for the annealing of the sample consists of a tungsten filament and a molybdenum grid. Both are at a 2 kV negative potential relative to the sample. The maximum temperature that can be reached is about 2000 K at a heating rate of 10 K/s. The temperature is measured by means of thermocouples in contact with the surface of the sample that is facing the ion gun.

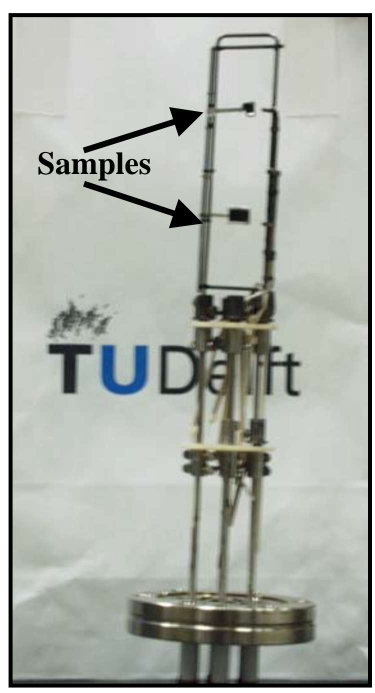

Figure A.1.2: Sample holder

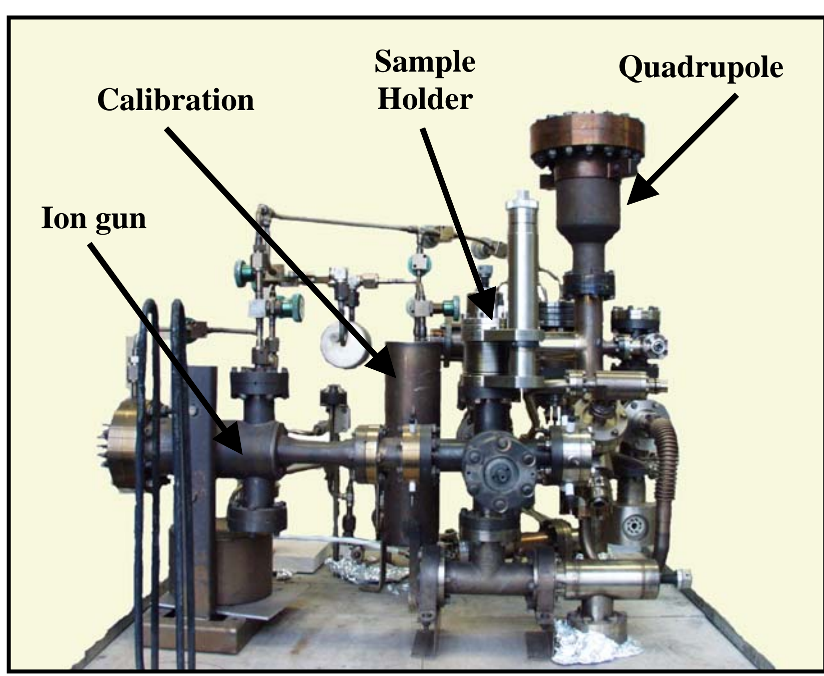

Figure A.1.3: Experimental set-up of THDS: "in-situ implantation" configuration.

- *"Oven " configuration (Fig.A.1.4):*

This configuration is used for samples that have been already implanted outside the apparatus. For example, it is useful to study high energy implantation effects since in the other configuration the maximum implantation energy that can be reached is 3 keV. The sample is

placed in a molybdenum crucible (Fig.A.1.5). This crucible is surrounded by tungsten filaments that can heat up to 2000 K. The oven is directly linked to the quadrupole.

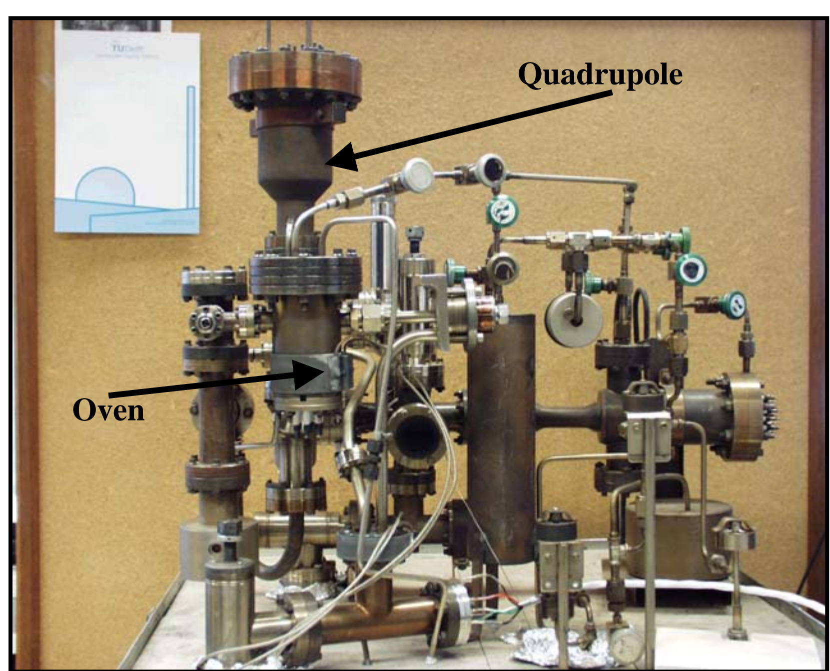

Figure A.1.4: Experimental set-up of THDS: “oven configuration”.

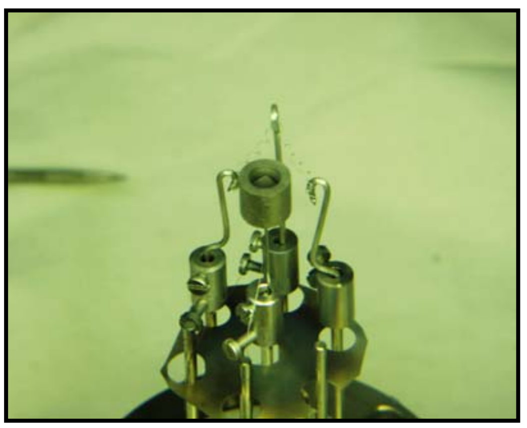

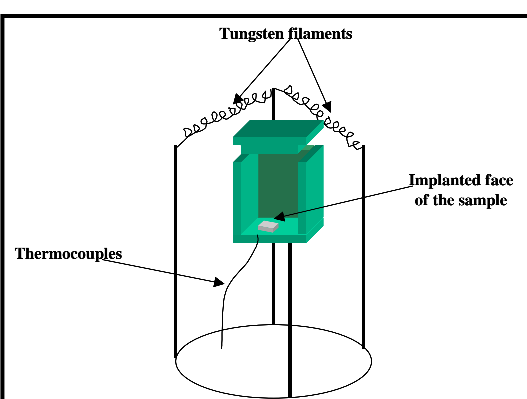

Figure A.1.5: Sample holder and schematic view of the crucible.

To switch from one configuration to another the experimenter just needs to open or closes few valves and connect thermocouple and heating system to the control board.

A.1.3 Modeling

While heating the sample, gas is released in the working chamber of volume V and the partial pressure of the desorbed gas *p* is measured with the mass spectrometer. We can write:

$$V\frac{dp}{dt} = \frac{dN}{dt} - pS \quad (A.1)$$

where N is the number of particles that have not yet desorbed, and S the pumping speed
The desorption rate is then given by:

$$L(t) = -\frac{dN}{dt} = -V\left(\frac{dp}{dt} + \frac{p}{\tau}\right) \quad (A.2)$$

where $\tau = V/S$ is the pumping time constant.

There are basically two modes of operation:

a. *Static* ($\tau \rightarrow \infty$)

with no deliberate pumping of the monitored gas. However pumping will always occur since the mass spectrometer is a pump itself. The desorption rate is then equal to:

$$\frac{dN}{dt} \approx V\frac{dp}{dt} \quad (A.3)$$

so that the desorption rate is proportional to the derivative of the pressure.

b. *Dynamic* $\left(\frac{dp}{dt} << \frac{p}{\tau}\right)$

In this case the desorbed gas is deliberately pumped away and the desorption rate is given by:

$$\frac{dN}{dt} \approx V\frac{p}{\tau} \quad (A.4)$$

so that the desorption rate is directly proportional to the measured pressure.

- **First-order desorption model:**

During the ramp annealing the defects dissociate at certain temperatures depending on their dissociation energies. The dissociation of the gas from the trap can be described, in many cases, by a first-order dissociation model:

$$\frac{dN}{dt} = -N\nu\exp\left(-\frac{E_{diss}}{kT}\right) \quad (A.5)$$

where N = number of filled traps

ν = attempt frequency (s^{-1})

E_{diss} = dissociation energy (eV)

k = Boltzmann constant ($eV.K^{-1}$)

T = absolute temperature (K)

However, diffusion from the traps to the sample surface can also lead to gas release. Thus the desorption can be described as first-order desorption if the desorption process is ruled by the dissociation from traps and if this dissociation is the first-order process. The first-order desorption model is valid in most cases of helium if:

1. The diffusion of the dissociated gas atoms in the sample is fast, i.e. $E_{migr} << E_{diss}$.
2. Gas atoms do not experience any surface barrier or recombination at the surface.
3. Every dissociation reaction provides only one dissociated atom.
4. No interactions exist between traps, i.e. the dissociated atoms are not retrapped by more stable traps.

The desorption rate for the first-order desorption process is:

$$L(T) = -\frac{dN}{dt} = N\nu \exp\left(-\frac{E_{diss}}{kT}\right) \quad (A.6)$$

At the temperature T_{max} at which the release in the desorption peak is maximum, the dissociation energy E_{diss} can be derived from the following equation:

$$\frac{E_{diss}}{kT_{max}^2} = \frac{\nu}{\beta} \exp\left(-\frac{E_{diss}}{kT_{max}}\right) \quad (A.7)$$

where $\beta = dT/dt$ is the annealing rate (typical value for β is 10 $K.s^{-1}$).

References

[Buters *et al.* 1987] W.Th.M. Buters, J.H. Evans, A. van Veen, A. van den Beukel, *J. Nucl. Mat.* **148**, 17 (1987).

[Gorkum *et al.* 1981] A.A. van Gorkum, E.V. Kornelsen, *Vacuum,* **31**, 89 (1981).

[Kornelsen *et al.* 1981] E.V. Kornelsen, A.A. van Gorkum, *Vacuum,* **31**, 99 (1981).

[Redhead 1981] P.A. Redhead, *Vacuum*, **12**, 203 (1962).

[Van Veen *et al.* 1981] A. van Veen, A. Warnaar, L.M. Caspers, *Vacuum*, **30**, 109 (1980).

[Van Veen 1987] A. van Veen, *Materials Science Forum* **15-18**, 3 (1987).

[Van Veen 1991] A. van Veen, in: *Fundamental Aspects of Inert Gases in Solids*, S.E. Donnelly, J.H. Evans (Eds), NATO ASI series B, Physics 279, Plenum Publishing Corp., New York, 1991, pp 41-57.

[Ziegler *et al.* 1985] J.F. Ziegler, J.P. Biersack, U. Littmark, *The Stopping and Range of Ions in Solids* (New York: Pergamon), (1985).

Appendix.2: Experimental data

A.2.1 6H-SiC

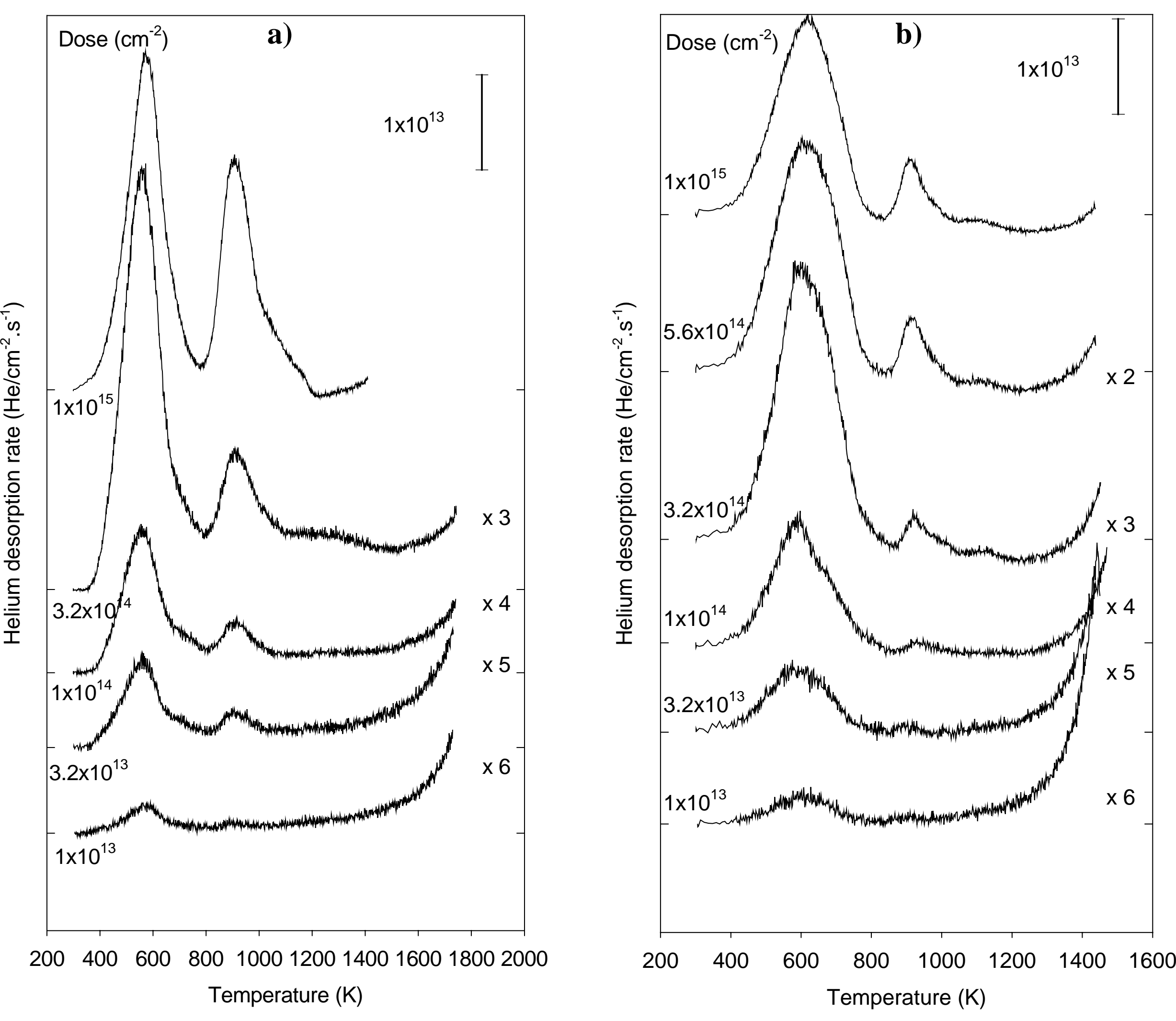

Figure A.2.1: Desorption spectra obtained for 6H-SiC implanted with 100 eV **(a)** and 300 eV **(b)** He ions at the indicated doses.

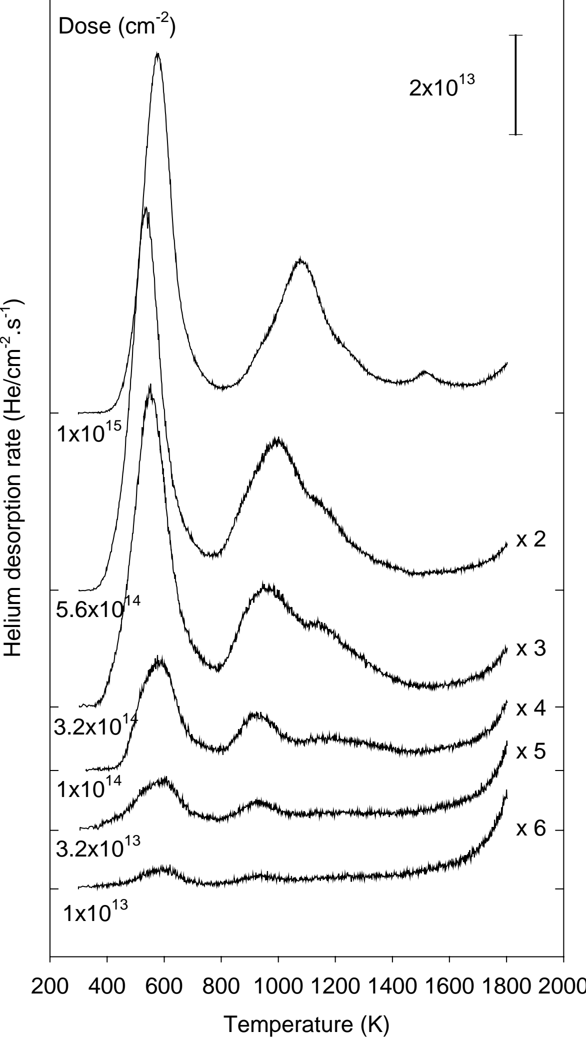

Figure A.2.2: Desorption spectra obtained for 6H-SiC implanted with 500 eV He ions at the indicated doses.

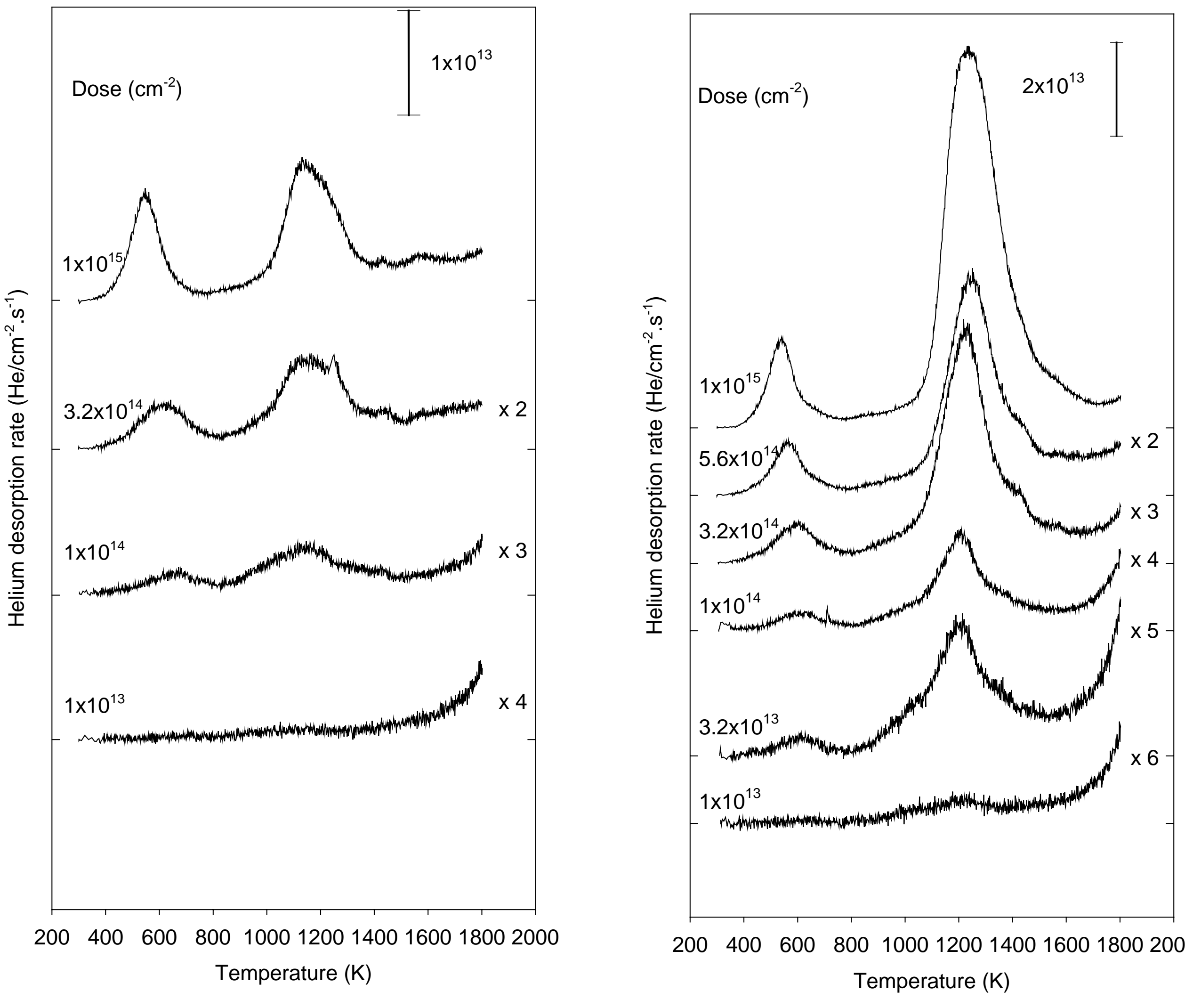

Figure A.2.3: Desorption spectra obtained for 6H-SiC implanted with 1.5 k eV **(a)** and 2 k eV **(b)** He ions at the indicated doses.

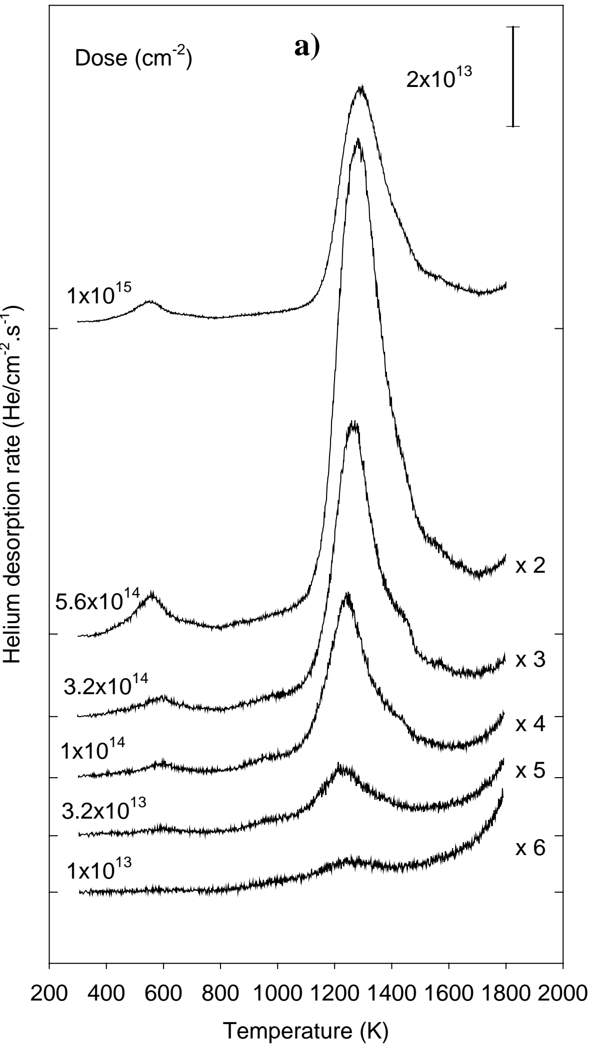

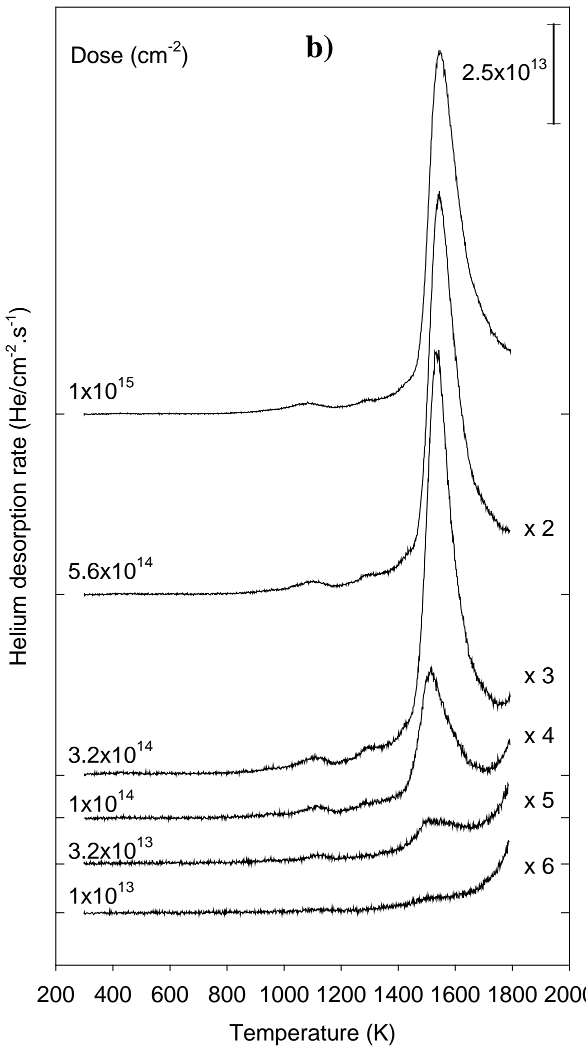

Figure A.2.4: Desorption spectra obtained for 6H-SiC implanted with 2.5 k eV(**a**) and 3 k eV (**b**) He ions at the indicated doses.

A.2.2 4H-SiC

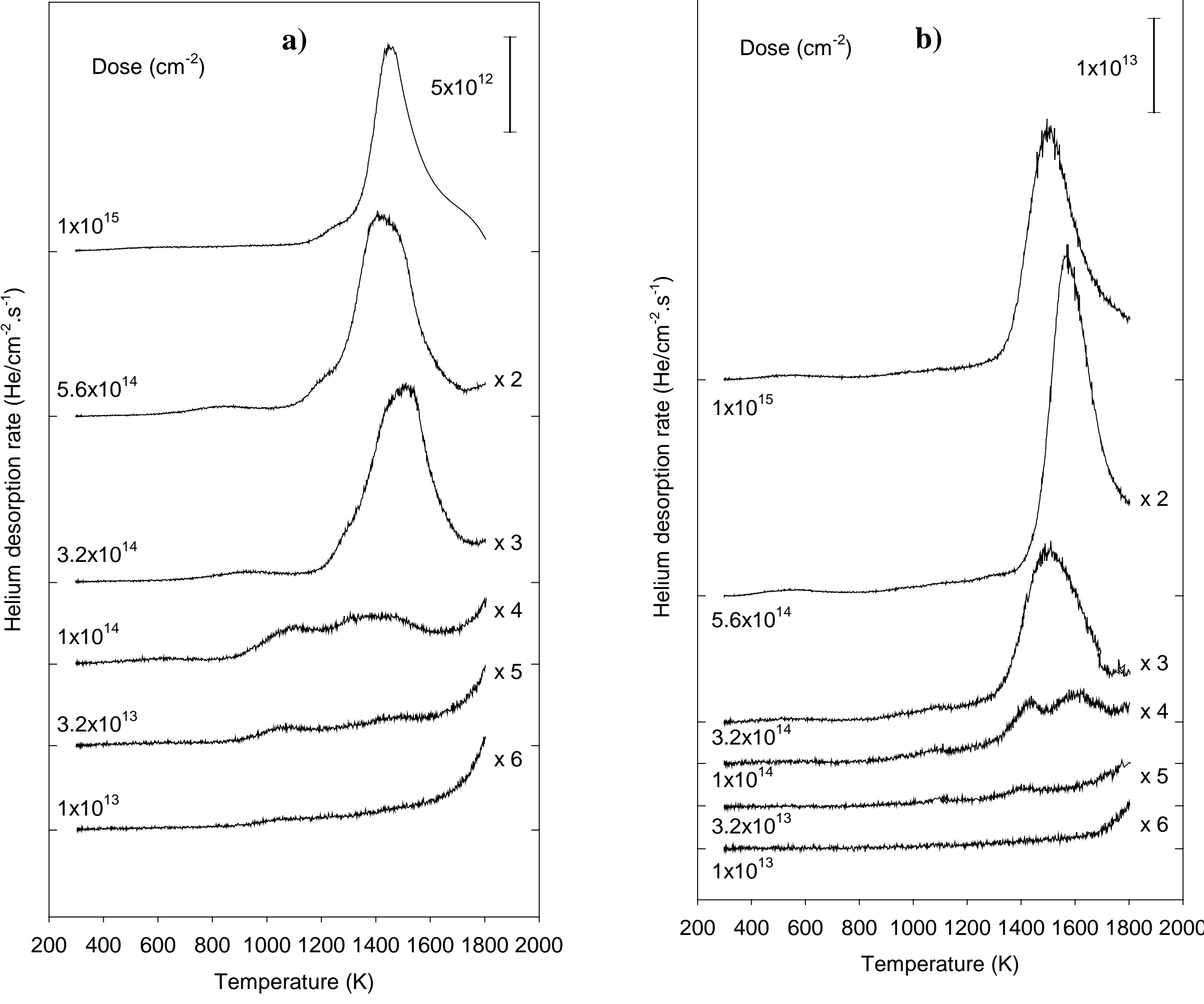

Figure A.2.5: Desorption spectra obtained for 4H-SiC(2) implanted with 500 eV **(a)** and 2 keV **(b)** He ions at the indicated doses.

Data	*Description*	*Polytypes*	*Method*	*Source*
$E^{diss}_{He-V} = 1.1\ eV$	Dissociation energy of He from V	α–SiC	Experimental	J.Chen 2000
$E^{diff}_{Si} = E^{diff}_{C} = 7 - 9\ eV$	Diffusion energies of Si and C	α–SiC	Experimental	J.Chen 2000
$E^{Si}_{d} \approx 40\ eV$	Threshold displacement energy of Si	SiC	Experimental	Zinkle (1997)
$E^{C}_{d} \approx 20\ eV$	Threshold displacement energy of C	SiC	Experimental	Zinkle (1997)
$E^{eff}_{d} = 25\ eV$	Effective displacement energy for SiC	SiC	Experimental	Zinkle (1997)
$E^{form}_{V_{Si}} = 3.6\ eV$	Formation energy of Si vacancy	β–SiC	Calculation	Huang (1993)
$E^{form}_{V_{C}} = 2.7\ eV$	Formation energy of C vacancy	β–SiC	Calculation	Huang (1993)
$E^{form}_{I_{Si}}(T_{Si}) = 9.8\ eV$	Formation energy of Si interstitial in the Si sublattice	β–SiC	Calculation	Huang (1993)
$E^{form}_{I_{Si}}(T_{C}) = 2.5\ eV$	Formation energy of Si interstitial in the C sublattice	β–SiC	Calculation	Huang (1993)
$E^{form}_{I_{C}}(T_{C}) = 3.3\ eV$	Formation energy of C interstitial in the C sublattice	β–SiC	Calculation	Huang (1993)
$E^{form}_{I_{C}}(T_{Si}) = 3.7\ eV$	Formation energy of C interstitial in the Si sublattice	β–SiC	Calculation	Huang (1993)
$E^{form}_{I_{He}}(T_{C}) = 0.7\ eV$	Formation energy of He interstitial in the C sublattice	β–SiC	Calculation	Huang (1993)
$E^{form}_{I_{He}}(T_{Si}) = 1.1\ eV$	Formation energy of He interstitial in the Si sublattice	β–SiC	Calculation	Huang (1993)
$E^{m}_{V_{Si}} = 2.9\ eV$	Si vacancy migration energy	β–SiC	Calculation	Huang (1995)
$E^{m}_{V_{C}} = 2.6\ eV$	C vacancy migration energy	β–SiC	Calculation	Huang (1995)
$E^{m}_{I_{Si}} = 4\ eV$	Migration energy of Si interstitial	β–SiC	Calculation	Huang (1995)
$E^{m}_{I_{C}} = 1.3\ eV$	Migration energy of C interstitial	β–SiC	Calculation	Huang (1995)
$D = 3.22\ g/cm^3$	Density	4H–SiC	Experimental	Harris (1995)
$E_{gap} = 3.0\ eV$	Bandgap	6H–SiC	Experimental	Wesch (1996)
$E_{gap} = 3.3\ eV$	Bandgap	4H–SiC	Experimental	Wesch (1996)
4.9 W/cm.K	Thermal conductivity	6H,4H–SiC	Experimental	Wesch (1996)
$E = 370\ cm^2/V.s$	Electron mobility at $10^{16}\ cm^{-3}$	6H–SiC	Experimental	Wesch (1996)
$E = 800\ cm^2/V.s$	Electron mobility at $10^{16}\ cm^{-3}$	4H–SiC	Experimental	Wesch (1996)
$H = 90\ cm^2/V.s$	Hole mobility at $10^{16}\ cm^{-3}$	6H–SiC	Experimental	Wesch (1996)
$H = 115\ cm^2/V.s$	Hole mobility at $10^{16}\ cm^{-3}$	4H–SiC	Experimental	Wesch (1996)

Table A.2.1: Formation and migration energies of point defects in silicon carbide and relevant data given by the literature. T_{Si} denotes the silicon sub-lattice and T_C the carbon sub-lattice.

Acknowledgements

To carry out the work reported in this PhD thesis, I have been privileged to meet and work with many people who helped me, motivated me and guided me. I would like to acknowledge them all here.

This work has been carried out at the University of Poitiers in the *Laboratoire de Métallurgie Physique* (LMP), directed by Monsieur Jean Mimault whom I would like to thank for welcoming me.

I would like to thank Mr. Claude Templier for accepting the role of chairman of the jury and also for the huge bibliography that he gave me!

I'm grateful to Messrs Steve Donnelly and Tom van Veen for reading this thesis. Their critical remarks on both physics and language have been invaluable.

I also thank Monsieur Daniel Alquier for his participation in the jury and for his critical comments on the work.

During the three years of my PhD work, I was fortunate to work within a very dynamic and friendly team. In this team I would especially like thank my two supervisors Jean-François Barbot and Marie-France Beaufort for all the support with which they provided me and for the dynamism they put into this work. They showed me the way to become a researcher. Their availability for all my questions and problems on physics but also on administrative staff was enormous: thanks Jean-François for all the administrative papers and application forms you've done for me!! This work is the result of everyday informal discussion meeting that could be held in the corridor (!) but that have created a strong group dynamics and from which many ideas have raised. I should mention also that parallel to work interaction, a strong friendship has developed. The dinners with your families, coffee breaks, beer breaks…etc, were great moments. All this aspects have made my work much more easy to achieved and in a happy way!

Many thanks go to Alain Declémy for the X-ray work and fruitful discussions.

I'm grateful to Professor Tom van Veen for allowing me to work in his laboratory (IRI). He introduced me to the desorption technique and stimulated the very interesting studies presented in this thesis. His background on the subject has lead to very fruitful discussions not only about desorption but about physics in general. His help in the interpretation of the experimental results has been invaluable. I would also like to thank again my two supervisors in France, Marie-France Beaufort and Jean-François Barbot for all the efforts they put into

making my stay in Holland possible. They have always been there for me and were as motivated as I was about my research project.

In the IRI, I was fortunate to meet many researchers. Among them I am indebted to Alexander Fedorov for teaching me everything about HDS1 apparatus and for all the help he gave me and the kindness he showed me during my entire stay in Holland. He also introduced me to the Friday night IRI bar which became a ritual before our weekend trips. Cooking Dutch food at the bar was a great experience! I also thank Kees Westerduin for technical support, medical support (the electric shock was really scary!). Thanks to all the students (the Spanish connection, the Russian connection and of course the Dutch connection) I met in the institute for parties, hot-chicken and kebab night, beer rallies and week-end trips that make up the so-called “student life”!! Special thanks go to Ramon, Alfonso and Dani who welcomed me in their flat when I was homeless. Many thanks to Henk Schut for welcoming me on my arrival in Delft and for driving and taking care of my van (believe me, that’s a difficult exercise!!). Ice-skating on the frozen canal in front of the lab was a unique experience and so was skiing in Den Haag! I would like to acknowledge everyone at NUFFIC who provided me with financial support by means of a Huygens grant (for information see http:\\www.nuffic.nl) that made this stay possible.

Esidor Ntsoenzok and Sylvie Godey at the CERI, Claude Fayoux and Philippe Guerin at the LMP are greatly acknowledged for implantation of samples. I would like to thanks Hilde Garem for teaching me and helping me with TEM. Working with her was always a great pleasure and discussions on TEM characterization were always fertile.

Hopefully, PhD student life is not only limited to work and so I would like to thank all the people I have met during these three years and who became friends. Thanks to all of you for support, weekend trips to the seaside, ski holidays, dinners, barbecues, parties, football games (I did my best to improve my level!!), go-carting, pub-crawl, … : *Fabien* (the Kebab man), *Laurent* (the sport man), *Frank* (the Marseille-belote man), *Marie-Laure* (the mushroom girl; not because she looks like but because she likes picking them! You are a great colleague to work with, thank you for everything) *Matthieu* (the beer and bar emptier man), *Thibaut*, *Pascaline* and *Jules* (our second family!), *Anne-Solenn* (the shiny girl), *Maité* (the Spanish cochinilla), *Enkhar* (the Spanish drinker), *Pascal* and *Christine* (the south expatriate couple), *Pizza* (the jembe man) and *Karine* (the Bretonne compatriot) and also the “young “ generation (*Fabien*, *Julien, Nikhil*, *Gintautas*, *Yves, Julien*, *Damien, Valérie*).

Finally, I would like to thank all my family who were always there for me and without whom this work couldn’t have been achieved.

RESUME

Les recherches présentées dans cette thèse ont été effectuées au Laboratoire de Métallurgie Physique de l'Université de Poitiers ainsi qu'au sein du groupe Defects in Materials appartenant au Interfaculty Reactor Institute de l'Université Technologique de Delft (Pays-Bas).

Les exigences concernant la qualité des matériaux semi-conducteurs utilisés en microélectronique deviennent de plus en plus drastiques. En effet, la présence d'impuretés et de défauts cristallographiques peut fortement modifier les caractéristiques des diodes. Il est donc impératif de les supprimer afin d'améliorer les performances des dispositifs. Des études récentes sur les cavités créées dans le silicium par implantation d'hélium à haute dose suivie d'un recuit à haute température, ont montré que ces dernières peuvent être utilisées pour le piégeage d'impuretés métalliques. Le silicium joue un rôle majeur dans la technologie actuelle des semi-conducteurs. Cependant pour de nouvelles applications, en particulier en milieu hostile, le carbure de silicium semble être un candidat prometteur.

Les défauts introduits par l'implantation d'hélium dans le silicium et dans le carbure de silicium ont été étudiés par MET (Microscopie Electronique en Transmission). Des techniques complémentaires comme la desorption d'hélium (THDS) et la DRX (Diffraction des Rayons-X) ont également été utilisées. Nous avons observé que dans le cas d'implantations à forte énergie (MeV), de nombreux défauts étendus de type interstitiel sont crées parallèlement à la formation des bulles. Nous avons montré que la formation des bulles dépend fortement du flux et que le taux de production des lacunes est un paramètre déterminant. Les effets du temps de recuit et de la température d'implantation ont également été étudiés. Dans le carbure de silicium, la formation de bulles se produit dans une zone amorphe et l'évolution en cavités a été étudiée en fonction de divers recuit. Une étude par THDS des précurseurs des bulles est également présentée.

ABSTRACT

The work presented in this Ph.D thesis has been done in the Laboratoire de Métallurgie Physique at the University of Poitiers and in the group Defects in Materials of the Interfaculty Reactor Institute at the Technological University of Delft (Netherlands).

Materials requirements for semiconductors used in microelectronics become continuously more severe. Indeed, impurities and crystallographic defects can strongly modify the characteristics of electronic devices and thus must be fully controlled in order to improve device performance. Recently, helium induced cavities in silicon wafers have received considerable attention due to their efficiency as gettering sites for metallic impurities. Cavities in silicon are usually formed by high dose He ion implantation followed by annealing at high temperatures. Even if silicon plays a major role in the development of today semiconductor device technology, silicon carbide is one of the most promising candidate to extend future microelectronic applications.

In this thesis TEM (Transmission Electron Microscopy) investigations of defects introduced by helium implantation in silicon and in silicon carbide are presented. Additional techniques such as THDS (Thermal Helium Desorption Spectrometry) and XRD (X-Ray Diffraction) have been also used. In case of medium dose MeV implantation in silicon, an alternative route for bubble formation is found, leading to numerous interstitial-type extended defects. We have shown that the dose-rate strongly influence the formation of bubbles and of related defects. Further studies on the effects of annealing time and implantation temperature have been performed. Implantation at room temperature of high dose helium ions into SiC leads not only to the formation of small bubbles but also to amorphization. At 1500°C annealing recrystallization take place leading to polytypisme and to the enlargement of the cavities. THDS studies on bubbles precursors in SiC are also presented.

MOTS CLEFS

-silicium
-carbure de silicium
-implantation ionique
-hélium
-bulles
-piégeage
-lacunes
-interstitiels
-dislocations
-désorption

KEY WORDS

-silicon
-silicon carbide
-ion implantation
-helium
-bubbles
-gettering
-vacancies
-interstitials
-dislocations
-desorption